

**Investigations on Microstructure Evolution of
Metal Additive Manufacturing by Experiments, Physics-based and Data-driven Modeling**

by

Yaohong Xiao

A dissertation submitted in partial fulfillment
of the requirements for the degree of
Doctor of Philosophy
(Mechanical Sciences and Engineering)
in the University of Michigan-Dearborn
2023

Doctoral Committee:

Assistant Professor Lei Chen, Chair
Professor Fei Gao
Associate Professor German Reyes-Villanueva
Professor Yi Zhang

Yaohong Xiao

yaohongx@umich.edu

ORCID iD: 0009-0004-5909-9428

© Yaohong Xiao 2023

To Yaohong Xiao's family

Acknowledgements

My gratitude towards Prof. Lei Chen is immeasurable. His unceasing support and mentorship throughout my doctoral journey were invaluable, and for that, I am profoundly thankful. I am also immensely grateful to Prof. German Reyes-Villanueva for his significant guidance and support in the experiment. His expertise and insights were critical in my experiments, and I deeply appreciate his unwavering belief in my potential. I am immensely appreciative of the guidance and constructive feedback from the esteemed committee members during the intricate process of my dissertation. Their expertise and insights have indeed been enlightening. A heartfelt thank you to my parents who have provided a constant pillar of spiritual support and understanding. Their belief in me has been a source of strength and inspiration. I extend my sincere gratitude to my colleagues, whose companionship and kindness have enriched my journey through graduate school. Their camaraderie has truly lightened the rigors of academic pursuit. Thank you all for being a part of my journey.

Table of Contents

| | |
|---|------|
| Dedication..... | ii |
| Acknowledgements..... | iii |
| List of Tables | viii |
| List of Figures..... | ix |
| Abstract..... | xiv |
| Chapter 1: Introduction..... | 1 |
| 1.1 Metal additive manufacturing | 1 |
| 1.2 Complex AM processes and challenges..... | 3 |
| 1.2.1 Motivation | 4 |
| 1.2.2 Thesis Objectives..... | 6 |
| 1.3 Outline of this dissertation | 6 |
| Chapter 2: Literature review | 8 |
| 2.1 Additive manufacturing process effect on single metal microstructures | 8 |
| 2.1.1 Grain structure | 8 |
| 2.1.2 Porosity..... | 9 |
| 2.1.3 Phase..... | 11 |
| 2.1.3.1 Ti-6Al-4V | 11 |
| 2.1.3.2 SS316L..... | 14 |
| 2.1.3.3 IN625 | 15 |
| 2.1.4 Question 1 to be Addressed..... | 16 |

| | |
|--|----|
| 2.2 Additive manufacturing process effect on bimetal microstructures..... | 17 |
| 2.2.1 Question 2 to be Addressed..... | 18 |
| 2.3 Optimization of microstructure by controlling melt pool. | 19 |
| 2.3.1 Question 3 to be Addressed..... | 20 |
| 2.4 Common Methods used for microstructural development understanding | 21 |
| 2.4.1 Experimental methods | 21 |
| 2.4.2 Physical modeling | 21 |
| 2.4.3 Data-driven modeling..... | 22 |
| Chapter 3: Phase evolution of AM-ed Ti-6Al-4V by a Gleeble and FEM-assisted methods..... | 23 |
| 3.1 Introduction | 23 |
| 3.1.1 Background..... | 23 |
| 3.2 Experimental methods..... | 25 |
| 3.2.1 Directly laser deposition process of Ti-4Al-4V | 25 |
| 3.2.2 Gleeble experiments | 25 |
| 3.2.3 Characterization of the microstructure and mechanical testing | 27 |
| 3.3 Computational method: thermal modelling..... | 27 |
| 3.4 Results | 29 |
| 3.4.1 Phase and microstructures | 29 |
| 3.4.2 Vickers hardness testing..... | 35 |
| 3.5 Discussion | 36 |
| 3.5.1 The analyses of phase evolution..... | 36 |
| 3.5.1.1 Phase transformation pathway of α' zone | 36 |
| 3.5.1.2 Phase transformation pathway of $\alpha'+\alpha_m$ zone..... | 39 |
| 3.5.1.3 Phase transformation pathway of $\alpha + \beta$ zone..... | 41 |

| | |
|---|----|
| 3.5.2 Phase evolution of α_m and α' | 43 |
| 3.5.2.1 Gleeble designed experiments | 43 |
| 3.5.2.2 Thermodynamic analysis | 44 |
| 3.6 Chapter conclusions | 46 |
| Chapter 4: Quantitative simulations of grain nucleation and growth at additively manufactured bimetallic interfaces of SS316L and IN625 | 48 |
| 4.1 Introduction | 48 |
| 4.1.1 Background..... | 48 |
| 4.2 The methodology framework | 50 |
| 4.3 Experimental methods..... | 52 |
| 4.4 Computational methods..... | 53 |
| 4.4.1 Transient temperature field and flow behavior modeling | 54 |
| 4.4.2 3D solidification phase-field modeling | 57 |
| 4.5 Results and discussion..... | 61 |
| 4.5.1 Flow behaviors, composition redistribution, and liquidus temperature | 61 |
| 4.5.2 The temperature field and melt pool morphology | 65 |
| 4.5.3 Mechanism of nucleation and grain growth | 66 |
| 4.5.3.1 Final grain morphologies | 66 |
| 4.5.3.2 The nucleation and grain growth at the interface of IN625/SS316L | 68 |
| 4.5.3.3 The nucleation and grain growth at the interface of SS316L/ IN625 | 71 |
| 4.6 Chapter conclusions | 75 |
| Chapter 5: Using machine learning to improve melt pool prediction in additive manufacturing: data denoising and predictive modeling | 77 |
| 5.1 Introduction | 77 |
| 5.1.1 Background..... | 77 |

| | |
|--|-----|
| 5.2 Experiment and Raw data | 80 |
| 5.3 Machine learning methodologies | 83 |
| 5.3.1 Convolutional neural network for denoising processing..... | 83 |
| 5.3.2 Artificial neural network for melt pool prediction | 85 |
| 5.4 Results | 89 |
| 5.4.1 Denoising modeling validation..... | 89 |
| 5.4.2 Melt pool denoising..... | 90 |
| 5.4.3 Melt pool prediction | 91 |
| 5.5 Discussion | 94 |
| 5.5.1 Noise effects | 94 |
| 5.6 Chapter conclusions | 97 |
| Chapter 6: Conclusion and Perspectives..... | 100 |
| References..... | 103 |

List of Tables

| | |
|--|----|
| Table 2-1 Characteristics of the products cooling form Beta phase [46][47]..... | 12 |
| Table 3-1 Coefficients for density, specific heat, and conductivity of Ti-6Al-4V [20][115]..... | 28 |
| Table 3-2 Processing parameters of the thermal model [20][115]. | 29 |
| Table 3-3 Phase evolution criteria. | 38 |
| Table 4-1: Physical parameters of the IN625 [152][156][174][175][176] and SS316L alloys [152] [177][178][179]. | 60 |
| Table 5-1: Comparisons between our model, NBEM model, and L-NBEM model..... | 87 |

List of Figures

| | |
|---|----|
| Figure 1-1: Various industrial applications of AM (Images downloaded from: http://www.all3dp.com , http://www.michelinmedia.com , http://luxcreo.com , http://wyss.harvard.edu , https://all3dp.com). | 1 |
| Figure 1-2: Schematic of the (a) powder bed fusion system (PBF) and (b) direct energy deposition system (DED). | 2 |
| Figure 1-3: Complicated physics around the melt pool [19]. | 3 |
| Figure 2-1: EBSD maps of β -grain structures for AM-ed Ti6Al4V [26], Inconel 625 [27] and AlSi10Mg [28]. | 9 |
| Figure 2-2: Visual examples of various types of pores in AM-produced metals: (a) lack-of-fusion pores in AM-ed Ti6Al4V [38] and (b) in IN 718 [39], (c) keyhole pores in AM-ed Ti6Al4V, gas pores in (d) AM-ed Ti6Al4V [38] and in (e) IN 718 [39], and (f) hydrogen porosity in AM-ed AlSi10Mg [40]. | 10 |
| Figure 2-3: (a) Phase diagram of the titanium alloys [45], and (b) Schematic continuous cooling diagram for Ti-6Al-4V β -solution treated at 1050°C for 30 min [46]. | 12 |
| Figure 2-4: The typical Optical micrographs of various cooling products [46]. | 13 |
| Figure 2-5: (a) SEM images of various α' phases in as-built Ti-6Al-4V [51], (b) finer lamellar $\alpha+\beta$ phases through <i>in-situ</i> martensite decomposition [53], and (c) $\alpha+\alpha'$ phases through heat treatment [57]. | 14 |
| Figure 2-6: (a) XRD patterns of the SS316L precursor powder and the as-built SS316L [67] and (b) EBSD phase fraction map of a selected area in as-built SS316L (red: ferrite; green: austenite) [68]. | 15 |
| Figure 2-7: (a) Elemental X-ray maps of as-built IN625 sample [73], (b) SEM images of as-built IN625 to show the Laves phase [76], (c) SEM images of solution treated IN625 (1050 °C for 2 h) to NbC and (c) Microstructure of AM-ed IN625 after heat treatment of 1 h at 870 °C to show δ -phase [75]. | 16 |
| Figure 3-1: (a) The schematic diagram of the LENS machine with DLDed samples, and (b) Gleeble 3500D with a cubic sample. | 27 |
| Figure 3-2: (a) the schematic of cross-section for DLDed Ti-6Al-4V, and (b) the optical microscopy (OM) characterization of the gradient structure in DLDed Ti-6Al-4V, as indicated by red rectangular box in (a). (c) the schematic of samples involved in | |

| | |
|--|----|
| Gleeble: (d) OM characterization of the as-received Ti-6Al-4V for the Gleeble experiment, (e) OM characterization of the water-quenched sample in Gleeble, and (f) part of the local amplification region of (e)..... | 30 |
| Figure 3-3: XRD patterns of the cross-section of three different samples. Blue, green and yellow lines corresponding to gradient structure in DLDED sample (blue rectangular box in Figure 3-2a), water-quenched sample by Gleeble (Figure 3-2e), and the as-received Ti-6Al-4V for Gleeble experiment (Figure 3-2d), separately. | 31 |
| Figure 3-4: optical microscopy (OM) characterization of gradient structure in DLDED Ti-6Al-4V along building direction, i.e., (f)~(a): (a)(b) zone3, i.e., α' zone, (c)(d) zone2, i.e., $\alpha_m+\alpha'$ zone, and (e)(f) zone1, i.e., $\alpha+\beta$ zone. Black arrows indicate GB- α at the prior β grain boundaries, green arrows correspond to the α_m near prior β boundaries, and red arrows point to the sharp edge without GB- α and α_m at prior β boundaries. | 33 |
| Figure 3-5: Scanning electron microscopy (SEM) characterization of gradient structure in DLDED Ti-6Al-4V along building direction, i.e., (f)~(a): (a) zone3, i.e., α' zone, (b)(c) zone2, i.e., $\alpha_m+\alpha'$ zone, and (d)(e)(f) zone1, i.e., $\alpha+\beta$ zone. (g) part of the local amplification region of (d)..... | 34 |
| Figure 3-6: Micro-hardness profile measured along the building direction of gradient structure in DLDED Ti-4Al-6V (left side) and water-quenched Ti-4Al-6V by Gleeble (right side). | 35 |
| Figure 3-7: The computational TCs, i.e., TC12-1~ TC12-12 of LM (M=12): The cooling rate of the melt pool and phase evolution are shown in red rectangular and yellow rectangular, separately. The purple rectangular indicates the TC12-3. | 37 |
| Figure 3-8: (a) The computed TCs at center points of the top 3 layers. (b) optical image of intersection between α' zone and $\alpha'+\alpha_m$ zone. M, and N corresponding to the number of layers and TCs, are numbered starting from the top layer and the first TC, respectively. | 39 |
| Figure 3-9: The computed TCs at center points of the next 9 layers (L4~L12). Monitoring locations for TCs are at the center point of each layer. The α_m phase is marked by red arrows. | 41 |
| Figure 3-10: Left side related to the phase evolution for each zone in the gradient structure of DLDED Ti-6Al-4V, i.e., α' , $\alpha'+\alpha_m$, $\alpha+\beta$ zones. M is the number of layers, K and L indicate the times of TCs used for (transformation). Right side corresponding to Gleeble-quenched counterpart..... | 42 |
| Figure 3-11 The microstructural profiles: (a) the OM image of the etched sample with a cooling rate of 30 °C/s; (b), (c) and (d) corresponding to the IQ (Image Quality) maps of the as-received sample got after quenching process in one, three and four TCs, individually. Red arrows point to the α_m phase. | 44 |

| | |
|---|----|
| Figure 3-12: The Gibbs free energy changes as a function of temperature with different phases. | 46 |
| Figure 4-1: A workflow summarizes the framework combined multi-physics modeling and experimental methods to compressively carry out the study of nucleation and grain growth at the AM-ed bimetallic interfaces of SS316L and IN625. Subfigure (b) shows a sandwich structure of the melt pool considering the flow behaviors, where a mixing zone is at the interface. (I) and (II) from the CFD model indicate the temperature field and flow behaviors separately | 52 |
| Figure 4-2: The schematic of AM-ed sample by directed energy deposition (DED) technique. Z is the building direction, Y is the scanning direction, and X is the step-over direction. | 53 |
| Figure 4-3: (a) Geometry model, whole boundary conditions, and mesh configurations for the CFD modeling, where h , ϵ , and σ are the heat convection coefficient, emissivity, and Stefan-Boltzmann constant, respectively. (b) The temperature-dependent surface tension of IN625 and SS316L..... | 55 |
| Figure 4-4: Schematic illustration of the grain growth model, including boundary conditions, dimensions, order parameters, and coupled temperature field. | 61 |
| Figure 4-5: (a)(c)(e) Case1: IN625/SS316L, and (b)(d)(f) Case2: SS316L/ IN625. The flow filed for (a) Case1 and (b) Case2. The position of composition tests by EDS line scanning in SEM images: (c) yellow arrow line for Case1 and (d) black arrow line for Case2, which are also indicated by the arrow line in (a) and (b). The EDS results for Case1 (e) and Case2 (f), in which Z1, Z2, Z3, and Z4 are transition zone, SS316L zone, IN625 zone, and composition abnormal-change zone (CACZ), separately. All the information is reorganized based on the reference [154]. | 63 |
| Figure 4-6: The simulated compositional distributions after incorporating the flow behavior for (a) Case1 and (b) Case2. The calculated liquidus temperatures for (a) Case1 and (b) Case2 are based on the CALPHAD method and elemental distribution along the EDS line [154]..... | 64 |
| Figure 4-7: The temperature field for Case1 (c) and Case2 (d) based on CFD simulation [154]. The exacted melt pool from the temperature field for Case1 (a) and Case2 (b). | 66 |
| Figure 4-8: (a)(b) Case1: IN625/SS316L, and (c)(d)(e) Case2: SS316L/ IN625, where (a)(c) are PFM predictions, (d) is the enlarged view indicated by the white rectangular box indicated in (c), and (b)(e) are experimental EBSD images, performed by [154]..... | 67 |
| Figure 4-9: Box plots for grain comparisons between EBSD observations and PFM predictions. | 68 |
| Figure 4-10: (a)~(d) present the simulated grain evolution process with time for Case1, i.e., depositing IN625 on SS316L, where the corresponding ΔT_{FL} map indicates the difference between temperature field (T_F) and liquidus temperature (T_L)..... | 69 |

| | |
|--|----|
| Figure 4-11: (a) shows the thermal gradient (G) and the velocity or growth rate (R) at solid-liquid (S/L) interface, and (b) presents the ratio of G/R for the S/L interface for Case1. | 71 |
| Figure 4-12: (a)~(e) present the simulated grain evolution process with time when SS613L depositing on IN625 (Case2), where the ΔT_{FL} indicates the difference between temperature field (T_F) and liquidus temperature (T_L) at the corresponding time. | 73 |
| Figure 4-13: (a) shows the thermal gradient (G) and the velocity or growth rate (R) at the solid-liquid (S/L) interface, and (b) presents the ratio of G/R for the S/L interface for Case2..... | 75 |
| Figure 5-1: Typical examples for plume and spatter exposed under the high-speed camera with references (a) [85] (b) [204], and (c)(d) [202]. | 80 |
| Figure 5-2: (a) Snapshot of AM commands, and (b) visualization of scanning path, including the laser-activated zone. | 81 |
| Figure 5-3: A few representative experimental melt pool images captured by Additive Manufacturing Metrology Testbed (AMMT) at the National Institute of Standards and Technology (NIST)..... | 82 |
| Figure 5-4: The developed convolutional neural network (CNN) model for denoising process of melt pool images..... | 84 |
| Figure 5-5: Structure of the Artificial Neural Network, where Δd_{i-1} and Δt_{i-1} correspond to distance and the time gap between points $i-1$ and the predictive point i , respectively, and P_{i-1} , V_{i-1} , and A_{i-1} indicate the power, scan speed, and melt pool area of laser spot $i-1$, respectively. Subscript i , for example, corresponds to the i^{th} melt pool images, i.e., the i^{th} '2' order of the camera trigger column in the commands (Figure 5-2a) in sequence..... | 86 |
| Figure 5-6: (a) Eight validation results, and (b) the training and validation loss plots of the CNN model. | 90 |
| Figure 5-7: Eight testing results of the denoising process performed on real noisy melt pool images by the trained CNN..... | 91 |
| Figure 5-8: Comparison of average relative error magnitude (AREM) in melt pool area prediction between NBEM and our model (with/without noise) for different testing groups. | 93 |
| Figure 5-9: (a) cumulated area difference of melt pool between ground truth and noisy melt pool for each dataset, and (b) the relative frequency of melt pool area difference for dataset 1. | 93 |
| Figure 5-10: Contour plots of the melt pool area predicted by different models as well as ground truth for testing dataset 16 and 23..... | 94 |

Figure 5-11: With a designed Gaussian normal distribution noise, the AREM changes with (a) noise proportion and (c) noise size (times of initial added noise size AIANS) for each testing dataset. The average AREM changes against (b) noise proportion and (d) noise size..... 95

Figure 5-12: Contour plots of (a) melt pool area predictions by the trained ANN model with noise-free datasets, i.e., Figure 5-10c, (b) ground truth, i.e., Figure 5-10a, (c)(e) melt pool area predictions by the trained ANN model with noisy datasets, and (d)(f) ground truth with noise addition in dataset 16..... 97

Abstract

Metal additive manufacturing (AM) involves a suite of processes where raw metal materials are joined or solidified under computer control to create three-dimensional objects. The AM process facilitates streamlined product development cycles, maximizes the potential of computer-aided design (CAD) to foster designers' creativity, and enables the fabrication of intricate, on-demand parts. AM has found applications in diverse fields, ranging from biomedical to aerospace, and even the oil and gas industry. However, its complexity and the array of process factors involved pose significant challenges in comprehensively understanding and optimizing microstructure evolution, a critical aspect for quality control and performance enhancement.

Despite the considerable research efforts dedicated to studying the intricate AM process-microstructure relationship, such as grain structures, porosity, and phase, numerous questions about microstructural development persist. This is primarily due to the complexity of the AM process and the variety of metal species involved. Key questions include: (1) How do dynamic thermal conditions influence microstructural development, particularly in the context of complex physics during AM of multi-phase metals (e.g., Ti-6Al-4V)? (2) How does the potential flow-driven compositional redistribution affect the microstructural development of bimetals? (3) How can we employ cost-effective and swift data-driven modeling to expedite the establishment of complex AM process-microstructure relationships for microstructure optimization and quality control?

To effectively address these questions, we employed a physics-based framework that includes experimental fabrication and validation, physics-based additive manufacturing modeling, and data-driven modeling to deepen our understanding of microstructural development. This research provides insights into microstructural evolution during AM of single metals and bimetals and proposes a cost-effective and efficient method for microstructural optimization through melt pool control. Specifically, we thoroughly examined the gradient structure featured with different phases in AM-fabricated Ti-6Al-4V, and systematically explored and validated the location-dependent phase evolution. Additionally, we achieved a quantitative understanding of the bimetallic structures of SS316L and IN625 by directed energy deposition (DED). Finally, we established a data-driven modeling framework with experimental data inputs from the National Institute of Standards and Technology (NIST) for rapid extrapolative melt pool prediction for unbuilt parts. This study presents a physics-based framework allowing for a comprehensive understanding of microstructural evolution, with the goal of achieving microstructure optimization and quality control of AM products.

Chapter 1: Introduction

1.1 Metal additive manufacturing

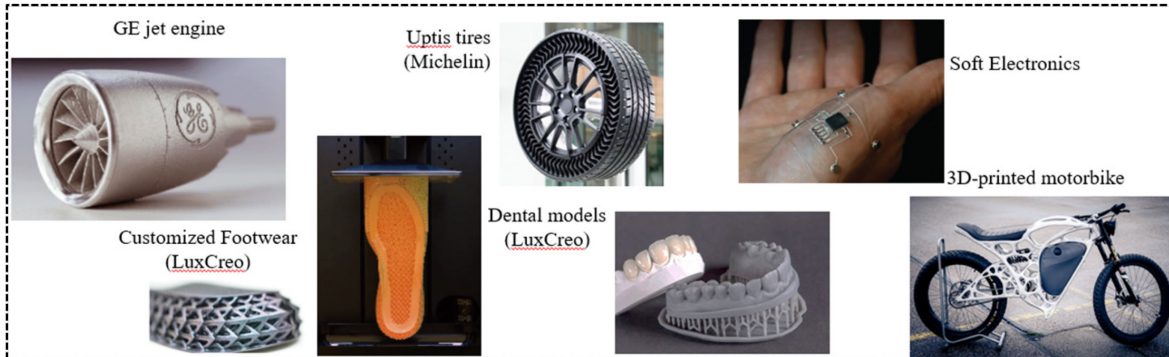


Figure 1-1: Various industrial applications of AM (Images downloaded from: <http://www.all3dp.com>, <http://www.michelinmedia.com>, <http://luxcreo.com>, <http://wyss.harvard.edu>, <https://all3dp.com>).

Additive Manufacturing (AM), commonly referred to as 3D printing, represents a paradigm shift in manufacturing technologies. Through an array of processes, raw materials are fused or joined, generally layer by layer, under computer control to fabricate complex three-dimensional objects. Unlike traditional manufacturing methods such as casting, forging, and machining, which are often limited by mold or tool shapes, AM harnesses the power of Computer-Aided Design (CAD) to foster design innovation and facilitate the fabrication of complex and custom components. AM is renowned for its efficiency, reduced waste, and ability to expedite product development cycles. Its applications are vast and diverse, spanning industries such as biomedical, aerospace, and oil and gas, as shown in Figure 1-1. Various techniques, such as Fused Deposition Modeling (FDM) for polymers, Stereolithography (SLA) for resins, and Inkjet Printing for ceramics, have been developed to cater to different materials. In metal additive manufacturing, high-energy beams such as lasers and electron beams are employed to provide the concentrated heat necessary for establishing metallurgical bonds between metal powders or wire with high

melting points, with the process typically conducted in an inert atmosphere to prevent oxidation and contamination.

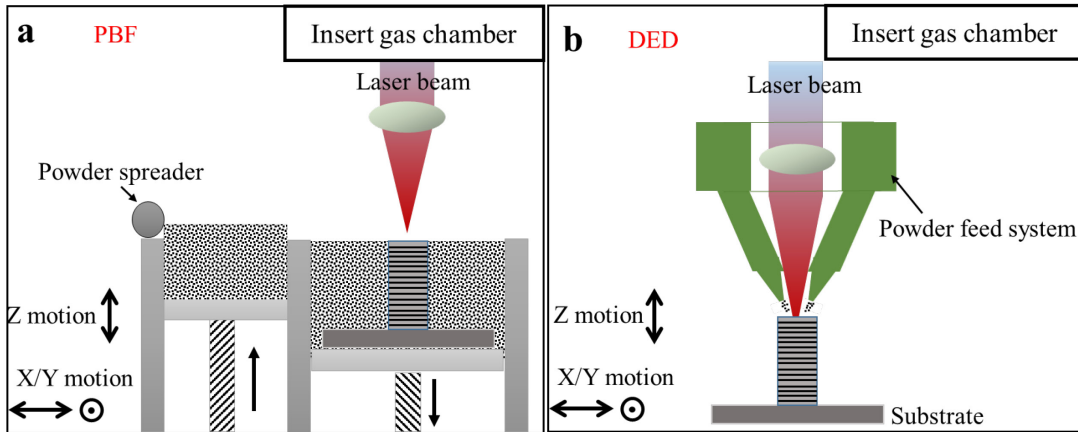


Figure 1-2: Schematic of the (a) powder bed fusion system (PBF) and (b) direct energy deposition system (DED).

In metal additive manufacturing, Directed Energy Deposition (DED) [1][2][3][4][5] and Powder Bed Fusion (PBF) [6][7][8][9][10] stand as the two predominant techniques. Both share the common approach of using an energy source to partially melt raw materials, building objects layer by layer. However, their differences are rooted in the positioning of raw materials and their consequent strengths and ideal applications. DED, as depicted in Figure 1-2b, operates with the feedstock moving in sync with the heat source. This method is particularly efficient for quickly fabricating large components. Notably, DED can employ multiple materials within a single build, which is advantageous for creating functionally graded materials (FGMs) [11][12][13][14][15] and is also ideal for repair work or adding material to pre-existing components [16][17]. However, DED tends to sacrifice resolution and surface finish due to its focus on scale and speed. In contrast, PBF is known for its precision. In this technique, as shown in Figure 1-2a, the feedstock is usually a powder that is laid out on a build platform. The heat source then selectively melts the powder as per the design. This precision allows PBF to produce parts with intricate details and a high-quality surface finish. Nonetheless, PBF is more time-consuming and typically less efficient in material usage compared to DED. Therefore, DED is best suited for applications demanding large-scale,

rapid production, and the integration of multiple materials, such as FGMs. PBF, on the other hand, is the go-to technique for producing highly detailed, high-resolution parts where surface quality is essential.

1.2 Complex AM processes and challenges

While AM offers unparalleled advantages over traditional metal manufacturing methods, the interaction between the energy beam and feedstocks, coupled with layer stacking, introduces complexities into the metallurgical processes and underlying physics. Figure 1-3 illustrates the intricate physics surrounding the melt pool, including convection, fluid flow, radiation, balling, powder denudation, cyclic heating and remelting, super-fast cooling, and non-equilibrium solidification, among others. These phenomena are uncommon in traditional casting but are intrinsic to metal AM processes. Furthermore, AM processes are influenced by numerous parameters (up to 130 [18]), including energy input, scanning speed, hatch distance, and laser beam shape, as well as material properties (e.g., powder distribution, thermal conductivity) and characteristics of AM machines. These factors collectively contribute to the complexity of AM process control.

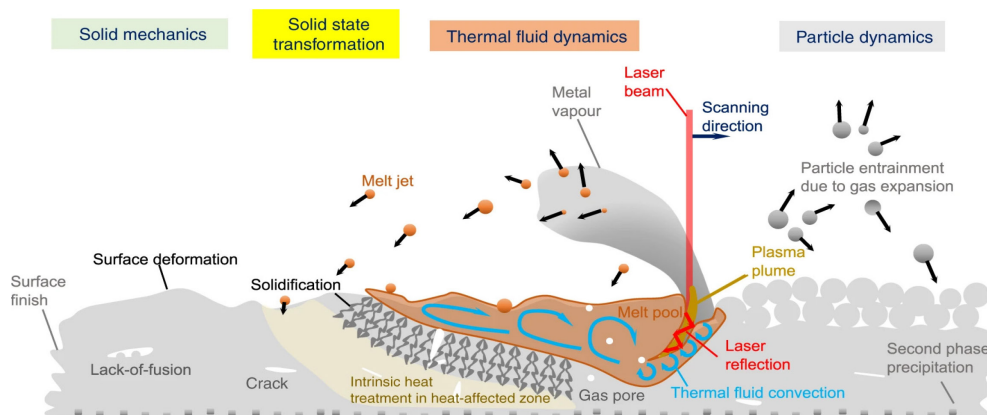


Figure 1-3: Complicated physics around the melt pool [19].

The investigation of process-structure linkages is crucial for refining processes and optimizing microstructures, which, in turn, is vital for bolstering quality control and ultimately enhancing the performance of the final products. Nevertheless, the intricacy of the AM process, as previously analyzed, poses considerable challenges in comprehending the interplay between the AM process and microstructure. This intricacy renders the exploration of microstructure evolution and optimization via the AM process notably more arduous compared to conventional manufacturing methods like casting and sintering. These challenges have the potential to stymie advancements in performance and curtail the widespread utilization of AM technologies. However, surmounting these challenges is imperative for fully harnessing the capabilities that AM technologies offer.

1.2.1 Motivation

Great efforts have been devoted to studying complex AM process-microstructure relations for common metals such as Ni-, Fe-, Al-, Ti-based alloys. The investigation of microstructures primarily encompasses (1) grain structures, (2) porosity, and (3) phase transformation. Extensive studies concerning grain structures have revealed that the columnar microstructures prevalent in AM-fabricated parts can be attributed to the layer-by-layer construction way, rapid cooling rates, and steep thermal gradients. Porosity is another well-studied aspect, where the formation of pores is often associated with insufficient energy input, gas entrapment during the AM process, and inconsistent powder characteristics, such as particle size and distribution. However, when it comes to phase transformation, the research is not as extensive. The complexity of the AM process, particularly the layer-wise stacking method, results in position-dependent thermal conditions. This raises critical questions: How do these unique thermal conditions affect phase transformation? Especially how to understand and validate the phase evolution pathways in the context of complex

physics (e.g., location-dependent thermal history and fast cooling rates) during the AM process involving multi-phase metals like Ti-6Al-4V?

Furthermore, AM techniques inherently excel at fabricating bimetallic structures, a domain where process-microstructure relationships remain ambiguous due to the dynamic variations in spatiotemporal composition throughout the AM process. Bimetallic structures, which enable location-specific properties, are prevalently found in functional materials, component repair, and welding joints. As a result, numerous bimetallic structures have been explored through AM techniques, particularly DED, but the emphasis has predominantly been on understanding and mitigating crack formation at the interfaces. The main reason is that the intricate interplay of compositions in bimetallic structures can often give rise to new brittle phases and facilitate crack initiation. Notably, the fluid convection within melt pools during the AM process tends to encourage a redistribution of spatially dependent compositions. This creates a novel mixing zone at the interface, which is distinct from the two parent materials and is a phenomenon that would not occur with a single metal due to its uniform composition. This would further raise the second question that is rarely mentioned in existing studies: how does the potential flow-driven compositional redistribution affect the microstructure evolution at the bimetal interface during AM process?

Finally, the traditional approaches of employing experimental studies and physical modeling to analyze microstructure evolution in the multifaceted AM processes are not only costly but also time-consuming due to the trial-and-error nature of experimentation and extensive physical modeling phases. Recently, the advent of smart manufacturing has brought data-driven modeling to the forefront, positioning it as an efficient, cost-effective alternative with extensive applicability within the manufacturing sector. Data-driven modeling, by leveraging the power of

data analytics, offers a more streamlined approach to understanding and optimizing complex manufacturing processes. This emergence of data-driven modeling in the manufacturing arena gives rise to the third pertinent question of this study: How can the cost-effective and expedited capabilities of data-driven modeling be harnessed to accelerate the elucidation and establishment of complex AM process-microstructure relationships, ultimately contributing to more efficient microstructure optimization and quality control?

1.2.2 Thesis Objectives

This study aims to provide insight into relationships between complex AM processes and microstructures for single metals and bimetallic alloys. Through experiments, physical modeling, and data-driven modeling, this study would finally contribute toward the extended understanding of microstructural evolution and optimization during AM metallic materials. The specific objectives of this study, as framed by the three previously stated questions, are as follows:

1. Identify phase evolution paths for as-built AM-ed Ti-6Al-4V featured with multiple phases using Finite Element Method (FEM)-based thermal simulation and Gleeble-simulator designed experiments.
2. Quantitatively investigate grain nucleation and growth in AM-fabricated bimetallic structures composed of SS316L and IN625 using Computational Fluid Dynamics (CFD) and Phase Field Method (PFM) simulations.
3. Utilize machine learning to enhance the prediction of melt pool characteristics during the additive manufacturing of IN625.

1.3 Outline of this dissertation

- ❖ Chapter 1 introduces metal additive manufacturing, its complexities, the motivations, and objectives of this study.

- ❖ Chapter 2 provides a literature review on microstructure problems in AM-fabricated single metals and bimetallic structures and identifies the questions in current research.
- ❖ Chapter 3 investigates phase transformation pathways in AM-fabricated Ti-6Al-4V by combining experiments with the Gleeble simulator and FEM thermal simulation.
- ❖ Chapter 4 studies the grain nucleation and growth of AM-ed bimetal structures composed of SS316L and IN625 using CFD and PFM simulations.
- ❖ Chapter 5 focuses on enhancing melt pool prediction through machine learning, including input feature design and data denoising.
- ❖ Chapter 6 provides conclusions and future work.

Chapter 2: Literature review

2.1 Additive manufacturing process effect on single metal microstructures

2.1.1 Grain structure

In additive manufacturing (AM) of metallic alloys, two types of grain structures, columnar and equiaxed, typically form and vary in location [20]. Columnar grains predominantly form in the main body, as illustrated in Figure 2-1, a consequence of epitaxial growth encouraged by high thermal gradients and slower cooling rates [20]. This epitaxial growth is sustained in the layer-by-layer deposition process, where melt-back of portions or the entirety of the previously deposited layer is essential and can be achieved through substantial energy input by increasing power levels [21][22]. During epitaxial growth, competitive grain growth can also occur. The columnar grains, favoring orientations such as $\langle 100 \rangle$ for fcc and bcc metals and $\langle 1010 \rangle$ for hcp metals, align with the maximum temperature gradient, thus outcompeting and crowding out other orientations [20][23]. Conversely, equiaxed grains primarily develop in the initial layers in contact with the substrate, and also in the top layers. The formation of equiaxed grains in the initial layers is a consequence of rapid heat dissipation into the substrate, leading to lower thermal gradients and higher solidification rates [24]. Additionally, partially melted powder can act as grain nuclei, further promoting the formation of equiaxed grains, especially in the top layers [25].

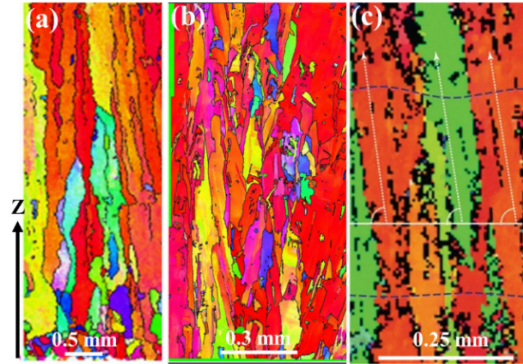


Figure 2-1: EBSD maps of β -grain structures for AM-ed Ti6Al4V [26], Inconel 625 [27] and AlSi10Mg [28].

To mitigate the anisotropic properties associated with columnar grain structures, columnar to equiaxed transition (CET) are normally encouraged. CET is closely related to the thermal gradient (G) and the growth interface velocity (R), both of which can be deftly manipulated through AM processes to modify the thermal conditions conducive to this transition. In this context, G - R maps have become an important tool in analyzing and understanding the regions where columnar-to-equiaxed transitions occur [29][30][31]. An effective proven strategy for inducing CET within the melt pool involves spot melting, such as point exposure scanning or the use of pulsed lasers [32], enabling maintaining a low G/R ratio [24][33]. Additionally, fine-tuning of parameters such as laser power, preheating temperature, and scanning speed is advised to further optimize the process [34]. Beyond these strategies, there are innovative methods to modulate the melt pool and enhance CET, which include (1) employing high-intensity ultrasound, where cavitation stirs the melt and activates nuclei [35], and (2) introducing foreign nucleant particles to augment the nucleation rate [36].

2.1.2 Porosity

Stacking manufacturing way decides that AM products are susceptible to the high risk of porosity. As shown in Figure 2-2, the porosity observed can be classified into two distinct categories based on their shape: spherical pores and irregular pores. Spherical pores are typically the result of gases becoming trapped during the process, attributed to factors such as moisture,

Marangoni convection, or material evaporation, and are primarily located within molten tracks [37]. On the other hand, irregular pores are largely the result of incomplete fusion or melting and insufficient hatching distances, and are predominantly situated at the boundaries of molten tracks, as depicted in Figure 2-2a.

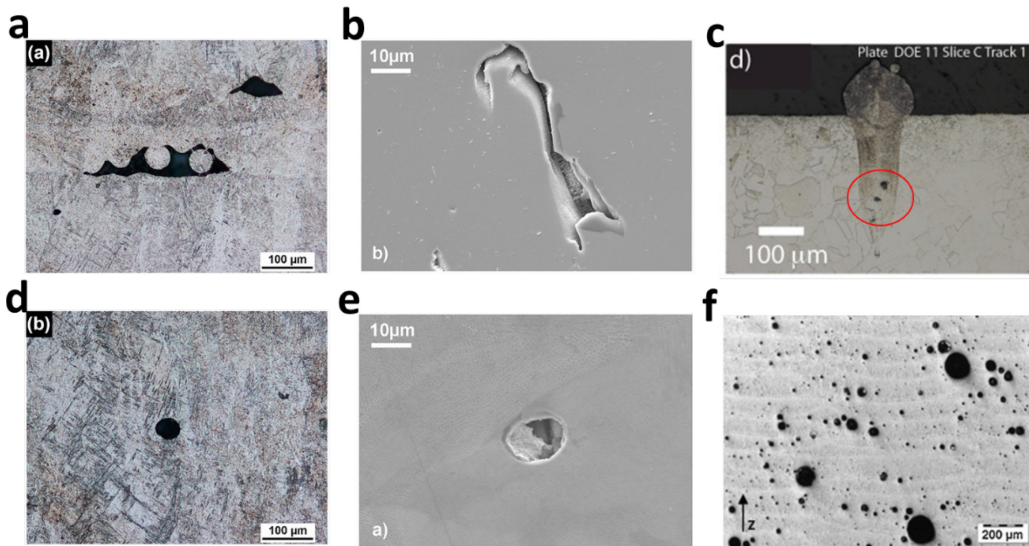


Figure 2-2: Visual examples of various types of pores in AM-produced metals: (a) lack-of-fusion pores in AM-ed Ti6Al4V [38] and (b) in IN 718 [39], (c) keyhole pores in AM-ed Ti6Al4V, gas pores in (d) AM-ed Ti6Al4V [38] and in (e) IN 718 [39], and (f) hydrogen porosity in AM-ed AlSi10Mg [40].

It has been widely proved that the formation of pores is intricately linked to various aspects of the AM process, encompassing processing parameters, feedstock properties, and the ambient atmosphere within the chamber [41]. Elevated energy input, for instance through higher laser power, can induce metal evaporation, vapor cavities, and the entrapment of vapor within the melt pool, resulting in keyhole porosity (Figure 2-2c). Conversely, inadequate energy input can lead to incomplete melting of the powder, culminating in lack-of-fusion porosity. Striking the right balance in processing parameters is thus critical in mitigating pore formation [42]. Implementing preheating and drying procedures can lower moisture content, which is especially pertinent in decreasing hydrogen-related porosity (Figure 2-2f) in aluminum-based products [41]. Additionally, maintaining a stringent inert atmosphere is crucial in minimizing oxidation, ensuring proper

wetting, and promoting bonding between powder particles [22]. Furthermore, post-processing techniques such as hot isostatic pressing (HIP) are commonly employed to reduce residual porosity [43].

2.1.3 Phase

Phase research of AM-ed metallic products is quite complex in that (1) the diversity of metals being printed, many of which are multi-component and/or multi-phase in nature, (2) the dynamic thermal conditions experienced during the AM process, including rapid melting, solidification, and layer-wise thermal histories, and (3) different post-heat treatments employed. In particular, dynamic thermal conditions introduce complexities in phase evolution compared to traditionally cast counterparts. This complexity in phase diversity is especially pronounced in multi-phase alloys such as Ti-based and Fe-based alloys in comparison to others like Ni-based alloys. In this section, three common alloys used in AM - Ti-6Al-4V, SS316L, and IN625 - are reviewed as representatives for examining phase studies.

2.1.3.1 Ti-6Al-4V

Ti-6Al-4V, often referred to as TC4, is a prevalent titanium alloy notable for its exceptional fatigue behavior, strength-to-weight ratio, toughness, corrosion resistance, and biocompatibility, making it suitable for aerospace and medical applications [44]. As depicted in the phase diagram of Figure 2-3a, during cooling, the body-centered-cubic (BCC) beta (β) phase transforms into a hexagonal-close-packed (HCP) alpha (α) phase beyond the β transus point (T_{β}). However, the alpha phase can further evolve into diffusion-controlled α , and massive (α_m) and martensitic (α') phases depending on cooling rates as shown in Figure 2-3b, which represents a continuous cooling transformation (CCT) diagram. Table 2-1 summarizes the typical transformation products that arise at different cooling rates when cooling Ti-6Al-4V from T_{β} , which is also instrumental in

phase studies for AM-produced Ti-6Al-4V. Corresponding morphologies are illustrated in Figure 2-4.

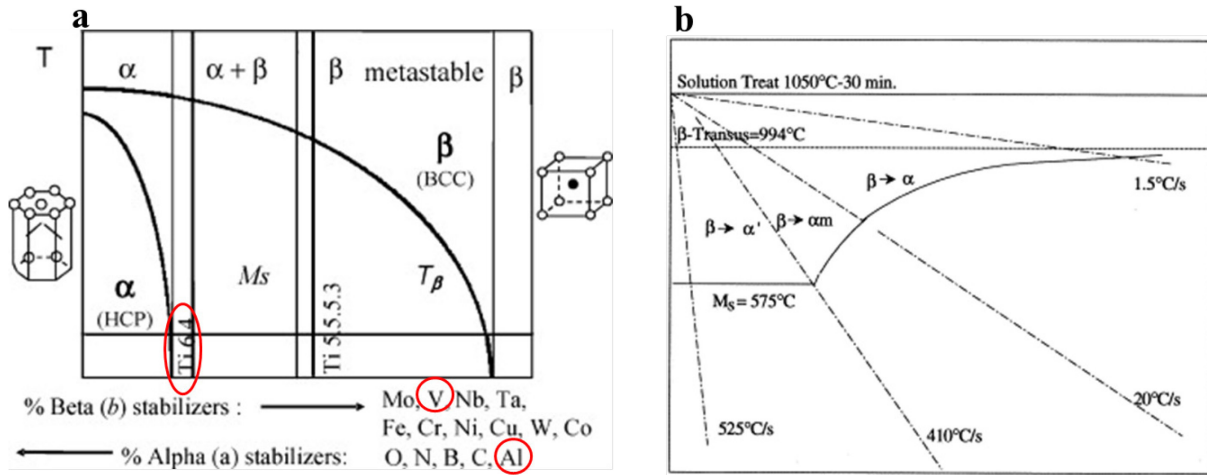


Figure 2-3: (a) Phase diagram of the titanium alloys [45], and (b) Schematic continuous cooling diagram for Ti-6Al-4V β -solution treated at 1050°C for 30 min [46].

Table 2-1 Characteristics of the products cooling form Beta phase [46][47].

| Condition number | Cooling Rate ($^{\circ}\text{C}/\text{s}$) | Transformation products | Morphologies |
|------------------|--|-------------------------------|--|
| 1 | >410 | Martensitic α' | Orthogonal α' plate |
| 2 | 25~410 | Massive α_m | Blocky α |
| 3 | < 25 | Diffusion controlled α | Sideplates along boundaries Colony morphology Basketweave morphology |

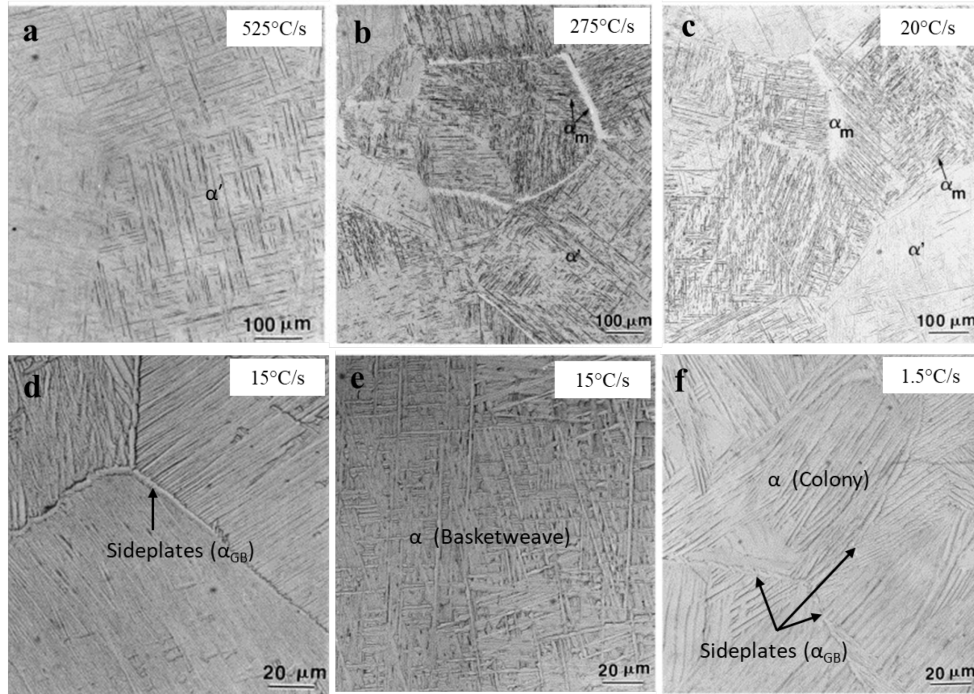


Figure 2-4: The typical Optical micrographs of various cooling products [46]

During the AM process, feedstock powders of Ti-6Al-4V are rapidly melted into the β phase to form melt pools, which undergo cyclical, extremely rapid cooling and heating due to consecutive layer deposition. The dominant phase, generally observed as martensitic α' due to the inherently high cooling rates ($\sim 10^5$ K/s) in small, localized melt pools, is displayed in Figure 2-5a [44][48][49][50][51][52]. To achieve the desired $\alpha+\beta$ phase products with well-rounded mechanical properties, AM processes, including focal offset distance and energy density adjustments [53], and selective laser melting (SLM) processing routes [54] are optimized for the *in-situ* transformation of martensite into lamellar $\alpha+\beta$ phases (see Figure 2-5b). Additionally, post-heat treatments can facilitate the formation of $\alpha+\beta$ [48][55] and a novel phase combination of $\alpha+\alpha'$ [56][57], as shown in Figure 2-5c. Other mixed phases are obtained in as-built samples like α' and $\alpha+\beta$ [58], and α' , α_m , and $\alpha+\beta$ [59].

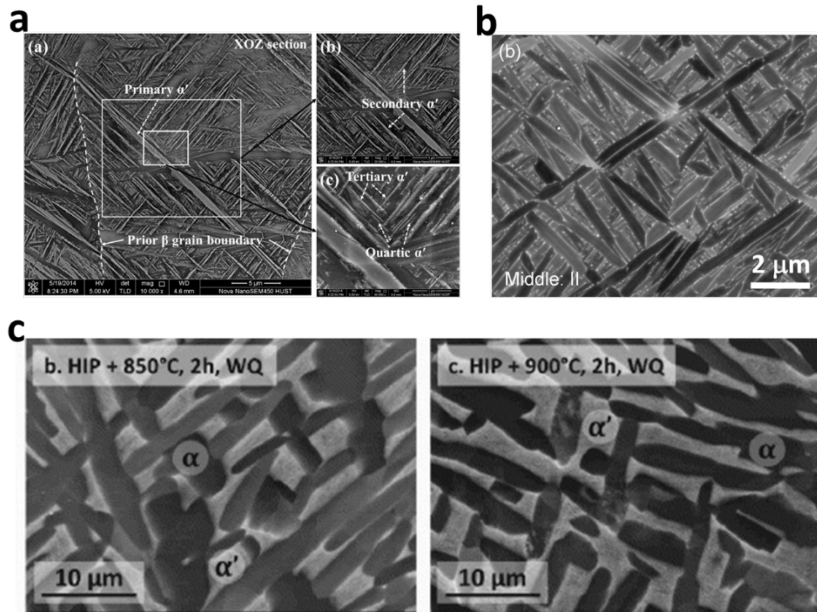


Figure 2-5: (a) SEM images of various α' phases in as-built Ti-6Al-4V [51], (b) finer lamellar $\alpha+\beta$ phases through *in-situ* martensite decomposition [53], and (c) $\alpha+\alpha'$ phases through heat treatment [57]

2.1.3.2 SS316L

316 stainless steel (SS316L) is an important member of the austenitic stainless steel family, valued for its excellent weldability, machinability, and corrosion resistance, making it widely used in chemical, pharmaceutical, and food industries [60][61]. Unlike Ti-6Al-4V, martensitic phases are rarely observed in as-built SS316L, even at high cooling rates during the AM process, due to the high content of austenite stabilizers such as Ni and Cr [62][63] and low M_s temperature (normally below room temperature [64][65]). Generally, only the face-centered cubic (FCC) austenite (γ) phase is observed, as confirmed by X-ray diffraction (XRD) studies [61][62][66][67], as shown in Figure 2-6a. Occasionally, trace amounts of ferrite (δ) phases with body-centered cubic (BCC) structures are detected [61][68]. Figure 2-6b illustrates that the phase composition of as-built 316L is predominantly austenite, with ferrite content less than 0.1%, which is below the XRD detection limit [61]. High-resolution TEM-EDX analysis reveals a high degree of chemical homogeneity in as-built 316L samples, with no evidence of micro- or nano-segregation [69]. In addition, participants like Si- and Mn-oxides form and distribute randomly in the samples [69].

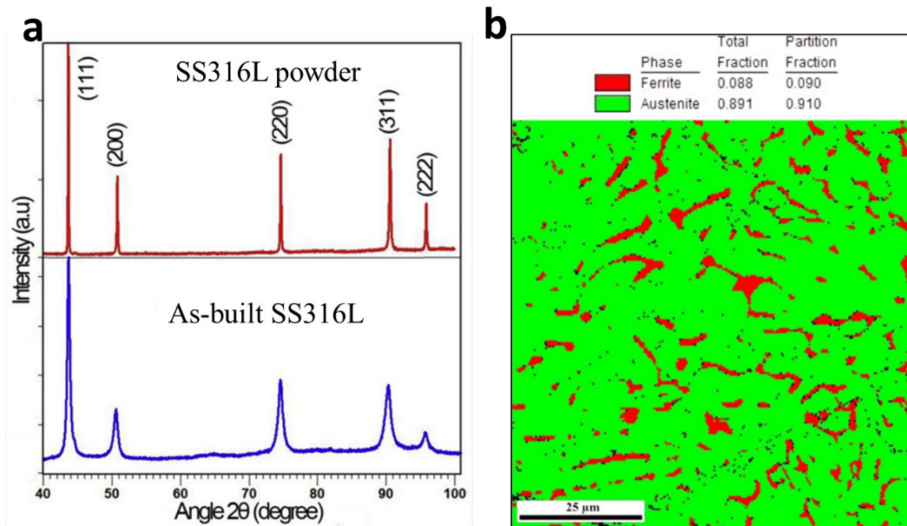


Figure 2-6: (a) XRD patterns of the SS316L precursor powder and the as-built SS316L [67] and (b) EBSD phase fraction map of a selected area in as-built SS316L (red: ferrite; green: austenite) [68].

2.1.3.3 IN625

In contrast to Ti-6Al-4V, IN625 primarily exhibits a face-centered cubic (FCC) structure within the Ni-Cr matrix and incorporates multiple elements such as Nb, Mo, Fe, Mn, and Si for solution strengthening. The alloy's mechanical properties are related to the precipitation of fine intermetallic phases (γ' [Ni₃Nb]) and carbides (MC, M₆C, and M₂₃C₆) during annealing at temperatures ranging from 550 to 850°C over an extended period [70]. The alloy performs well in terms of corrosion resistance, fatigue, and mechanical strength at high temperatures, making it ideal for high-temperature and high-pressure applications such as in aerospace and nuclear industries [71].

As shown in Figure 2-7a, the AM process tends to result in elemental segregation, particularly of Nb and Mo, during the printing of IN625 due to the rapid cooling rates. This can lead to the formation of undesired phases. In particular, the brittle Laves phase, denoted as (Ni, Cr, Fe)₂(Nb, Mo, Ti), can form interdendritally due to the rapid cooling rates, as shown in Figure 2-7b. The formation of the Laves phase consumes matrix strengthening elements such as Nb and Mo, inhibiting the formation of γ' (Ni₃Al(Ti)) and γ'' (Ni₃Nb) [70]. This can soften the matrix and

adversely affect mechanical properties [71][72]. Post-heat treatments are often employed to homogenize elemental segregation [73] and facilitate the dissolution of the Laves phase [70]. This may lead to the precipitation of carbides [71][74] (as seen in Figure 2-7c) and δ -phase [75] (as seen in Figure 2-7d).

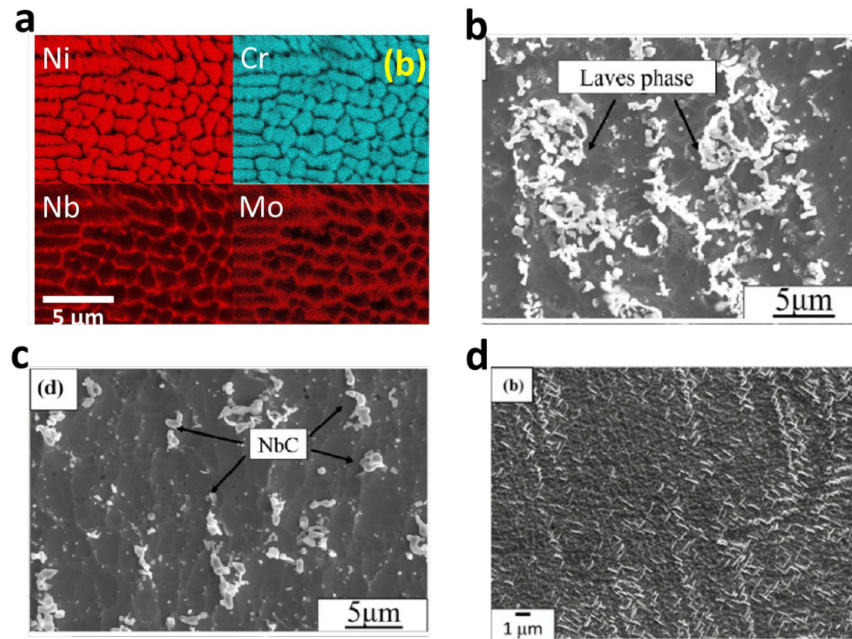


Figure 2-7: (a) Elemental X-ray maps of as-built IN625 sample [73], (b) SEM images of as-built IN625 to show the Laves phase [76], (c) SEM images of solution treated IN625 (1050 °C for 2 h) to NbC and (c) Microstructure of AM-ed IN625 after heat treatment of 1 h at 870 °C to show δ -phase [75].

2.1.4 Question 1 to be Addressed

As reviewed in section 2.1, there has been substantial research and progress in understanding and controlling grain structures and porosity in additively manufactured (AM) metals. However, phase transformation, especially under the complex thermal conditions inherent in AM, has not garnered as much attention. The layer-by-layer fabrication process in AM leads to position-dependent thermal histories, and consequently, it is possible for different layers to experience different thermal treatments. This complexity poses a significant challenge in predicting and controlling microstructural evolution, which is also the reason why some cases show position-dependent phases. Thus, the question that arises is: How can the phase evolution

pathways be understood and validated, particularly in light of the complex, location-dependent thermal histories and rapid cooling rates in AM? Further research is required to decipher the interactions between these thermal conditions and phase transformations, ultimately aiming to facilitate the tailoring of microstructures to optimize the properties of the final product, such as in the case of Ti-6Al-4V. (e.g., Ti-6Al-4V).

2.2 Additive manufacturing process effect on bimetal microstructures

Bimetallic structures mainly feature utilization of two or more different materials for a layer-wise build-up, widely existing in functionally graded materials (FGM) and dissimilar material joints. This unique structure enables offering user-definable and spatial position-dependent properties, thus meeting some special applications, such as nuclear plant and aerospace components [77], repair [16], and welding [78].

Additive manufacturing (AM) techniques, particularly Direct Energy Deposition (DED), have been pivotal in streamlining the exploration and fabrication of bimetal structures. Examples include combinations like Ti-6Al-4V/Invar 36 [11], Ti-6Al-4V/304L [12], 304L/Invar 36 [13], IN718/copper alloy [79], and SS316/SS430 [80]. During the DED process, localized, successive, and diminutive melt pools are generated with high-power-density beams (e.g., laser and electron beams) and powder/wire feeding systems equipped with multiple nozzles moving coaxially. As a result, the spatial change of different materials and their contents are easily achievable via the continuous solidification of melt pools containing varying components, thus allowing the layer-by-layer formation of various bimetallic structures even in one object. Thus, the DED method is inherently suitable for building bimetal structures compared to conventional fabrication methods such as sintering [81].

Similar to dissimilar welding, a critical challenge in bimetallic structures is the susceptibility to cracking at the interface, which is often attributed to (1) the mismatch of thermal properties and immiscibility of constituent materials, and (2) the formation of detrimental phases. In a study attempting to construct a bimetallic structure of IN718 and Ti64, three build strategies were explored, including direct deposition, compositional gradation, and the use of an intermediate bond layer [82]. The results show that delamination occurs when directly depositing IN718 on Ti64 mainly due to the first reason. The second strategy also results in crack propagation and complete de-bonding at the region of 40–60 wt% IN718 due to the brittle intermetallic phase. However, employing vanadium carbide mixed with parent alloys as an intermediate layer proved successful in bonding the two immiscible alloys.

Actually, the compositional gradation at the interface is usually created to avoid direct contact of two metallic materials, like most FGMs, to mitigate the properties mismatch. However, cracks and detrimental phases are still observed near the interface. For example, Fe-Ti intermetallics and σ -FeV phase are considered to account for the crack at the transition from 25 vol% Ti-6Al-4V/75 vol% V to 25 vol% SS304L/75 vol% V and 25% SS304L/75% V to 50% SS304L/50% V [12], while a secondary phase of (Mo, Nb)C was identified as the cause of crack development near the 82 wt% SS304L/18 wt% IN625 region in another study [14]. Intermetallic phases (FeTi, Fe₂Ti, Ni₃Ti, and NiTi₂) have been considered why FGM cracked during the AM process.

2.2.1 Question 2 to be Addressed

As reviewed above, the research of AM-ed bimetallics mainly focuses on the study to avoid the formation of detrimental phases and reducing crack susceptibility. However, the grain structures that form in the melt pool at the interface have garnered rarely attention. The as-mentioned complex physic, especially the fluid convection in melt pools, would cause

compositional redistribution and generate a different mixing zone from two-parent materials, which does not work during the single metal AM due to identical composition distribution everywhere in the melt pools. So, this raises an imperative question: How does flow-driven compositional redistribution influence microstructure evolution at the bimetal interface, and how can this be quantitatively analyzed and understood? Further investigation into this phenomenon is necessary to optimize the properties and performance of AM bimetal structures.

2.3 Optimization of microstructure by controlling melt pool.

The melt pool, as an important AM process signature, has been proved to play a vital role in the microstructure and properties of AM-ed parts [83][84][85][86]. During the AM process, tiny melt pools are continuously formed along a computer-designed scan path under the exposure of high-density-power beams (e.g., laser beams). At the same time, metallurgic bonding occurs between adjacent melt pools in a track-wise (same layer) and layer-wise (different layers) way to form the final product. In this way, inappropriate melt pool sizes would provide many opportunities for defect generation (e.g., pores) and lead to poor performance. On the one hand, the melt pool with a small size would cause insufficient pool overlapping, resulting in incomplete melting and thus porosity formation [84][87]. On the other hand, the large melt pools arising from high energy inputs are likely subjected to keyhole issues [88], which would also cause excessive porosity [89]. These porosities would reduce the properties like tensile strength, fatigue limit, and corrosion resistance [90]. In addition, oversized melt pools easily cause much thermal loading to adjacent areas, increasing strain aging [91][92] pool. Large melt pools also likely worsen the surface quality [93]. Therefore, melt pools enable building a key bridge for the study of the AM process-microstructure relation [65]. Enabling control of the melt pool, including the prediction

and adjustment, is of great importance to avoid the porosity for microstructure optimization and ensure quality control.

Physics-based modeling is a common approach that can be used to predict melt pools. In contrast to very expensive trial-and-error experimental methods, it provides an in-depth and quantitative understanding of the various physical phenomena associated with the melt pool (e.g., heat transfer and convection). In this case, the prediction of the melt pool at different printing conditions can be physic-informed rather than heavily relying on trial-and-error experiments. A simulation combining a finite difference method and a combined level set volume of fluid method, for example, can easily show that suitably increasing scanning speed could avoid cavity evolution and lead to a shallow lens-like melt pool [94]. However, high computational costs have been considered to hinder the widespread use of physics-based modeling [95]. For this reason, simplifications and assumptions such as using the 2D simulation domain, reducing the number of tracks and layers [42][24], and ignoring unimportant physics [96] have been commonly made, which, however, may cause significant model discrepancy with AM practice. Therefore, a cost-saving and reliable alternative for melt pool prediction is urgently needed, and data-driven modeling is probably the most promising one so far, as it can provide faster and cheaper computation [97].

2.3.1 Question 3 to be Addressed

As reviewed above, data-driven modeling has the potential to fast build the relations between AM process and microstructures, facilitated by the melt pool as an intermediary. The dimensions of the melt pool, such as its width, length, depth, or area, can be easily quantified. Furthermore, these dimensions have been found to be intricately linked with the evolution of specific microstructures, including columnar grain structure [98] and porosity [99]. Nevertheless,

traditional methods such as regression analysis or curve fitting prove inadequate for capturing the intricate physics inherent in the AM process. To achieve a better and highly accurate prediction and adjustment of the melt pool, the raised third question of this study is how to build inexpensive and fast data-driven modeling, including input design, to figure out the complex AM process-melt pool relationships, which then guide the microstructure optimization and quality control?

2.4 Common Methods used for microstructural development understanding

2.4.1 Experimental methods

Extensive experimental research has been undertaken to investigate microstructural features. Conventional methods for examining microstructure morphology involve the use of optical microscopy (OM), scanning electron microscopy (SEM), and transmission electron microscopy (TEM). Electron backscatter diffraction (EBSD) is employed for texture analysis, while X-ray diffraction (XRD) is utilized for phase identification. These experimental techniques offer valuable insights into the microstructural characteristics of materials processed through AM.

2.4.2 Physical modeling

Physical or physics-based modeling is a widely used approach to simulate the evolution of microstructures in both time and space during the AM process. The primary models for grain structure simulations include phase-field models (PFM) [20][24][100][101], cellular automata (CA) models [102][103][104] and Monte Carlo (MC) models [105][106]. In these models, thermal data is usually sourced from thermal-finite element simulations or thermal-computational fluid dynamics simulations. Phase-field models, in particular, have been employed to study the grain structure, porosity [42] and phase transformation [107].

2.4.3 Data-driven modeling

Data-driven modeling has garnered considerable attention in the AM community, with broad applications ranging from uncertainty quantification [108][109], classification [85][110], to prediction [111][112]. Researchers like Wang et al. have developed multilevel data-driven surrogate models to study uncertainty propagation, from process parameters to mechanical properties [113]. These models are capable of replacing intricate multi-physical models, such as thermal, grain growth, and elasto-viscoplastic models, to study the general process-structure-property (PSP) relationship [114]. The growing trend in utilizing various monitors in the AM community has made the collection of abundant experimental data easier, furthering experimental data-driven modeling development. Mohammad et al. succeeded in using acoustic emission monitoring with machine learning for online defect detection [115], while Jamison et al. utilized two CCD cameras to obtain 3D-digital image correlation data, further employing a trained Naïve-Bayes classifier to predict defect likelihood [116]. Among these applications, data-driven predictive modeling of melt pool characteristics, such as size, has garnered significant attention. Therefore, the study of microstructures in additive manufacturing is facilitated through a variety of methods, including experimental, physical modeling, and data-driven modeling. The combined use of these methods can lead to deep and comprehensive understanding of microstructural development and optimization in AM.

Chapter 3: Phase evolution of AM-ed Ti-6Al-4V by a Gleeble and FEM-assisted methods

3.1 Introduction

3.1.1 Background

For the first question, complicatedly position-dependent thermal conditions could complicate the microstructure, especially the phase transformation, which is has been proven by the diversity of phases, especially for the Ti-6Al-4V through the literature review. Unlike their casting counterparts, in which the expected $\alpha+\beta$ phases could be easily obtained thanks to the continuous cooling curve, AM-fabricated Ti-6Al-4V components are subject to complicated non-equilibrium thermal cycles (TCs); thus, it is hard to directly achieve the $\alpha+\beta$ phases. To transform α' and α_m phases to be $\alpha+\beta$ phases, we usually resort to post-processing like annealing, which, however, would incur an additional cost. Nevertheless, if we well understand the mechanism of how TCs impacts phase evolution, it is possible to control the resulting phases in an as-fabricated build.

TCs in AM, which originated from layer-wise printing under non-equilibrium thermodynamic conditions, shows two important characteristics, i.e., (1) periodical attenuation and (2) location dependence. Specifically, a fast heating rate, a high peak temperature, and a high cooling rate are present at the early stage, which are gradually degraded as the subsequent layers are deposited [117][118]. Moreover, different positions experience different temperature evolutions, i.e., position-dependent TCs. These characteristics have been demonstrated to affect the phase transformation at different locations significantly. The periodic attenuation of TCs would mainly lead to the gradient size of the α phase. For example, Galarraga et al. have found that α -

lath thickness varies with distance from the build platform [38]. Kelly et al. also have reported a gradient in the individual α -lath thickness between the deposited layers [119]. The location dependence of TCs usually results in site-specific phases. Lu et al. [59] found that the bottom of the printed part shows an $\alpha+\beta$ structure, but the top exhibits α' zone and $\alpha'+\alpha_m$ zone. Hence, all those experimental facts demonstrate a high possibility of forming an inherent gradient structure once using the AM method for building Ti-6Al-4V. However, the corresponding mechanism due to the TCs remains unclear. In fact, most researchers are mainly struggling with viably experimental methods to obtain the $\alpha+\beta$ structure. For example, they have adjusted manufacturing conditions like focal offset distance, energy density, layer thickness, inter-layer time, and part dimension to achieve $\alpha+\beta$ structure during AM [53][54][120]. Therefore, they are experimental-oriented and rely on trial-and-error or similar empirical knowledge without taking advantage of the role of TCs in the control of resulting phases. This is primarily because real-time monitoring, like infrared (IR) cameras [121] is normally cost-intensive, and thermocouples are sometimes limited because they are mostly mounted on the substrate [122][123][124].

Recently, we have experimentally found a gradient structure (~ 10 mm) composed of $\alpha+\beta$, $\alpha'+\alpha_m$, and α' zones along the building direction on the top of AM-ed Ti-6Al-4V, which is different from the gradient (mainly in α -lath thickness) studied by Kelly's [119]. It was also observed by Lu et al. [59] but without a comprehensive understanding. So, in this chapter, we aim to uncover how TCs affect the phase evolutions and act on this gradient structure formation by taking advantage of Gleeble-designed experiments, computational simulation, and thermodynamic methods. The gradient structure (~ 10 mm) is first characterized by optical microscopy, scanning electron microscopy, X-ray diffraction, and the Vickers hardness tester. To highlight the impact of the TCs, the water-quenched Ti-6Al-4V sample by Gleeble is compared with the AM-ed

counterpart. Then, the relationships between gradient structure, phase evolution, and TCs curves from the thermal simulation are systematically built on understanding the mechanisms of the phase evolution during AM of Ti-6Al-4V. Furthermore, another two Gleeble-assisted experiments are designed to explore the potential phase evolution existing in AM. Lastly, thermodynamic analyses are conducted to demonstrate the possible phase transformation.

3.2 Experimental methods

3.2.1 Directly laser deposition process of Ti-4Al-4V

The AM cylinder is built by Optomec LENS 750 with a typical processing condition, including a scan speed of 17 mm/s and a laser power of 350 W (more processing details [121]). Normally, the layer thickness of directed energy deposition (such as DLD) is 0.3-1 mm, which is higher than that of powder bed fusion (PBF) (tens of microns) [125]. Herein, the layer thickness is set to 0.508 mm. The obtained top part with approximate $\Phi 7 \times 25$ mm in size is shown in Figure 3-1a.

3.2.2 Gleeble experiments

Gleeble 3500D offers an alternative solution to explore the phase evolution that occurs during AM Ti-6Al-4V. As a physical simulator [126][127], Gleeble 3500D can be leveraged to design experiments, specifically the imitation of the fast heating and cooling processes. Also, highly sensitive thermocouples enable us to capture the real-time variation of temperature. Therefore, Gleeble has been widely employed to design controlled processing for the investigation of phase evolutions [128][129]. One typical example is that Kelly has used Gleeble 1500 to get two thermal cycles, in which the slow cooling rates (≤ 10 K/s) are used [130]. To further enhance the Gleeble-designed experiments, more than two TCs with an interval time of about several seconds and a fast cooling rate can be tailored using Gleeble to mimic the TCs of AM. This allows

for a comprehensive study correlating the gradient structure, TCs, and phase evolution during AM of Ti-6Al-4V.

For the Gleeble experiments in this study, as-received Ti-6Al-4V plates purchased from Sigma-Aldrich Inc are machined to a small cubic sample ($9 \times 9 \times 9$ mm) by a diamond blade to ensure fast and uniform heating and cooling process. Hence, the temperature difference between the outer surface and the center of Gleeble-treated samples can be ignored. As illustrated in Figure 3-1b, the cubic sample is sandwiched by graphite electrodes for the current flow. During the heating and cooling process, the chamber is full of argon to avoid oxidation. Also, the temperature is in-situ monitored by thermocouples that are welded (similar method with [46]) on the surface of cubic samples and recorded by the data acquisition system of Gleeble [131] for analyzing the cooling rate. There are three kinds of Gleeble-treated samples; (1) water-quenched sample: the machined cubic sample is heated up to 1100 °C for 10 minutes, followed by quenching with high-speed water flow; (2) air-quenched sample: the machined cubic sample is heated up to 1100 °C for 10 minutes and then cooled by airflow; (3) TCs-treated sample: the machined cubic sample is quickly heated to 1100 °C and then gas quenched using pressurized argon nozzles at a sufficient rate to ensure martensitic transformation, followed by 800 °C annealing for a few seconds (more processing details [132]). This heating-quenching-fast annealing process, which is equivalent to one TC, has been repeated up to four times. The water-quenched sample is compared with the DLDed sample (sections 3.4.1 and 3.4.2). The rest of the Gleeble-treated samples are specifically analyzed in section 3.2.1 about verifying the possible phase evolution during AM of Ti-6Al-4V.

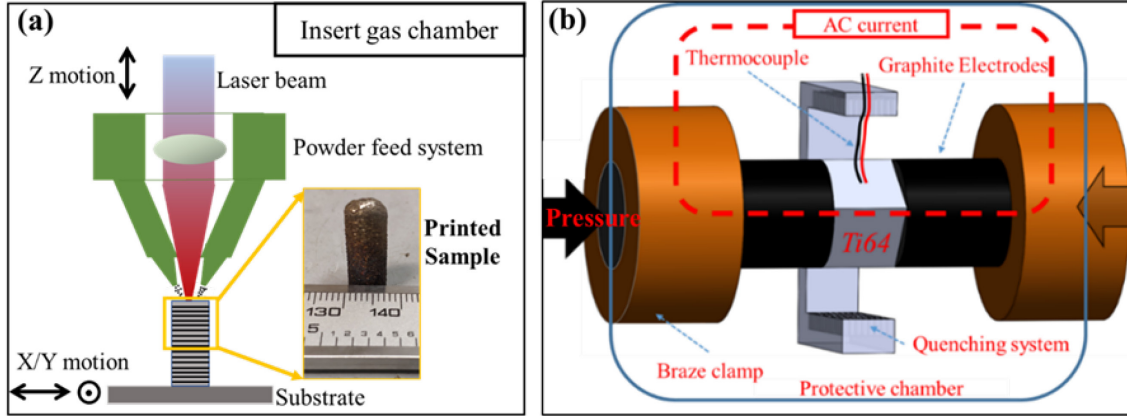


Figure 3-1: (a) The schematic diagram of the LENS machine with DLDed samples, and (b) Gleeble 3500D with a cubic sample.

3.2.3 Characterization of the microstructure and mechanical testing

The DLDed samples (the top part about 10 mm in height) and Gleeble-treated samples are cut to get a fresh cross-section and then ground using Struers Tegrapol-11 Polisher, followed by polishing with Buehler VibroMet-2 Polisher. The polished specimens are examined by X-ray diffraction (XRD) and then etched with Kroll's reagent of 2 ml HF, 4 ml HNO₃ and 50 ml H₂O for 25s. Ultrasonic cleaning is performed for optical microscopy (OM) and scanning electron microscopy (SEM). Also, a Leco Vickers Microhardness Tester (LM-300AT) is used for examining the properties. ImageJ software is used to analyze the size of various phases.

3.3 Computational method: thermal modelling

A finite-element-based simulation model based on the element birth and death technique [133][134] is applied to investigate the TCs during the DLD process quantitatively. A transient temperature distribution $T(x,y,z,t)$ is simulated by solving the following Eq. (3-1) governing heat transfer energy balance:

$$\rho C_p \frac{dT}{dt} = \nabla \cdot (k \nabla T) + Q(x, y, z, t) \quad (3-1)$$

where k , ρ , and C_p are conductivity, density, and specific heat, respectively, as listed in Table 3-1. The input energy from the laser heat source (Q) [20][135] is calculated using a double ellipsoid model as an input in ABAQUS/2018 using a DFLUX subroutine [108], expressed as:

$$Q = \frac{6\sqrt{3}P\eta f}{abc\pi\sqrt{\pi}} \exp\left(-3\left[\frac{(x+vt)^2}{a^2} + \frac{(y+vt)^2}{b^2} + \frac{(z+vt)^2}{c^2}\right]\right) \quad (3-2)$$

Here, η and P represent energy absorption efficiency and laser power, respectively. The other parameters are tabulated in Table 3-2. Due to a lack of the preheating process [121], the initial boundary condition $T = T_a = 25$ °C (ambient temperature) is set for the substrate and all elements. During DLD, heat loss for deposited parts composed of convection and radiation are considered [58] for all surfaces that expose in an argon atmosphere, expressed as:

$$k\nabla T = -h \cdot (T - T_a) - \sigma\varepsilon \cdot (T^4 - T_a^4) \quad (3-3)$$

where h , ε , and σ are the heat convective coefficient, emissivity, and Stefan-Boltzmann constant, respectively. It should be noted that latent heat used for phase transformation is ignored [58] due to the negligible contribution compared with the heat source [20]. A relatively higher heat convective coefficient (h) compared with that used in PBF [117] is adopted considering the direct exposure of deposited parts to the atmosphere of argon flow instead of surrounding by loose powders during DLD. The built part is simplified into single-line built geometry to reduce computation time and achieve multiply layers depositions [118] and verified with experimental results [121] in section 3.1.1. Other simulation parameters are listed in Table 3-2.

Table 3-1 Coefficients for density, specific heat, and conductivity of Ti-6Al-4V [20][117].

| Material properties | Unit | Symbol | Value as a function of temperature (T) |
|---------------------|-------------------|--------|---|
| Specific heat | W/(m·K) | C_p | $531.1 + 0.1185T + 1.883 \times 10^{-5}T^2 - 7.921 \times 10^{-9}T^3$ |
| Conductivity | J/(kg·K) | k | $4.968 + 4.973 \times 10^{-3}T + 8.044 \times 10^{-6}T^2 - 2.008 \times 10^{-9}T^3$ |
| Density | kg/m ³ | ρ | $4.652 \times 10^3 - 0.9391T + 9.255 \times 10^{-4}T^2 - 3.133 \times 10^{-7}T^3$ |

Table 3-2 Processing parameters of the thermal model [20][117].

| Processing parameters | Unit | Symbol | value |
|-----------------------------|--|---------------|-----------------------|
| Laser power | W | P | 350 |
| Absorption efficiency | | η | 0.8 |
| Layer height | mm | | 0.5 |
| Scanning speed | mm/s | v | 17.0 |
| Beam diameter | μm | a | 200.0 |
| Penetration depth | μm | b | 20.0 |
| heat convective coefficient | $\text{W}/\text{m}^2 \cdot \text{K}$ | h | 12.0 |
| Emissivity | | ε | 0.49 |
| Stefan-Boltzmann constant | $\text{W}/\text{m}^2 \cdot \text{K}^4$ | σ | 5.67×10^{-8} |

3.4 Results

3.4.1 Phase and microstructures

The etched optical microscopy images of the water-quenched sample by Gleeble and the gradient structure for the DLDED sample are shown in Figure 3-2e and Figure 3-2b, which are used to characterize microstructural defects, grain size, and morphology in a macro size. Very few defects are observed in both samples, but the grain (refer to prior β grain herein) size and morphology are significantly different. Specifically, the DLDED sample shows two kinds of grain structures: (1) columnar structures on the edge side of DLDED samples (right side of Figure 3-2b) with about 45 degrees from the building direction (by red cycles about 1mm), and (2) equiaxed grains (about 400 μm) in the middle cross-section (left side of Figure 3-2b). For the water-quenched sample in Gleeble, as shown in Figure 3-2e, equiaxed grains prevail with a size of about 300 μm . However, before heat treatment, the as-received sample for the Gleeble experiment

(Figure 3-2d) shows typical rolled grain structures with elongated small grains. The change of grain shape is mainly attributed to a 10-min holding time at 1100 °C, leading to a complete β grain structural transformation and subsequent grain growth [44].

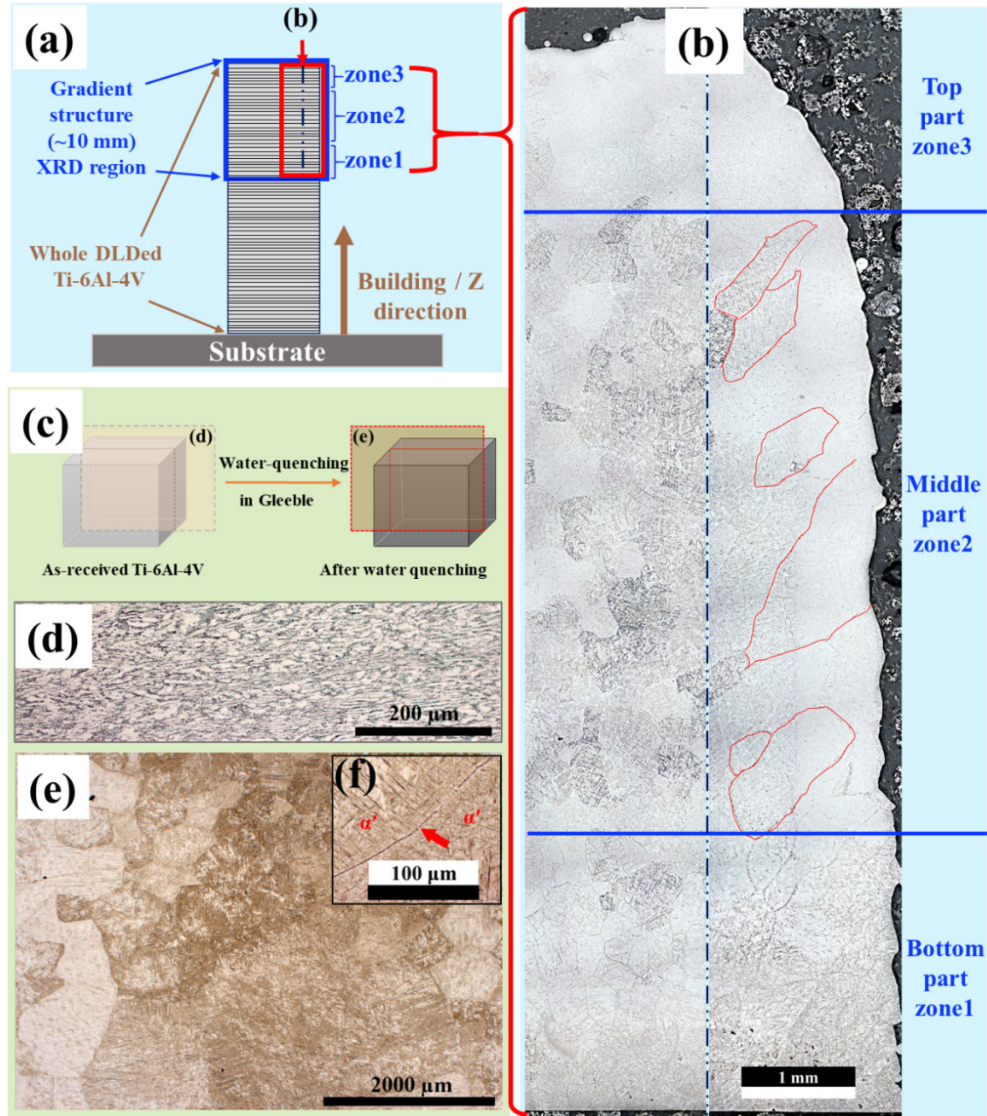


Figure 3-2: (a) the schematic of cross-section for DLDED Ti-6Al-4V, and (b) the optical microscopy (OM) characterization of the gradient structure in DLDED Ti-6Al-4V, as indicated by red rectangular box in (a). (c) the schematic of samples involved in Gleeble: (d) OM characterization of the as-received Ti-6Al-4V for the Gleeble experiment, (e) OM characterization of the water-quenched sample in Gleeble, and (f) part of the local amplification region of (e).

To examine the possible phases, the X-ray diffraction pattern collected from the cross-sections of the gradient structure in the DLDED sample, as shown in Figure 3-2a, compared with patterns from that of as-received and water-quenched samples under a velocity of 1 degree/min

and a step of 0.02 degree. It can be easily observed that both the gradient structure (blue line) and the as-received sample (yellow line) indicate the evident presence of the peak of the β phase. However, there is no β phase peak detected by X-ray diffraction for water-quenched samples (green line). Hence, the identified β phase only exists in the gradient structure and as-received sample. Moreover, such an obvious diffraction peak of the β phase in the gradient structure also reveals the existence of the α phase because α and β phases usually appear together to form the common $\alpha+\beta$ structure in Ti-6Al-4V [55]. This structure is easily further confirmed by OM and SEM in the following analysis. The as-received sample with the known rolled $\alpha+\beta$ microstructure demonstrates this point due to the same strong β phase peak. For the water-quenched sample, we know the sample is cooled from 1100 °C to 400 °C within 0.01s. Therefore, the achieved cooling rate of 7000 °C/s indicates a fully martensitic structure (α') [46] without the detected β phase. Moreover, α' possibly exists in the DLDED sample because the existence of α' phase leads to a wider α/α' reflection [136] compared with the known $\alpha+\beta$ phases for the as-received sample. For this reason, the water-quenched sample with a pure martensitic structure presents the broadest α/α' reflection. Therefore, the gradient structure in DLDED Ti-6Al-4V is probably composed of $\alpha+\beta+\alpha'$.

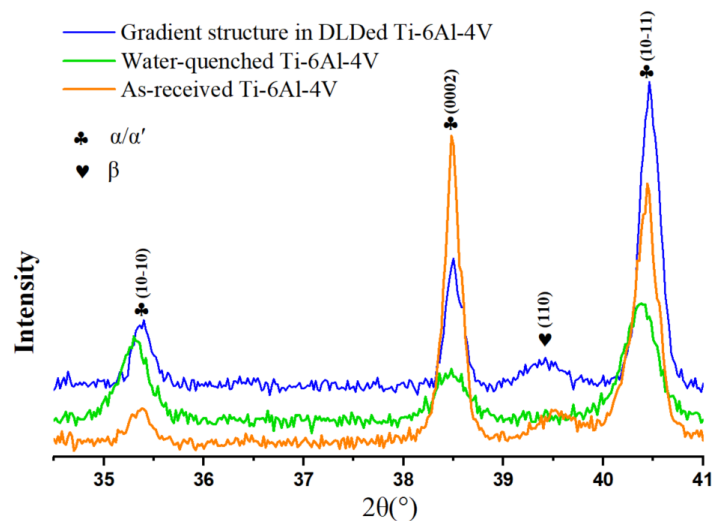


Figure 3-3: XRD patterns of the cross-section of three different samples. Blue, green and yellow lines corresponding to gradient structure in DLDED sample (blue rectangular box in Figure 3-2a), water-quenched sample by Gleeble (Figure 3-2e), and the as-received Ti-6Al-4V for Gleeble experiment (Figure 3-2d), separately.

To locate those possible phases mentioned above and analyze their features in gradient structure of DLDED sample, magnified OM and high-resolution SEM images (after etched) from each zone (Figure 3-2b) are shown in Figure 3-4 and Figure 3-5 separately. Obviously, the phase species and features are different from each other in different zones, especially the morphological change at prior β grain boundaries (GBs), which help identify the main phases corresponding to each zone. In detail, zone1, about 2.21mm with five deposited layers, is primarily composed of the typical $\alpha+\beta$ structure, including GB- α and lamellar $\alpha+\beta$, similar to the structure of Figure 3-5a [46]. This structure arises from a diffusion-controlled transformation by slow cooling and annealing [48]. The α phase prefers to nucleate at and grow along prior β GBs to form a continuous α layer (also called GB- α [137]), indicated by black arrows in Figure 3-4e and 4f. Note that the thickness of GB- α is observed to decrease along the Z direction (also observed by Tan et al. [122]), especially GB- α in zone2 nearly disappears, pointed by the black arrow in Figure 3-4e. Besides, the gradual variation of lamellar $\alpha+\beta$ structures is captured by SEM images in Figure 3-5f, e, and d. Fine lamellar $\alpha+\beta$ structures (details are shown in Figure 3-5g) are dominant in Figure 3-5d in the top section of zone1. The fine lamellar structures are all replaced by large lamellar structures in the bottom zone1 (Figure 3-5f), and the captured lamellar structures, as shown in Figure 3-5e, demonstrate the transitional process.

For zone2 about 5.4 mm with 11 layers, indicated by Figure 3-4c, 4d, 5b, and 5c, it can preliminarily postulate that α_m and needle-like α' phases without GB- α and α plates are inside prior β grains by comparing the similar OM image of Figure 3 [46]. Also, the α_m phase can be further confirmed and distinguished with the GB allotriomorphic α phase from two aspects through SEM images: (1) the location and (2) shape and size. First, the GB allotriomorphic α phases are distributed along prior β GBs [130][138]. On the contrary, α_m phases include both GB-crossing

and non-GB-crossing types, as stated by Lu et al. [59]. Herein, the circled α_m phases, as shown in Figure 3-5b and 5c, belong to the non-GB-crossing case because there is a lack of discovery of prior β GBs adjacent α_m phases. The isolated α_m phase is surrounded by martensite α' phases from SEM observations. For shape and size, the α_m phase is patch-shaped and about dozens of microns in size, similar to the discovered α_m by SEM [59]. It is different from the discovered GB allotriomorphic α phases, which are mostly shown as discontinuous side plates with a width below several microns [138]. All these analyses, combined with SEM images, further confirm the existence of the α_m phase in zone2.

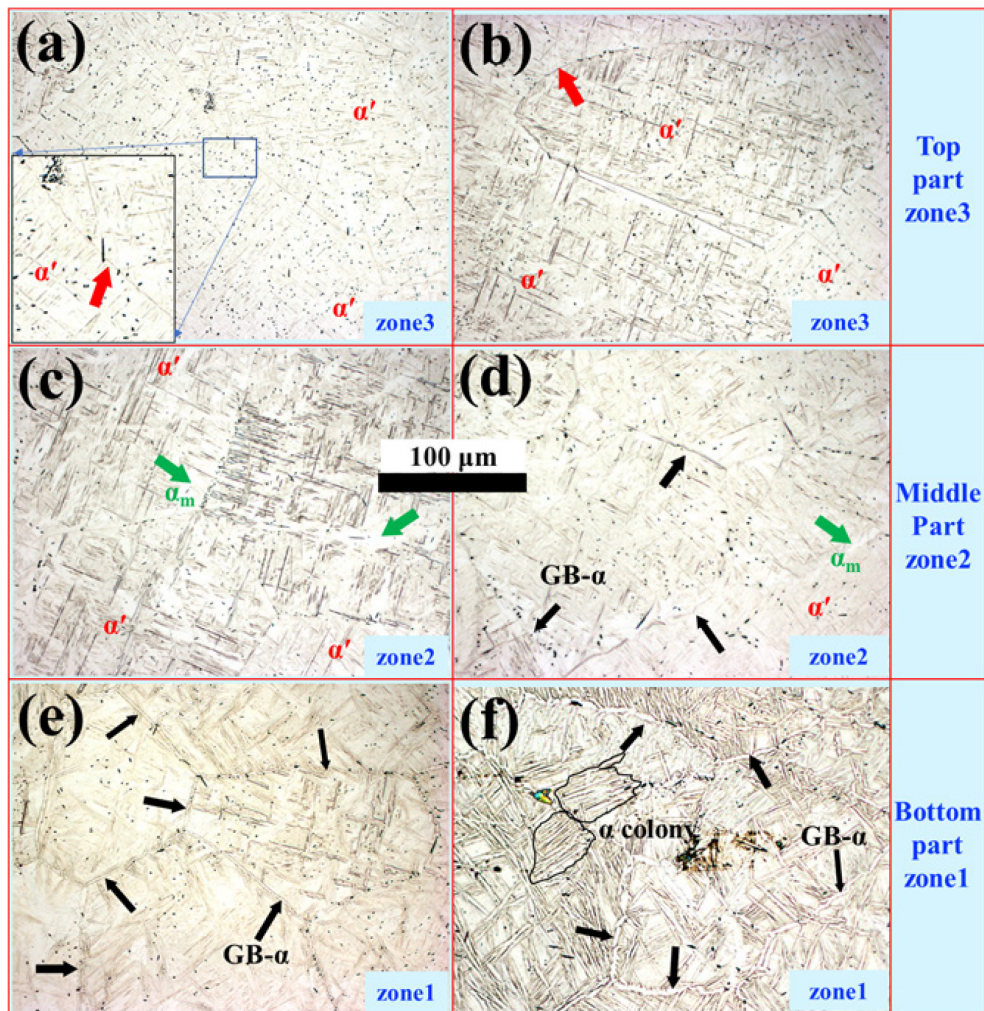


Figure 3-4: optical microscopy (OM) characterization of gradient structure in DLDED Ti-6Al-4V along building direction, i.e., (f)~(a): (a)(b) zone3, i.e., α' zone, (c)(d) zone2, i.e., $\alpha_m + \alpha'$ zone, and (e)(f) zone1, i.e., $\alpha + \beta$ zone. Black arrows indicate GB- α at the prior β grain boundaries, green arrows correspond to the α_m near prior β boundaries, and red arrows point to the sharp edge without GB- α and α_m at prior β boundaries.

zone3 is about 1.53 mm composed of three deposited layers. It is featured with a sharp prior β GBs (marked by red arrows in Figure 3-4a and 4b) and the martensite needles [139] inside the prior β grain. By observing the SEM image of Figure 3-5a, the largest α' phase pointed by the red arrow is called “primary α' ” across the entire parent β phase, and other finer α' phases are ordinarily parallel or perpendicular to the primary α' [51]. Therefore, zone3 is a pure martensitic structure full of α' phases similar to that of the water-quenched sample by Gleeble (Figure 3-2f) and Figure 3.2 [46].

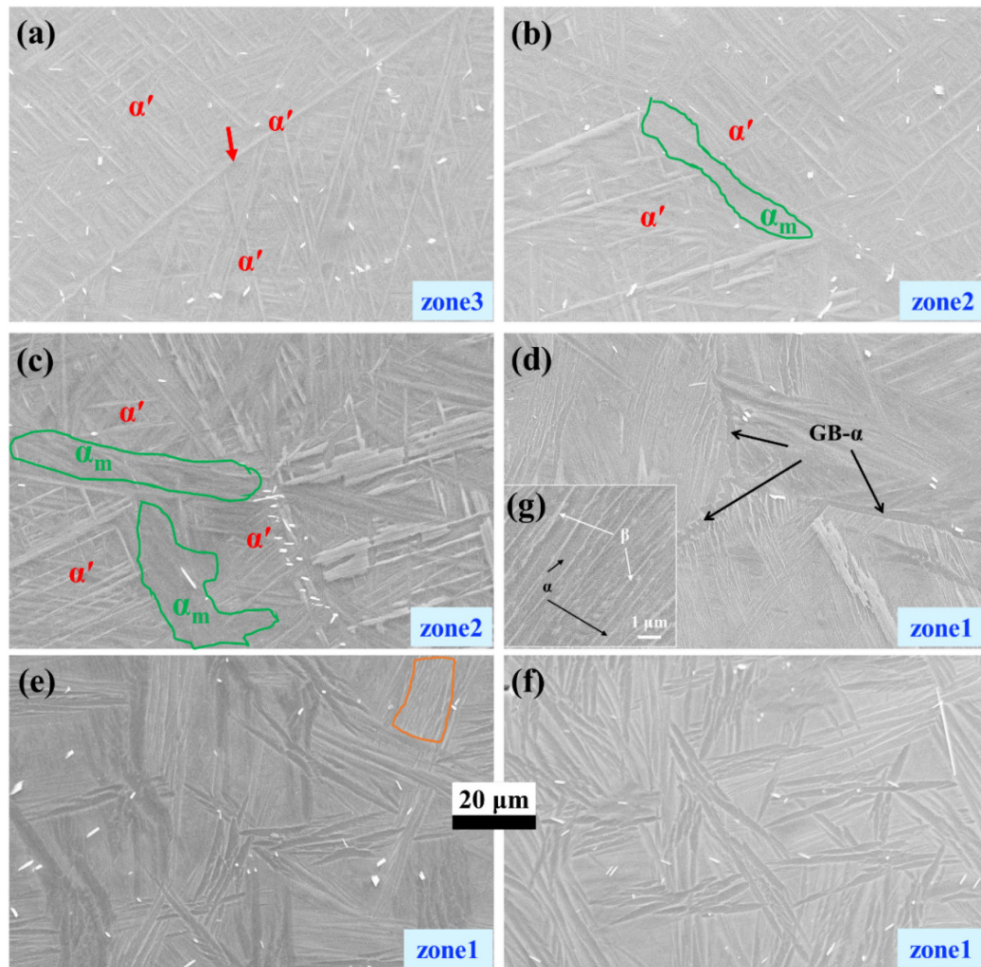


Figure 3-5: Scanning electron microscopy (SEM) characterization of gradient structure in DLDED Ti-6Al-4V along building direction, i.e., (f)~(a): (a) zone3, i.e., α' zone, (b)(c) zone2, i.e., $\alpha_m + \alpha'$ zone, and (d)(e)(f) zone1, i.e., $\alpha + \beta$ zone. (g) part of the local amplification region of (d).

In summary, a graded structure changing from the $\alpha + \beta$ zone, $\alpha_m + \alpha'$ zone to α' zone along the building direction on the top of the DLDED sample (about 10 mm height) is confirmed.

3.4.2 Vickers hardness testing

To further explore the graded properties, Vickers hardness tests are performed as a function of location along the Z or building direction for the DLDED sample, as shown in the left side of Figure 3-6, while the testing results of the water-quenched sample by Gleeble are shown on the right side. As can be seen, DLDED Ti-6Al-4V shows a continually increasing trend of microhardness along the building direction overall, but some fluctuations exist. Specifically, at the bottom of the sample, the hardness of a typical $\alpha+\beta$ lamellar structure in zone1 is about 340~355 HV, consistent with the testing results [140]. With the decreased size of α layers, the hardness verifies an increasing trend [141] for the $\alpha+\beta$ lamellar structure along the Z direction, which is consistent with the increased hardness along the Z direction in zone1. The hardness of the water-quenched sample by Gleeble is examined by about 390 HV, similar to the top zone of DLDED samples with a pure martensitic structure. Note that the hardness on the surface shows a decreased trend.

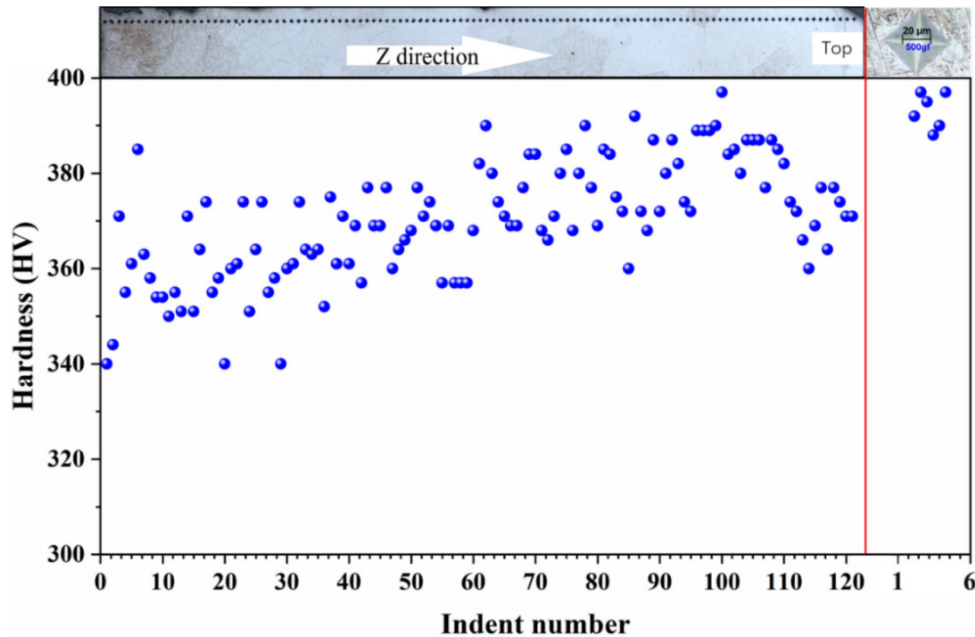


Figure 3-6: Micro-hardness profile measured along the building direction of gradient structure in DLDED Ti-4Al-6V (left side) and water-quenched Ti-4Al-6V by Gleeble (right side).

3.5 Discussion

3.5.1 The analyses of phase evolution

3.5.1.1 Phase transformation pathway of α' zone

Firstly, the chosen TCs of the L_M ($M=12$) layer (at the middle point of each layer) are plotted and verified with the experimental results, mainly including the peak temperature and the cooling rate of the melt pool. Specifically, the simulated peak temperature is about 2201.63 °C, which is coincided with the maximum temperature (~ 2100 to 2500 °C) measured by the IR camera [121]. Also, the simulated cooling rate (23748.23 °C/s) between the peak temperature and the melting temperature indicated by the yellow rectangle in Figure 3-7 is consistent with the experimentally measured value (~ 12200 to 38500 °C/s) with a layer thickness of 0.508 mm [121]. Note that the cooling rate used for studying phase evolution herein mainly refers to the dT/dt between the β transus point (T_{β}) and the martensite-start point (M_s) [118], as shown in the red rectangle in Figure 3-7. Here, TC_{M-N} is used to represent the N TC of the L_M layer, in which M and N count starting from the top layer and the first TC, respectively. Also, multiple TCs are produced because the laser beam repeatedly scans over the recording. Therefore, for example, L_{12} , as shown in Figure 3-7, corresponds to 12 TCs, i.e., TC_{12-1} , TC_{12-2} , TC_{12-3} (indicated in the purple rectangle) $\sim TC_{12-12}$. It should be noted that although the β transus is set as a condition herein that all phases completely transfer to β phase during heating, the temperature slightly below the β transus of 980 °C still can contribute to incomplete transformation to the β phase. More quantitative discussions can refer to [142] and are not involved in this paper.

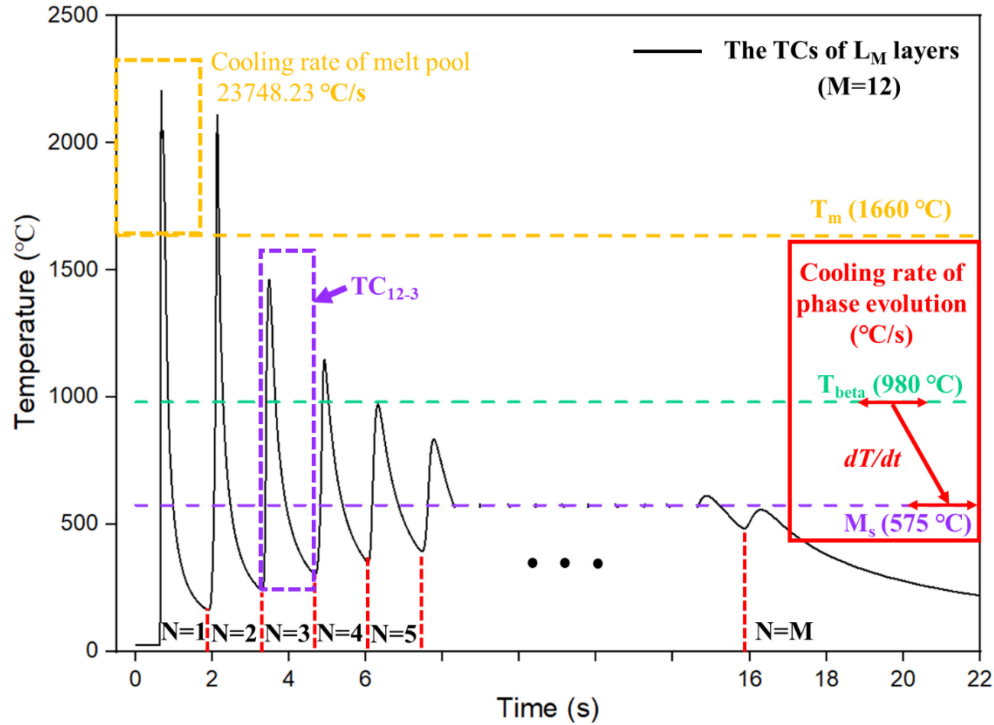


Figure 3-7: The computational TCs, i.e., TC12-1~ TC12-12 of LM (M=12): The cooling rate of the melt pool and phase evolution are shown in red rectangular and yellow rectangular, separately. The purple rectangular indicates the TC12-3.

Prior to discussing the phase evolution, some criteria, shown in Table 3-3, should also be clarified. In detail, the following principles [118] are followed.

1. If the cooling rate is above 400 °C/s, the peak temperature is above T_{β} (980 °C) and the bottom temperature (the lowest temperature in each TC) is below M_s (575 °C), the diffusionless transformation of $\beta \rightarrow \alpha'$ mainly occurs [118].
2. If the cooling rate is between 25~400 °C/s, the peak temperature is above T_{β} , and the bottom temperature is below M_s , the diffusionless transformation of $\beta \rightarrow \alpha' + \alpha_m$ mainly occurs [118]. It should be noted that the transformations happen locally, i.e., $\beta \rightarrow \alpha'$ or $\beta \rightarrow \alpha_m$ occurs at different locations and is highly independent of each other.
3. If the cooling rate is above 25 °C/s and the peak temperature is below T_{β} , the metastable phases, i.e., α' and α_m , are mainly retained.
4. If the cooling rate is below 25 °C/s with the temperature between 400~800 °C, the

diffusion-controlled phase transformation of $\alpha'+\alpha_m \rightarrow \alpha+\beta$ [53][59] and the growth of α and β phases occur. Note that $\alpha' \rightarrow \alpha+\beta$ or $\alpha_m \rightarrow \alpha+\beta$ also happens locally.

Of course, the heating process possibly results in the slight decomposition of α' and α_m , which is not considered due to the short-time heating process (about 0.028~0.4s). Also, the liquid phase, formed above the melting point of 1660 °C, is not discussed in this paper. Besides, the diffusionless transformation already partially happened as long as the cooling rate is above 25 °C/s even when the bottom temperature is above M_s . Hence, the non-equilibrium transformation in Conditions 1 and 2 is still qualitatively considered herein.

Table 3-3 Phase evolution criteria.

| Condition number | Cooling Rate (°C/s) | Peak Temperature (°C) | Bottom temperature (°C) | Main Phase transformation |
|------------------|---------------------|-----------------------|-------------------------|---|
| 1 | >410 | > T_{β} | < M_s | $\beta \rightarrow \alpha'$ |
| 2 | 25~410 | > T_{β} | < M_s | $\beta \rightarrow \alpha'+\alpha_m$ |
| 3 | >25 | < T_{β} | any | retained α' and α_m |
| 4 | <25 | 400~800 | | $\alpha'+\alpha_m \rightarrow \alpha+\beta$ the growth of α and β |

Figure 3-8 presents the computed TCs at center points of the top 3 layers, namely, L_1 , L_2 , and L_3 , constituting the α' zone. For L_1 , which experiences only one TC, i.e., TC_{1-1} , the phase transformation of $\alpha+\beta \rightarrow \beta$ firstly happens when the laser and raw powders travel through the center of L_1 with the peaking temperature $> T_{\beta}$, followed by $\beta \rightarrow \alpha'$ phase transformation at the cooling rate of 412 °C/s that satisfies the condition 1 in Table 3-3. So, the whole phase evolution for L_1 is $\alpha+\beta \rightarrow \beta \rightarrow \alpha'$. For L_2 , TC_{2-1} (with the cooling rate of 460 °C/s) results in the same phase evolution of $\alpha+\beta \rightarrow \beta \rightarrow \alpha'$ as that of L_1 . However, TC_{2-2} heats the α' back to β while the laser beam travels over L_2 for the second time, followed by $\beta \rightarrow \alpha'$ transformation during the cooling process at the cooling rate of 412.4 °C/s corresponds to condition 1 again. Hence, the phase evolution for L_2 is

$\alpha+\beta\rightarrow\beta\rightarrow\alpha'\rightarrow\beta\rightarrow\alpha'$. For L₃, because one more TC (TC₃₋₂) leads to one more $\rightarrow\beta\rightarrow\alpha'$ transformation, L₃ goes through the phase evolution of $\alpha+\beta\rightarrow(\beta\rightarrow\alpha')_2\rightarrow\beta\rightarrow\alpha'$, where the subscript indicates the number of TCs. One should note that $\beta\rightarrow\alpha'+\alpha_m$ (condition 2) possibly happens in TC₃₋₃ because the cooling rate is just 409.7 °C/s, resulting in the martensitic zones with a little α_m (pointed by the red arrow in Figure 3-8b) at the intersection between α' zone and $\alpha'+\alpha_m$ zone. In summary, the phase evolution for L₁, L₂, and L₃ is $\alpha+\beta\rightarrow(\beta\rightarrow\alpha')_M$, where the subscript indicates the times of ($\beta\rightarrow\alpha'$) and $M\leq 3$. This kind of phase evolution is mainly credited to two factors, i.e., (1) peak temperature ($> T_{\beta}$), and (2) cooling rate (>410 °C/s).

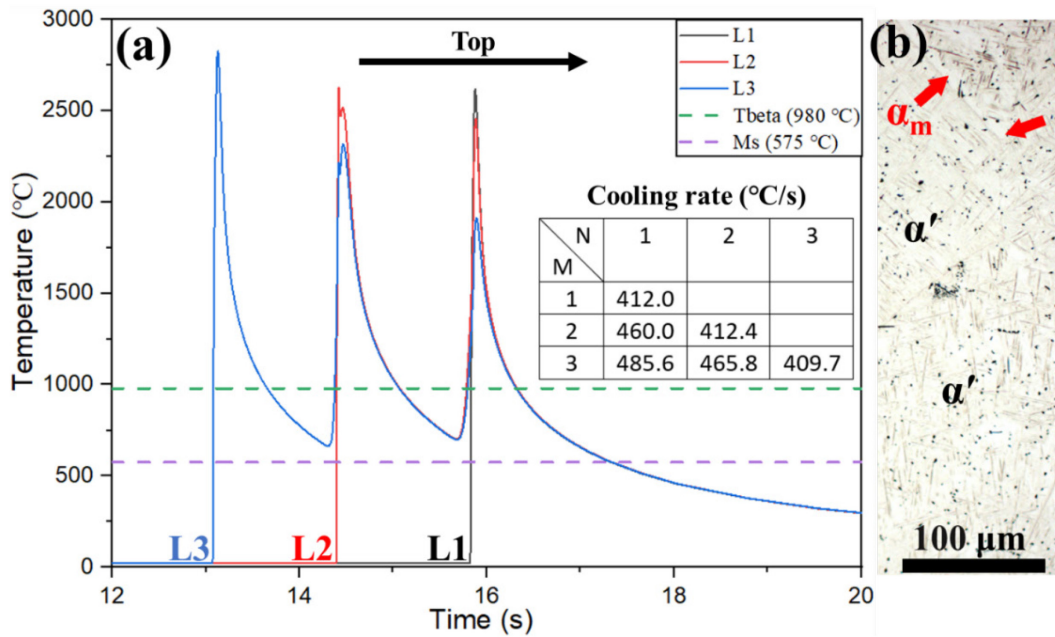


Figure 3-8: (a) The computed TCs at center points of the top 3 layers. (b) optical image of intersection between α' zone and $\alpha'+\alpha_m$ zone. M, and N corresponding to the number of layers and TCs, are numbered starting from the top layer and the first TC, respectively.

3.5.1.2 Phase transformation pathway of $\alpha'+\alpha_m$ zone

Figure 3-9a presents the chosen computed TCs at center points of L₄~L₁₂ layers, mainly constituting $\alpha'+\alpha_m$ zone (Figure 3-9b). Obviously, the peak temperature and the cooling rate both decrease with an increase of TC number N, thus leading to a further phase evolution according to the criterion listed in Table 3-3.

Specifically, for L₄ and L₆, two factors, namely, peak temperature ($> T_{\text{beta}}$) and cooling rate (>410 °C/s) are still satisfied by almost every TC beside the last TC (TC_{M-M}); hence the phase evolution is still $\alpha+\beta\rightarrow(\beta\rightarrow\alpha')_{M-1}$ when $N\leq M-1$, i.e., before the last TC. When $N=M$, the cooling rate for TC₄₋₄ and TC₆₋₆ reduces to 400, and 370 °C/s respectively but the peak temperature is still above T_{beta} , marked by red cycles, so the final phase transformation for last TC changes to $\beta\rightarrow\alpha'+\alpha_m$ (condition 2). The whole phase evolution develops into $\alpha+\beta\rightarrow(\beta\rightarrow\alpha')_{M-1}\rightarrow\beta\rightarrow\alpha'+\alpha_m$ ($M=4$ and 6). For the following layers ($M\geq 7$), the phase evolution of $\alpha+\beta\rightarrow(\beta\rightarrow\alpha')_{M-1}\rightarrow\beta\rightarrow\alpha'+\alpha_m$ occurs in normally when $N=6$ in this paper, indicated by green and blue cycles. When $N>6$, the cooling rate of TCs successively decreases to 25~410°C/s, and also the peak temperature decrease much to below T_{beta} . In that case, the condition 3 is satisfied, thus enabling the produced non-equilibrium phases, i.e., α' and α_m retained, which will be discussed in 5.2.1. Hence, the overall phase evolution for $\alpha'+\alpha_m$ becomes $\alpha+\beta\rightarrow(\beta\rightarrow\alpha')_{M-K-1}\rightarrow\beta\rightarrow\alpha'+\alpha_m\rightarrow(\alpha'+\alpha_m\rightarrow\alpha'+\alpha_m)_K$, where $M\geq 4$ and $K\geq 0$. Particularly, the slowest cooling rate at TC₁₂₋₁₂ is still about 30 °C/s, indicating the retained α' and α_m phases even at TC₁₂₋₁₂. Therefore, the $\beta\rightarrow\alpha'+\alpha_m$ transformation and retained α' and α_m lead to the formation of $\alpha'+\alpha_m$ zone due to the continuously decreased peak temperature ($< T_{\text{beta}}$) and cooling rate (25~410 °C/s).

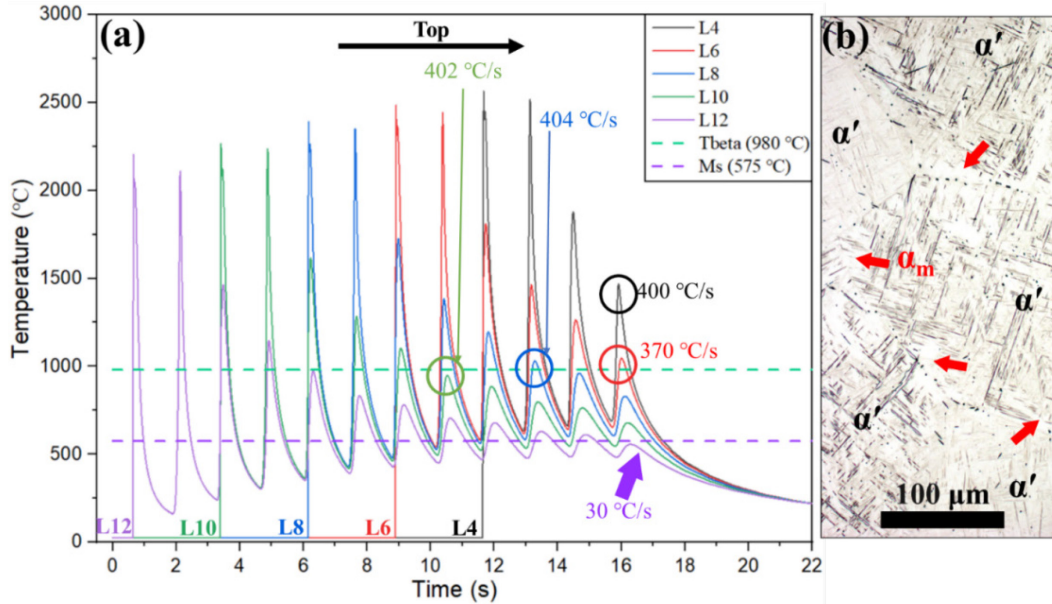


Figure 3-9: The computed TCs at center points of the next 9 layers (L4~L12). Monitoring locations for TCs are at the center point of each layer. The α_m phase is marked by red arrows.

3.5.1.3 Phase transformation pathway of $\alpha + \beta$ zone

The $\alpha + \beta$ zone, formed below the $\alpha' + \alpha_m$ zone, primarily comes from the decomposition of non-equilibrium phases α' and α_m that are the retained α' and α_m phases from the aforementioned evolution of $\rightarrow \alpha' + \alpha_m \rightarrow (\alpha' + \alpha_m) \rightarrow \alpha' + \alpha_m$. The formation of the $\alpha + \beta$ zone only when $M \geq 15$ means that the produced α' and α_m suffer further degraded TCs ($N \geq 15$) featured with two aspects, that is, (1) peak temperature (400 ~800 °C), and (2) cooling rate below 25 °C/s.

In terms of the deposition temperature (400 ~800 °C), Xu et al. have experimentally studied that martensitic structures (α') of AM-ed Ti-6Al-4V prefer to decompose between 400 ~800 °C [53]), leading to a fine lamellar $\alpha + \beta$ structure. Meanwhile, α_m can further transfer to the fine $\alpha + \beta$ structure [59]. Therefore, the discovered fine $\alpha + \beta$ structures (~1 μm), as shown in Figure 3-5d, 5e, and 5g, demonstrate the decomposition of all the metastable phase (α'/α_m), i.e., $\alpha' + \alpha_m \rightarrow \alpha + \beta$. On the other hand, the cooling rate has already reduced to 30 °C/s of TC₁₂₋₁₂, as shown in Figure 3-9. Based on the degraded trend [143], the cooling rate of below 25 °C/s is able to happen when $M \geq 15$, and thus, condition 4 is satisfied. Hence, the phase evolution becomes $\alpha + \beta \rightarrow (\beta \rightarrow \alpha')$

$M-K-2 \rightarrow \beta \rightarrow \alpha' + \alpha_m \rightarrow (\alpha' + \alpha_m) \rightarrow (\alpha' + \alpha_m)_K \rightarrow \alpha + \beta$. Considering the growth of the formed α and β phase with more TCs [48], the whole phase evolution becomes $\alpha + \beta \rightarrow (\beta \rightarrow \alpha')_{M-K-L-2} \rightarrow \beta \rightarrow \alpha' + \alpha_m \rightarrow (\alpha' + \alpha_m) \rightarrow (\alpha' + \alpha_m)_K \rightarrow \alpha + \beta \rightarrow (\alpha + \beta \rightarrow \alpha + \beta)_L$, in which $L (\geq 0)$ represents the limited number of TCs used for phase growth of α and β phases. The whole location phase evolution for all zones is summarized as Figure 3-10.

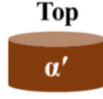
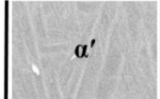
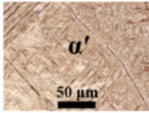
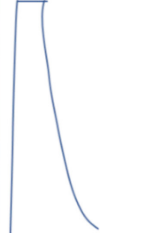

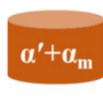
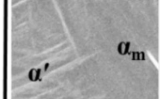

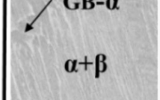

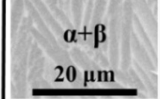
| Continuous TCs (DLD) | | | One TC (Gleeble) |
|---|---|--|--|
|  Top α' |  α' | $\alpha + \beta \rightarrow (\beta \rightarrow \alpha')_M$ |  α' 50 μm $\alpha + \beta \rightarrow \beta \rightarrow \alpha'$   α' |
|  $\alpha' + \alpha_m$ |  α' α_m | $\alpha + \beta \rightarrow (\beta \rightarrow \alpha')_{M-K-1} \rightarrow \beta \rightarrow \alpha' + \alpha_m \rightarrow (\alpha' + \alpha_m) \rightarrow (\alpha' + \alpha_m)_K$ | |
|  $\alpha + \beta$ |  GB- α $\alpha + \beta$ | $\alpha + \beta \rightarrow (\beta \rightarrow \alpha')_{M-K-2} \rightarrow \beta \rightarrow \alpha' + \alpha_m \rightarrow (\alpha' + \alpha_m) \rightarrow (\alpha' + \alpha_m)_K \rightarrow \alpha + \beta$ | |
|  $\alpha + \beta$ |  $\alpha + \beta$ 20 μm | $\alpha + \beta \rightarrow (\beta \rightarrow \alpha')_{M-K-L-2} \rightarrow \beta \rightarrow \alpha' + \alpha_m \rightarrow (\alpha' + \alpha_m) \rightarrow (\alpha' + \alpha_m)_K \rightarrow \alpha + \beta \rightarrow (\alpha + \beta \rightarrow \alpha + \beta)_L$ | |

Figure 3-10: Left side related to the phase evolution for each zone in the gradient structure of DLDed Ti-6Al-4V, i.e., α' , $\alpha' + \alpha_m$, $\alpha + \beta$ zones. M is the number of layers, K and L indicate the times of TCs used for (transformation). Right side corresponding to Gleeble-quenched counterpart.

It is also worth noting that some transformations possibly partially happen and are complete after several TCs. For example, one TC may not support a full transformation of $\alpha' + \alpha_m \rightarrow \alpha + \beta$ due to the very fast heat and cooling process in one second. Meanwhile, some quantitative details may need further updated models [144], and strict verifications, especially the verification of the phase transformation process is hard due to the transient transformation process and the difficulty of monitoring temperature during AM. Hence, the following sections provide two referable methods further to study some involved phase evolutions during AM of Ti-6Al-4V.

3.5.2 Phase evolution of α_m and α'

3.5.2.1 Gleeble designed experiments

Two phase evolutions involving α_m and α' phases are demonstrated here by specifically designed experiments using Gleeble-treated samples, including (1) α_m and α' phases are obtained from the β phase, and (2) α_m and α' can be retained after TCs. For the first one, the air-quenched sample by Gleeble is cooled at a rate of 30 °C/s according to the data acquisition system. The obtained sample is shown in Figure 3-11a, in which α_m is observed near GBs [59], as pointed by red arrows. A similar transformation has been reported [46], which concluded that the cooling rate between 25 and 410 °C/s could lead to a mixed structure of α_m and α' . The cooling rate of this range does not support the formation of GB allotriomorphic α [130]. This observation thus demonstrates the phase transformation in $\alpha_m+\alpha'$ zone2, shown in Figure 3-4c, d, and Figure 3-5b, and c.

To verify the second phase evolution, i.e., α_m and α' retained after TCs using TCs-treated samples. The IQ (Image Quality) maps obtained after each quenching process in one, three, and four TCs, are shown in Figure 3-11b, c, and d, respectively. After the first quenching process, the α' phase with untransformed α [132], shown in Figure 3-11b is obtained. However, after three and four TCs, the structure is composed of the α' phase and the patch-shaped α_m phase that is distributed near the GBs [59][46] (pointed by red arrows in Figure 3-11c and d) without any untransformed α . Although the performed TCs by Gleeble is not identical to the TCs of DLD, it still verifies three things: (1) suitable TCs can induce the formation of α' and α_m , (2) multiply TCs can lead to a fully α_m and α' structure, and (3) non-equilibrium phases, i.e., α' and α_m can be retained after multiply TCs.

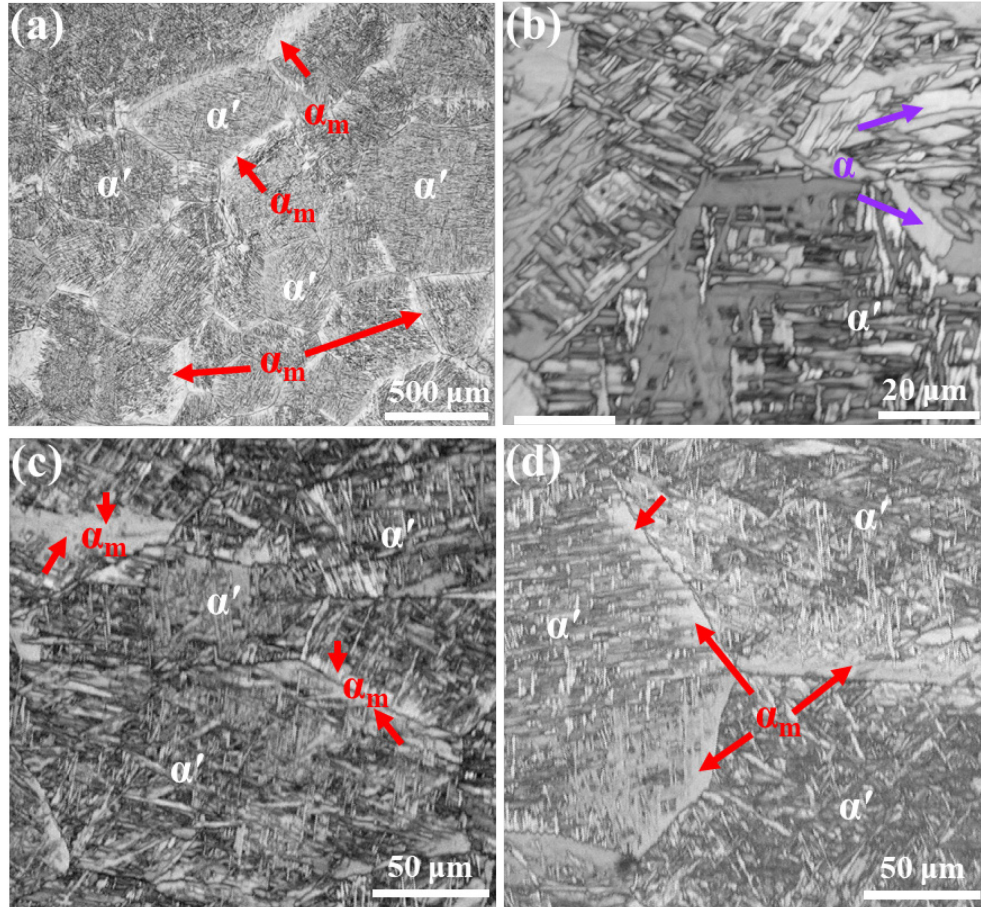


Figure 3-11 The microstructural profiles: (a) the OM image of the etched sample with a cooling rate of 30 °C/s; (b), (c) and (d) corresponding to the IQ (Image Quality) maps of the as-received sample got after quenching process in one, three and four TCs, individually. Red arrows point to the α_m phase.

3.5.2.2 Thermodynamic analysis

The thermodynamic approach is an effective way to analyze possible phase transformations [145][146]; here, the molar Gibbs free energy of HCP (α' , α_m , and α) and BCC (β) phases are compared to estimate phase transformations and study the kinetic pathways considering the cooling rate. The molar Gibbs free energies of HCP and BCC phases of Ti-6Al-4V, as a function of temperature and the atomic fraction of Al and V, are directly taken from the thermodynamic database [145].

$$\begin{aligned}
G^\varphi &= x_{Al} \cdot G_{Al}^\varphi + x_{Ti} \cdot G_{Ti}^\varphi + x_V \cdot G_V^\varphi + RT(x_{Al} \ln x_{Al} + x_{Ti} \ln x_{Ti} + x_V \ln x_V) \\
&+ x_{Al} \cdot x_{Ti} \sum_0^n L_{Al-Ti}^{\varphi,l} (x_{Al} - x_{Ti}) + x_{Ti} \cdot x_V \sum_0^n L_{Ti-V}^{\varphi,l} (x_{Ti} - x_V) \\
&+ x_{Al} \cdot x_V \sum_0^n L_{Al-V}^{\varphi,l} (x_{Al} - x_V) + x_{Al} \cdot x_{Ti} \cdot x_V \sum_0^n L_{Al-Ti-V}^{\varphi,o}
\end{aligned} \tag{3-4}$$

where φ represents either the α or the β phase. More details about a similar method are adopted by Xiao et al. [147].

The massive transformation (to form α_m) is characterized by composition-invariance and interface-controlled kinetics [148], the Gibbs free energy of β (the blue line) and α_m (the purple line in Figure 3-12) are calculated with the same atomic fraction of $(X(Al), X(V)) = (0.1019, 0.036)$ that corresponds to 6wt.% Al and 4wt.%V. Another high-temperature HCP structure (α') from martensitic transformation is also a typical diffusionless structure without any compositional variation. The main difference for these two transformations is that martensitic transformation is achieved by a cooperative movement of atoms (slip or twinning), while the massive reaction occurs by nucleation and short-range diffusional jumps across the massive/matrix interface [149]. Hence the Gibbs energy of α' should be similar to α_m , and thus α' can transfer to α_m thermodynamically with each other in an isothermal condition. Also, the high-temperature β phase has a higher Gibbs free energy than that of all HCP phases below a critical temperature of $T_c = 976$ °C that, close to T_{β} . When the temperature is higher than T_c , all the HCP phases tend to transfer to the β phase with a lower Gibbs energy. But solidification is a fast process in DLD, and the rapid cooling rate was also considered to provide a significant driving force for nucleation and phase transformation during cooling [145]. Hence, the Gibbs free energy of HCP structures should be lower (the red line in Figure 3-12), and thus the α_m and α' are more easily formed compared with the isothermal counterparts. In terms of the thermodynamic difference between α' and α_m phase, the α' structure

has higher energy than the α_m product because of the high mismatch and dislocations in the lath, while the α_m product is mainly at GBs and the mismatch can be partially relaxed near grain boundaries, as shown in Figure 3-11a, c, and d. Hence, when considering the contributions of the driving force by cooling rate and even the compositional variations with a decreased temperature, the α' phase might transfer to α_m (for more details [145]).

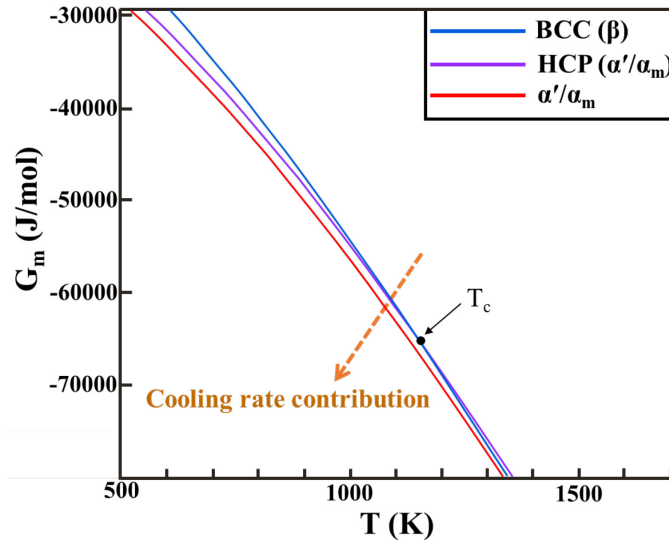


Figure 3-12: The Gibbs free energy changes as a function of temperature with different phases.

3.6 Chapter conclusions

In this paper, a Gleeble-assisted method was adopted to help study the possible phase evolution during AM of Ti-6Al-4V combined with the graded structure obtained on the top of DEDed Ti-6Al-4V cylinders. The graded structure of about 10 mm consists of the $\alpha+\beta$ zone (2.21 mm), $\alpha'+\alpha_m$ zone (5.4mm) to α' zone (1.53mm) along the building direction. The hardness tests show an increasing trend from about 340 to 390 HV. The location-dependent TCs arising from continually depositing new layers during AM are emphasized, and it is the main factor that contributes to the formation of this graded structure. Based on the graded structure, the phase evolutions, including $\beta \rightarrow \alpha'$, $\beta \rightarrow \alpha'+\alpha_m$, $\alpha'+\alpha_m \rightarrow \alpha+\beta$, and the growth of α and β phases are plotted as a function of the height along AM building direction. Particularly, α' and α_m

transformation and retention under TCs are verified by the Gleeble-designed experiments, and the possibility of various phase transformations is proved by a thermodynamic method. These research methods provide practical ways to study microstructural and phase changes under complicated thermal or physical environments. Also, the explored mechanisms of phase evolution are applicable to the large and practical AM-ed parts, thus providing insights into engineering phase structures of practical components.

Chapter 4: Quantitative simulations of grain nucleation and growth at additively manufactured bimetallic interfaces of SS316L and IN625

4.1 Introduction

4.1.1 Background

For the second question, the physics of fluid convection in the melt pools would possibly change the grain microstructures, especially at the interface of bimetals. During AM bimetals, the melt liquid flows would essentially change compositional distribution and generate a different mixing zone that different from two-parent materials, which, however, does not work during the single metal AM due to identical composition distribution everywhere in the melt pools. So, how does the potential flow-driven compositional distribution affect the grain structures at the bimetal interface require a deep understanding.

To experimentally investigate the flow convections, flow tracers and high-energy synchrotron micro-radiography techniques have been adopted [150][151]. Aucott et al. have pointed out that surface tension effects are considered a dominant driving force for melt pool flow, which is highly sensitive to specific elements like sulfur (S), enabling a flow pattern reversion [151]. Other driving forces, such as the Marangoni effect, vaporization, hydraulic pressure, buoyance force for melt flow, have also been analyzed [152]. Among them, the buoyance force and the Marangoni effect account for liquid convection from low-density zone to high-density zone and from high-temperature zone to low-temperature zone, respectively. Zhao et al. have reported that the fluid flow may lead to increased interface velocity (R) and suppress epitaxial growth during printing Co-Cr-Mo alloy [153]. These studies suggest that different

materials/compositions would cause different liquid flow behaviors and likely further affect the solidified microstructure evolution. However, most of the as-mentioned modifications and studies are limited to the AM-ed single/homogeneous material, and few works have studied the effect of fluid convection in the melt pool on the solidification behaviors during AM of bimaterial structures.

The complex physics of the mass and heat transfer in the melt pool, caused by the fluid convection at the bimaterial interface, likely results in distinctive solidification behaviors against the AM-ed single material. Recently, Chen et al. have built bimetallic structures of SS316L and IN625 by DED. The experimental observations indicate that different deposition sequences lead to completely different resultant microstructures (columnar/mixed grains) at the interface; the analysis has suggested it is related to flow behaviors, composition redistribution, and liquidus temperature [154]. However, most studies of bimetallic structures focus on the crack formation [155] and [156]. The underlying mechanisms governing different microstructures in the melt pool are still not well uncovered, especially the nucleation and grain growth processes demanding further quantitative investigations. It is still a daunting challenge to experimentally decipher either the flow behavior-induced composition changes or the composition redistribution-driven microstructure evolution process during AM of dissimilar material structures, which necessities the adoption of computational simulations.

The phase-field method (PFM), as a practical simulation tool, has been increasingly applied to simulate microstructural evolution during AM process. This is due to its unique advantage in accurately describing the diffuse interface without the need to explicitly track the moving interface [157]. Lu et al. have developed a PFM to investigate the solidified microstructures for AM-ed Ti-6Al-4V [100]. Keller et al. have simulated and studied micro-segregation for AM-ed IN625 by integrating the finite element method with the CALPHAD method [158]. The PFM has been used

to successfully simulate microstructure evolution during the layer-by-layer AM process and investigate site-specific microstructures [20] and particle coalescence [42]. In addition, the mechanisms governing the columnar to equiaxed transition (CET) of grain structures under different AM conditions have been thoroughly studied [24]. These studies show that PFM is capable of accomplishing simulations of the microstructural evolution of AM processes, including melting/remelting, nucleation, solidification, and grain growth. With the possibility of achieving coupling of complex temperature fields and liquidus temperatures, this simulation approach has the potential to achieve an effective in-situ investigation of the DED process of bimetallic structures, which are currently not achievable experimentally.

In this study, multi-physics modeling, mainly including a phase-field model and CFD, was developed to gain insights into the nucleation and grain growth process of DED bimetallic structures through two cases. Case1 is the deposition of IN625 on SS316L, denoted as IN625/SS316L, and Case2 is the deposition of SS316L on IN625, denoted as SS316L/IN625. How different flow behaviors affect the composition redistribution and the liquidus temperature for the two cases was examined first, followed by the analysis of the melt pool features of AM-ed bimetallic structures that differ from the AM-ed single material counterparts. Then, the temperature field and liquidus temperature information were fed to PFM for predicting the nucleation and grain growth process. Predictions of final grain morphologies were compared with experimental observations. Finally, the different microstructural evolutions for both cases, including nucleation and grain growth, were quantitatively analyzed.

4.2 The methodology framework

The developed framework, including multi-physics modeling and experimental validation, is shown in Figure 4-1a. The CFD model is employed to study the temperature field (I) and flow

behaviors (II) during the AM process. Then the flow patterns (II) are utilized as the input in the convection-diffusion simulation to verify the convection effects on compositional redistribution at the interface, i.e., mixing zone, as illustrated in Figure 4-1b. Meanwhile, the experimental examination by energy dispersive spectroscopy (EDS) is performed to validate the simulation results. Note that the mixing zone mainly refers to the specific region where the composition distribution is different from that of parent materials/bimaterial (about 60 μm along building direction [154]). In principle, the mixing zone is located at the interface, around which composition exchanges easily due to the presence of flow convection in the melt pool [159][160]. Three regions, i.e., two parent materials (presented as A and B) and the mixing zone at the interface can be observed in Figure 4-1b. Such a special configuration is thus called a sandwich structure herein. The liquidus temperature of this sandwich structure along building direction, as the input for PFM in Figure 4-1a, is obtained from a published paper [154], in which the values of parent material herein are 1623.0 K for IN625 and 1698.0 K for SS316L. CALPHAD method has been used to calculate the liquidus temperature of the middle mixing zone by using Thermo-Calc software and the thermodynamic database (TCFE8 steel/Fe-alloy), allowing for liquidus prediction of the location with a known composition distribution and has been adopted [161][162]. Finally, the PFM result is validated by comparing the final simulated grain structures with electron back-scattered diffraction (EBSD) images. In brief, combined computational and experimental efforts are devoted herein for concretely revealing the mechanisms of nucleation and grain growth, as shown in Figure 4-1.

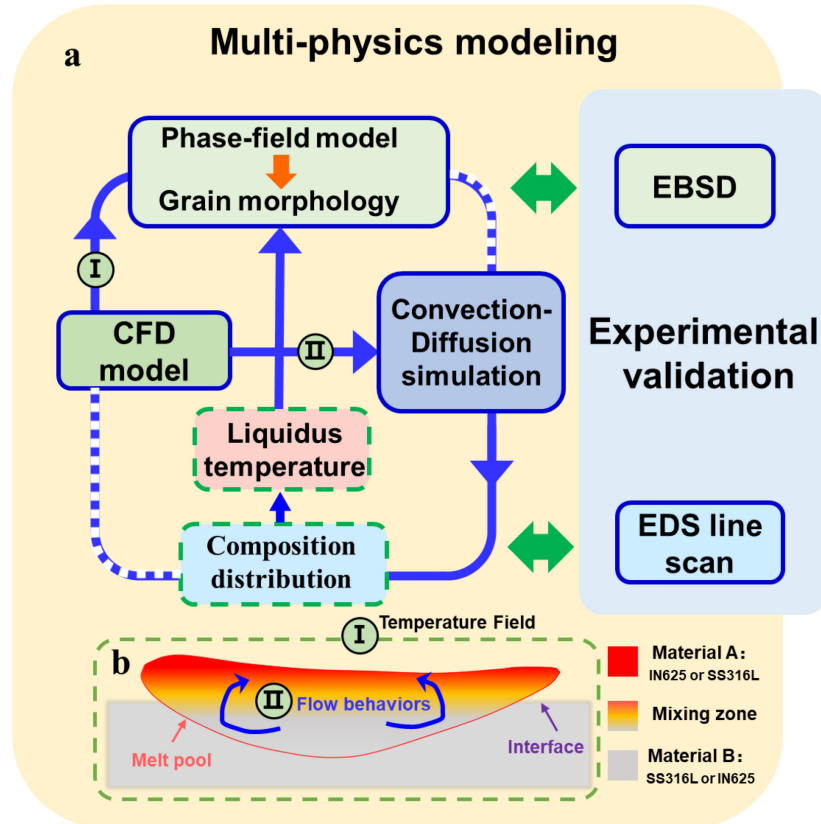


Figure 4-1: A workflow summarizes the framework combined multi-physics modeling and experimental methods to compressively carry out the study of nucleation and grain growth at the AM-ed bimetallic interfaces of SS316L and IN625. Subfigure (b) shows a sandwich structure of the melt pool considering the flow behaviors, where a mixing zone is at the interface. (I) and (II) from the CFD model indicate the temperature field and flow behaviors separately

4.3 Experimental methods

The Case1 (IN625/SS316L) and Case2 (SS316L/IN625) structures are additively manufactured by alternately depositing eight layers of SS316L and IN625 powders on the SS304L substrate using a high-power high-deposition system [154]. The commercial powders of SS316L (Sandvik, 45~150 μm in diameter) and IN625 (Carpenter Technology, 120~270 μm in diameter) are deposited with a flow rate of 20.5 g/min. Meanwhile, a 2KW laser beam (4 mm spot size) coaxially moves with a speed of 25 inches per minute. A simple line scanning pattern is adopted with a step-over of 2.5 mm. All the printing processes are done in an inert gas environment to avoid oxidation, and other process parameters can be referred to [154]. As shown in Figure 4-2, the printed sample with a part build volume of $110 \times 10 \times 65 \text{ mm}^3$ is located at the center of the

SS304L substrate. The obtained samples are then sectioned along with the ZY plan, indicated by yellow color in Figure 4-2. The following metallographic preparation is carried out by mounting the sectioned sample in epoxy and polishing it to 1 μ m diamond suspensions. Electrolytic etching and vibratory polish are applied to further improve surface finish for microstructural examinations. The metallographic samples include microstructures of Case1 and Case2. A scanning electron microscope (SEM) equipped with energy dispersive spectroscopy (EDS) is used to obtain the elemental composition across the bimetal interface. The EDS results are used to validate the predictions of the convection-diffusion simulation, as shown in Figure 4-1. Electron back-scattered diffraction (EBSD) analysis is performed to figure out microstructures used to corroborate PFM predictions. In addition, ImageJ software is used to analyze the size of different grains quantitatively.

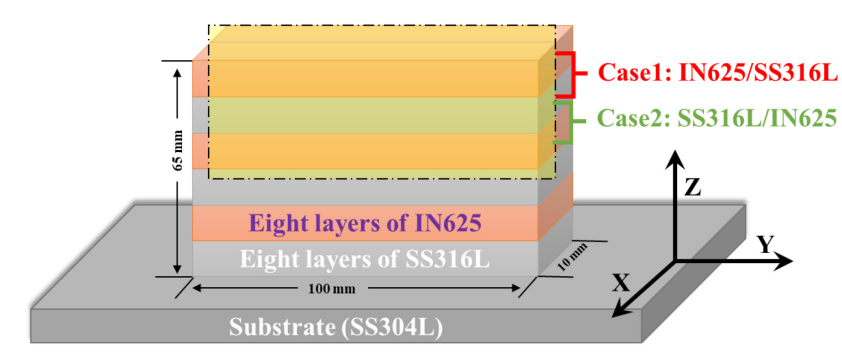


Figure 4-2: The schematic of AM-ed sample by directed energy deposition (DED) technique. Z is the building direction, Y is the scanning direction, and X is the step-over direction.

4.4 Computational methods

In this section, the two-layer single-track deposition is simulated for both cases. Specifically, the two cases are directly modeled by depositing IN625 on SS316L (Case1) or SS316L on IN625 (Case2) for simplification and computational efficiency while maintaining the physical understanding of underlying mechanisms. Note that the model can be easily extended to multi-layer depositions by iterative solutions.

4.4.1 Transient temperature field and flow behavior modeling

In this section, the two-layer single-track deposition is simulated for both cases. Specifically, the two cases are directly modeled by depositing IN625 on SS316L (Case1) or SS316L on IN625 (Case2) for simplification and computational efficiency while maintaining the physical understanding of underlying mechanisms. Note that the model can be easily extended to multi-layer depositions by iterative solutions.

Commercial CFD software, Flow 3D, as employed by Wang and Zou (2019)), is used to calculate the heat transfer and flow behaviors during depositing IN625 on SS316L (Case1) and SS316L on IN625 (Case2), which are investigated separately. The thermal-fluid dynamics process is modeled by simultaneously solving the mass, momentum, and energy conservation equations [163], which are listed in Eq. (4-1) through (4-3), respectively.

$$\frac{\partial \rho}{\partial t} + \nabla \cdot (\rho \mathbf{u}) = 0 \quad (4-1)$$

$$\frac{\partial}{\partial t} (\rho \mathbf{u}) + \nabla \cdot (\rho \mathbf{u} \otimes \mathbf{u}) = -\nabla \cdot p + \nabla \cdot (\mu \nabla \mathbf{u}) - S_m \quad (4-2)$$

$$\frac{\partial}{\partial t} (\rho H) + \nabla \cdot (\rho \mathbf{u} H) = \nabla \cdot (k \nabla T) - \rho \mathbf{u} \nabla H \quad (4-3)$$

where ρ is the fluid density, t is time, \mathbf{u} is the velocity vector, p is pressure, μ is dynamic viscosity, T is temperature, and k is thermal conductivity. S_m in Eq. (4-2) is the momentum source term driven by multiple forces (e.g., Marangoni force), and the ∇H in Eq. (4-3) is used to consider the latent heat caused by phase change (e.g., solid-liquid transition), detailed in [163].

Figure 4-3a presents the modeling geometry, whole boundary conditions, and mesh configurations. The dimensions, including the bottom rectangle-shape previous layers and top partial cylinder-shape deposited layer, are clearly indicated at the cross-section. The width and height of the deposition layer are consistent with the experimental observations. Note that such a

simplification using the partial cylinder as a deposited layer has been utilized in previous thermal-mechanical analysis [164][165], in which a general agreement in temperature field and melt pools were observed with and without this simplification. The good agreement between CFD-predicted melt pool shape and optical microscopy observations in previous research has demonstrated the effectiveness of this CFD model [154].

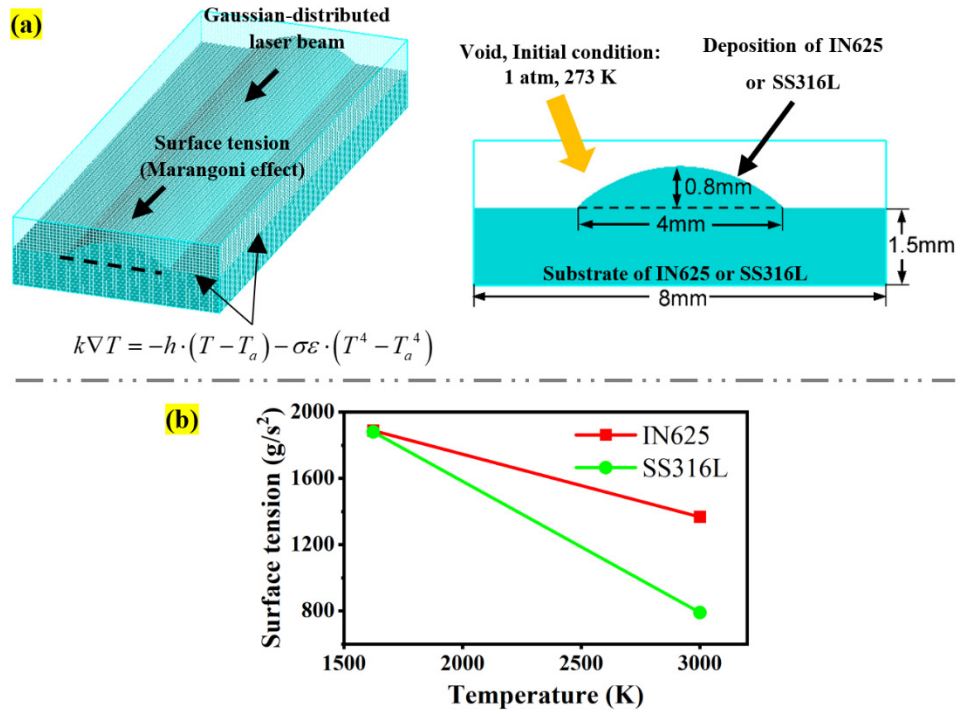


Figure 4-3: (a) Geometry model, whole boundary conditions, and mesh configurations for the CFD modeling, where h , ε , and σ are the heat convection coefficient, emissivity, and Stefan-Boltzmann constant, respectively. (b) The temperature-dependent surface tension of IN625 and SS316L.

The whole boundary conditions are shown in Figure 4-3a: including (1) thermal boundary conditions mainly includes Gaussian distributed-laser power density loading on the deposited layer surface, (2) heat loss by both the convective and radiative heat transfer through all surfaces that expose in inert gas, and (3) the surface tension shear stress is applied on the deposited layer surface using an implicit option in Flow 3D as the pressure boundary condition [166], which causes the temperature-driven Marangoni effect. The temperature-dependent surface tension of both SS316 and IN625 is demonstrated in Figure 4-3b. However, the composition-driven Marangoni effect is

not considered. Other temperature-dependent properties (i.e., thermal conductivity, density, and specific heat capacity) of the two materials can be referred to [154]. The initial condition is 273 K and 1 atm, as presented in Figure 4-3a.

The common volume-of-fluid (VOF) method is used to track the free surface boundary of two parent materials [159][166], as expressed by Eq. (4-4), in which F is fluid volume fraction, and \mathbf{u} is the velocity vector. $F=0$ indicates a void cell without liquid metal, and $F = 1$ indicates a liquid cell full of liquid metal. $0 < F < 1$ indicates an interface cell containing the void-fluid interface. The effect of the second phase on the VOF equation mainly comes from the inhomogeneous material and fluid properties, e.g., thermal conductivity, laser absorption rate, and fluid viscosity, which determine the fluid velocity by the governing equations (Eqs. (4-1), (4-2) and (4-3)) and thus affect the deformation of the free surface. The property of the mixture is the weighted average of the volume fraction of parent materials [167]. Note that herein the temperature field (I) and flow vectors (II) are got from the CFD model, as shown in Figure 4-1.

$$\frac{\partial F}{\partial t} + \nabla \cdot (F \cdot \mathbf{u}) = 0 \quad (4-4)$$

To further examine the flow effect on the element redistribution at the interface, a common convection-diffusion simulation is used to correlate the flow velocity field with the element concentration [168], which is described as,

$$\frac{\partial}{\partial t}(\rho C_i) + \nabla \cdot (\rho \mathbf{u} C_i) = \nabla \cdot (\rho D_i^m \nabla C_i) - S_i^c \quad (4-5)$$

where c_i is the concentration of element i , \mathbf{u} is the velocity field, and D_i^m is the multicomponent mixture-averaged diffusion coefficient, expressed as $D_i^m = (1-f_i) / (\sum_{k=i} \chi_k / D_{ik})$ [168]. The concentration source term S_i^c owing to phase change is set as zero here when ignoring the solute partition [169]. Further, based on elemental analyses by EDS and convection-diffusion

simulations, the liquidus temperature close to interface and its range can be calculated by CALPHAD method and finally act as one input for PFM, as shown in Figure 4-1.

4.4.2 3D solidification phase-field modeling

In this section, the two-layer single-track deposition is simulated for both cases. Specifically, the two cases are directly modeled by depositing IN625 on SS316L (Case1) or SS316L on IN625 (Case2) for simplification and computational efficiency while maintaining the physical understanding of underlying mechanisms. Note that the model can be easily extended to multi-layer depositions by iterative solutions.

The performed 3D PFM is developed based on previous studies [20][24], allowing for the simulation of microstructure evolution during the layer-by-layer AM process. As shown in Figure 4-1, this model is capable of incorporating the movement of the complex 3D temperature field indicated by (I). It also considers the flow behavior effects via liquidus temperature that is another input. During simulating AM process, a series of order parameters, i.e., $\Phi_q(r, t)$ ($q=1\sim Q$), are used to describe the structure of a polycrystalline simulation cell at a given time t at each position r within the simulation cell [170][171]. The continuous change of $\Phi_q(r, t)$ between 0 and 1 avoids the sharp change of interface and the explicit trace of grain boundaries [29]. The time-dependent Ginzburg-Landau equations (Eq. (4-6)) coupled with the total (Eq. (4-8)) and local (Eq. (4-9)) free energy equations are solved for the evolution of order parameters with time (t) and space (r), and the relative equations are given as follows.

$$\frac{\partial \phi_q(\mathbf{r}, t)}{\partial t} = -L_q(T) \frac{\delta F(t)}{\delta \phi_q(\mathbf{r}, t)} \quad (q = 1, 2, \dots, Q) \quad (4-6)$$

$$L_q(T) = L_0^* \cdot \left(\frac{T}{T_\alpha}\right)^m \cdot \exp\left(-\frac{\Delta E}{R_g T}\right) \quad (4-7)$$

$$F(t) = \int \left[w \cdot f_0(\phi_1(\mathbf{r}, t), \phi_2(\mathbf{r}, t), \dots, \phi_Q(\mathbf{r}, t)) + \sum_{q=1}^Q \frac{\kappa_q}{2} (\nabla \phi_q(\mathbf{r}, t))^2 \right] d\mathbf{r} \quad (4-8)$$

$$f_0(\{\phi_q(\mathbf{r}, t)\}) = -\frac{a}{2} \sum_{q=1}^Q \phi_q^2(\mathbf{r}, t) + \frac{b}{4} \left(\sum_{q=1}^Q \phi_q^2(\mathbf{r}, t) \right)^2 + \left(c - \frac{b}{2} \right) \sum_{q=1}^Q \sum_{s>q}^Q \phi_q^2(\mathbf{r}, t) \phi_s^2(\mathbf{r}, t) \quad (4-9)$$

In Eq. (4-6), the modified Arrhenius type equation of kinetic rate coefficient $L_q(T)$ is adopted to incorporate the effects of temperature and thermal gradient on grain boundary mobility [20][24], as expressed by Eq. (4-7). $\{\kappa_q\}$ are positive gradient energy coefficients related to the grain boundary energy, w is the barrier height. $f_0(\{\phi_q(\mathbf{r}, t)\})$ accounts for the local free energy density. a , b and c are constants with $a = b > 0$ and $c > b/2$. so that f_0 possesses $2Q$ degenerate minima. The polycrystalline grains are presented by those minima located at $(\phi_1, \phi_2, \dots, \phi_Q) = (\pm 1, 0, \dots, 0), (0, \pm 1, \dots, 0), \dots, (0, 0, \dots, \pm 1)$ [170]. Therefore, this phase-field model focuses more on grain growth evolution during AM process. In comparison with dendrite growth simulation, it brings a great advantage in effectively performing the simulation on a domain that is larger than several millimeters, allowing observing the simultaneous growth of grains in a moving melt pool. By contrast, the dendrite simulation is normally conducted with a relatively small scale ($\sim 100 \mu\text{m}$), normally limiting the simulation domain in one grain or several grains yet exponentially increasing computational cost. Considering the effects of flow behaviors on a melt pool-size scale, the grain growth model is suitably adopted herein, and the effects of flow behaviors on the grain evolution in a moving melt pool can be well studied. Solute partition and trapping are important phenomena in rapid solidification during AM (i.e., a non-equilibrium solidification process), yet more closely related to secondary dendrite arm growth [172][173]. The solute trapping can be manifested with a revised partition coefficient that is a function of solidification velocity/rate (R

as mentioned). Therefore, Solute trapping is implicitly considered by incorporating an R -dependent partition coefficient in calculating constitutional undercooling to be detailed below. Further, in order to predict the nucleation initiation, the nucleation undercooling is incorporated by using the common method [24] as follows.

Three different undercoolings, i.e., ΔT_t thermal undercooling, ΔT_r curvature undercooling, and ΔT_c constitutional undercooling, are summed to account for the total undercooling, ΔT , given as:

$$\Delta T = \Delta T_t + \Delta T_r + \Delta T_c = \frac{\Delta h_v}{c_p} I_v(P_t) + \frac{2\Gamma}{r} + mC_0(k_r - 1) \left[\frac{I_v(P_c)}{1 - (1 - k)I_v(P_c)} \right] \quad (4-10)$$

where Δh_v is the fusion enthalpy per unit volume, c_p is the specific heat, Γ represents the Gibbs-Thomson coefficient, the Ivantsov function $I_v(P) = P \exp(P) E(P)$, where $E(P) = \int_p^\infty \exp(-t)/tdt$. $P_c (= rR/2D)$ and $P_t (= rR/2h)$ are the solutal and thermal Peclet numbers, respectively, in which D is the solute diffusion coefficient in the liquid, h represents the thermal diffusivity of the melt, and r is the dendrite tip radius coupled with rapid thermal gradient [174]. m represents the liquidus slope, k_r is the revised partition coefficient obtained by mapping the k - R relationship [173]. The R ($\sim 0.1 \text{ m}\cdot\text{s}^{-1}$) is calculated using cooling rate and temperature gradient based on the temperature field got from CFD [31]. Then, the heterogeneous nucleation density against ΔT is characterized by a Gaussian distribution [175] as follows.

$$n(\Delta T) = \int_0^{\Delta T} \frac{dn}{dT'} d\Delta T' = \int_0^{\Delta T} \exp \left[-\frac{1}{2} \left(\frac{\Delta T' - \Delta T_N}{\Delta T_\sigma} \right)^2 \right] \frac{n_{max}}{\Delta T_\sigma \sqrt{2\pi}} \quad (4-11)$$

where ΔT_N and ΔT_σ are the mean undercooling, and standard deviation of undercooling, respectively, and n_{max} is the maximum density of nucleation sites. Then, the density of new grains $\delta n_v = \{n[\Delta T(t)] - n[\Delta T(t - \Delta t)]\}$ formed in each time step and effective volume $V_{ea} = dx^3$ are used to obtain the probability of nucleation at each lattice site P_v [168].

$$P_v = \delta n_v V_{ea} = \{n[\Delta T(t)] - n[\Delta T(t - \Delta t)]\} dx^3 \quad (4-12)$$

At each lattice site, once P_v is above the random number with 0 and 1 generated by the computer, a new nucleus forms in the melt pools. Other parameters used are listed in Table 4-1.

Note that the liquidus temperature of the mixing zone is included in Sec. 4.5.1.

Table 4-1: Physical parameters of the IN625 [154][158][176][177][178] and SS316L alloys [154] [179][180][181].

| Property (units) | Symbol | Values for IN625 | Values for SS316L |
|---|--------------|---|--|
| Liquidus temperature (K) | T_{Li} | 1623.0 | 1698.0 |
| Solidus temperature (K) | T_{So} | 1563.0 | 1673.0 |
| Specific heat | c_p | 40.07 (J·K ⁻¹ ·mol ⁻¹) | 4.85×10 ⁶ (J·K ⁻¹ ·m ⁻³) |
| Liquidus slope (K·(at%) ⁻¹) | m | -10.50 | -5.5 |
| Solute concentration of Ni in liquid (wt.%) | C_0 | 58 | 8 |
| Thermal diffusivity (m ² ·s ⁻¹) | h | 6.16×10 ⁻⁶ | 7.0 ×10 ⁻⁶ |
| Solute diffusion coefficient (m ² ·s ⁻¹) | D | 3.12×10 ⁻⁹ | 0.8×10 ⁻⁹ |
| Enthalpy of fusion | Δh_v | 2.04×10 ⁴ (J·mol ⁻¹) | 1.77×10 ⁹ (J·m ⁻¹) |
| Gibbs-Thomson coefficient (K·m) | Γ | 3.65×10 ⁻⁷ | 2.8×10 ⁻⁷ |

Figure 4-4 presents the coupled temperature field, geometry, boundary conditions, and initial conditions for FPM, where only the interface region (above ~0.8 mm and below ~1.45 mm) is modeled. In the model, two sets of parameters, i.e., the order parameters $\Phi(r_l, t)$ and the temperature field $T(r_l, t)$ are included to represent the grain structures and the tempo-spatial thermal distribution. For the initial condition, i.e., when $t=0$, $\Phi_q(r_l, 0) = 0$ for the deposited layer and $\Phi_q^2(r_l, 0) = 1$ for the previous layer indicating a polycrystalline structure before deposition. zero flux is applied on the top and bottom surfaces, and the periodic boundary conditions are applied on the surrounding surfaces. Temperature field $T(r_l, t)$ is obtained by mapping the temperature stored in the CFD model. The relative coordinates and the temperature of each coordinate remain unchanged; meanwhile, the absolute coordinates are changed to map and move the entire temperature field from CFD to FPM (T_F) [165][165]. Therefore, no initial thermal boundary is required.

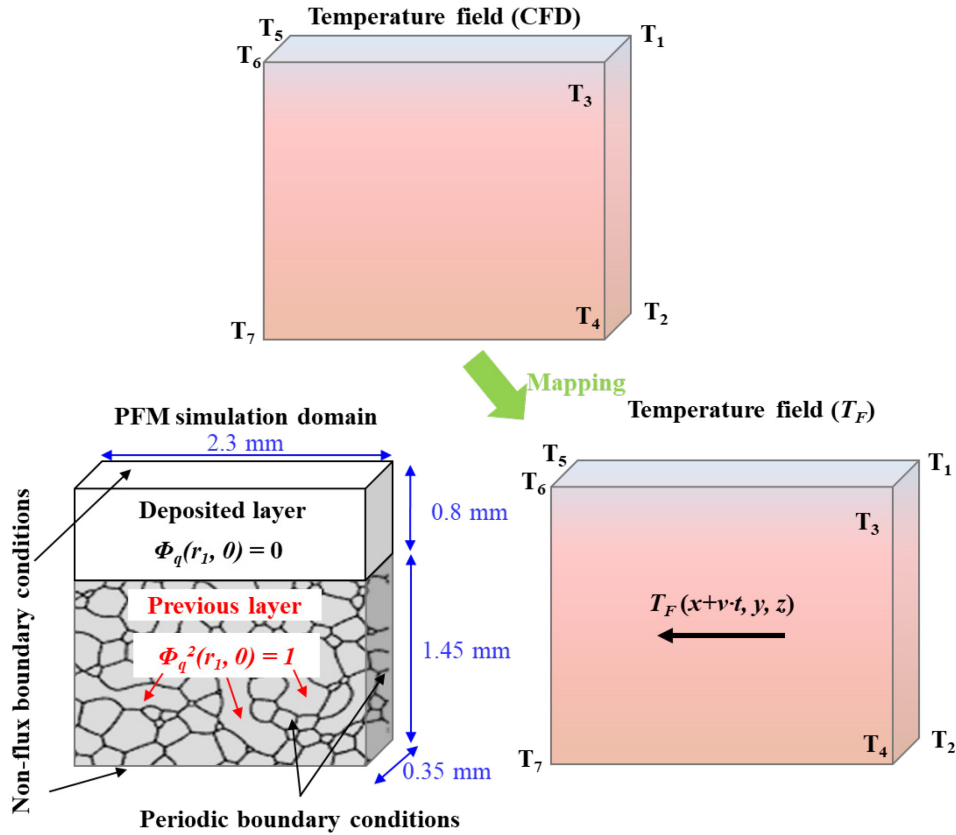


Figure 4-4: Schematic illustration of the grain growth model, including boundary conditions, dimensions, order parameters, and coupled temperature field.

4.5 Results and discussion

4.5.1 Flow behaviors, composition redistribution, and liquidus temperature

This section mainly aims to correlate the flow behaviors with the composition redistribution and then the liquidus temperature. Figure 4-5a and b compare the flow behaviors simulated by the CFD for both cases, i.e., IN625/SS316L (case 1) and SS316L/IN625 (case 2). Case1 mainly presents an expected clockwise flow field in the longitudinal section of the melt pool (see Figure 4-5a). This molten material flows from the back to the front of the melt pool and then rises up. While Case2 shows two distinct flow zones, i.e., one is at the front of the melt pool with a clockwise flow, and the other is at the rear of the melt pool with an anticlockwise (see Figure 4-5b). The front one has a similar flow pattern as Case1 yet at the front melt pool. The rear one

flows from the front to the rear and then to the up. The difference can be attributed to the thermo-physical properties mismatch-induced changes of surface tension, which is considered as the primary driving force for flow convection [151]. Specifically, the SS316L has a relatively higher laser absorption rate and larger thermal conductivity but lower viscosity than IN625.

Figure 4-5e and f present the variation of each element for both cases along the EDS scanning line, as indicated by the arrow lines in Figure 4-5a, c, and Figure 4-5b, d. Different zones can be distinguished by directly observing the compositional changes. Besides the zones with parent materials, i.e., SS316L (Z2) and IN625 (Z3), the remarkable transition zone (Z1) for both cases is identified by the turning point indicated by black circles. Case1 shows a continuous changing trend for the mixing zone (i.e., transition zone or Z1 in Case1) between Z2 and Z3, indicating a good implementation of blending by the clockwise flow convection. By contrast, there is one more zone in the mixing zone in Case2 featured with a composition abnormal-change (thus named as CACZ or Z4 herein); this zone breaks the continuous variation of composition in Case2. The mixing zone caused by flow behaviors for Case2 is thus composed of Z1 and Z4. This unusual Z4 demonstrates that the expected well-mixing (like Case1) is interrupted by the anticlockwise flow at the rear region of the melt pool (see Figure 4-5b), which counteract the effect of the front clockwise flow. The height of the mixing zone for both cases is about 60 μm at the interface, which implies the strong effect of flow behaviors.

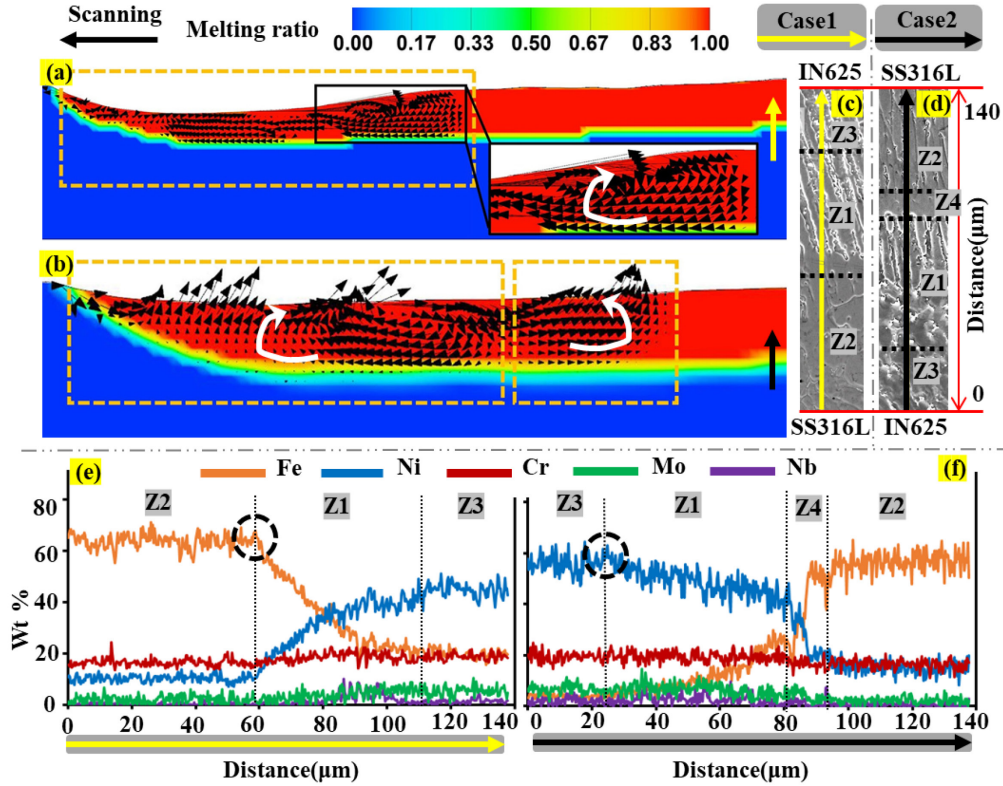


Figure 4-5: (a)(c)(e) Case1: IN625/SS316L, and (b)(d)(f) Case2: SS316L/ IN625. The flow field for (a) Case1 and (b) Case2. The position of composition tests by EDS line scanning in SEM images: (c) yellow arrow line for Case1 and (d) black arrow line for Case2, which are also indicated by the arrow line in (a) and (b). The EDS results for Case1 (e) and Case2 (f), in which Z1, Z2, Z3, and Z4 are transition zone, SS316L zone, IN625 zone, and composition abnormal-change zone (CACZ), separately. All the information is reorganized based on the reference [154].

Figure 4-6a and b show the simulation results from the convection-diffusion model given in Eq. (4-5) using the CFD flow velocity as the input. Obviously, the two cases show totally different composition distributions, which can be divided into different zones similar to EDS results, particularly the presence of CACZ in Case2. This is potentially attributed to distinctive flow behaviors between Case 1 and Case 2. Specifically, the clockwise flow in both cases with the negative vectors below 0.032 m/s at the beginning stage in the bottom melt pool leads to the transition zone (Z1). In addition to the clockwise flow, the anticlockwise flow for Case2 corresponding to a large positive flow vector up to 0.507 m/s sharply changes compositions at the upper melt pool, contributing to the formation of Z4. It is therefore concluded that the different

flow behaviors lead to the formation of different composition zones through the proposed simulation method.

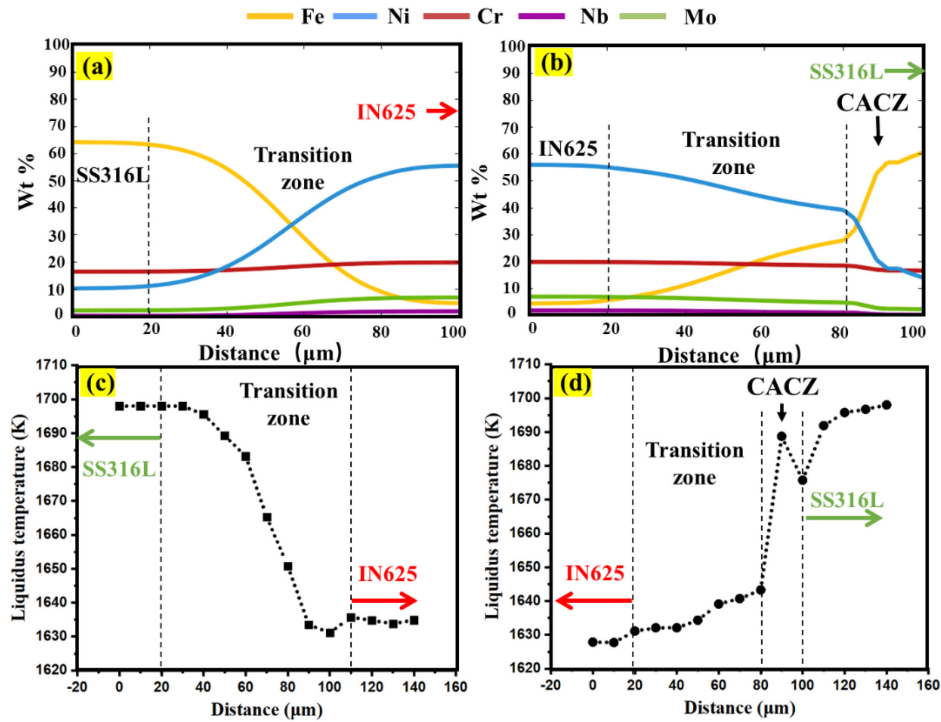


Figure 4-6: The simulated compositional distributions after incorporating the flow behavior for (a) Case1 and (b) Case2. The calculated liquidus temperatures for (a) Case1 and (b) Case2 are based on the CALPHAD method and elemental distribution along the EDS line [154].

Figure 4-6c and d present the liquidus temperature (T_L) for the mixing zone along the EDS scanning line (Figure 4-5c and d). The obtainment of T_L is based on the CALPHAD calculations [154]. Comparing Figure 4-6a with b, the two cases show different trends of liquidus temperature that follow the change of Fe element with a relatively high melting point. The liquidus temperature for Case1 shows a continuously decreasing trend yet with an opposite trend for Case2. Usually, the deposition sequence of dissimilar materials mainly determines the overall liquidus temperature trend for the mixing zone, i.e., from high melting point metal (SS316L) decreasing to relatively low melt point metal (IN625). It should be noted that the composition-abnormal change zone (CACZ) exists in the mixing zone of Case2, causing a relatively high liquidus temperature in this

localized region; by contrast, CACZ formation results from the anticlockwise flow, which is not seen in Case1.

The obtained liquidus temperature of the mixing zone is together with the liquidus temperature of IN625 and SS316L, forming the integrated liquidus temperature for both cases along the building direction. Here, this constructed liquidus temperature (T_L) will be extended along the Y direction (scanning direction) as one input for FPM, which will be used to determine the state (liquid or solid) for a given location in the simulation domain by comparison with the temperature field (T_F). Following this, the effects of composition redistribution (caused by flow behaviors) are considered and incorporated into the FPM further to uncover the microstructural evolution process (e.g., nucleation and grain growth) for both cases.

4.5.2 The temperature field and melt pool morphology

Figure 4-7c and d compare the temperature field (T_F) from the CFD simulations for Case1 and Case2, respectively. There is an apparent difference between the temperature field for the two cases. The main distinction is a larger high-temperature (> 1563 K) zone for Case2 compared to Case1. This is because the deposited layer of SS316L in Case2 enables absorption of more energy than the IN625 counterpart for Case1 due to the fact of laser absorption rate: 38~45% of SS316L $>$ 30~35% of IN625. It should be noted that the state of any position in the simulation domain can be determined by comparing the liquidus temperature (T_L) and temperature field (T_F). For example, once the temperature difference $\Delta T_{FL} (= T_F - T_L)$ is above zero at a given position, this position is liquid.

Figure 4-7a and b present the melt pool for Case1 and Case2, respectively. The melt pool is extracted from the temperature field and then colored according to the liquidus and solidus temperature contour lines of IN625 and SS316L used by [154]. Compared with the AM-ed single

material, it is evident that the melt pools of the AM-ed bimetallic structure are much more complicated. The most remarkable feature is a sandwich structure composed of outside bimetals and middle composition mixing zone, with each zone governed by different solidification rules due to different materials. Another difference is the irregular solid-liquid interface or the melt pool boundary, in contrast to a regular arc-curve interface and edge in the melt pool for the AM-ed single material. These sandwich structures and complicated shapes likely lead to a different solidification process compared with the AM-ed single material. Moreover, the various zones in these two melt pools show different distributions and morphologies, resulting in different solidification behaviors. For example, the melted zone of IN625 for Case2 is larger than that of SS316L for Case1, suggesting a larger remelting zone in Case2 than that in Case1. Therefore, the corresponding resultant microstructures and evolution processes are also different, as revealed in detail in Sec. 3.3.

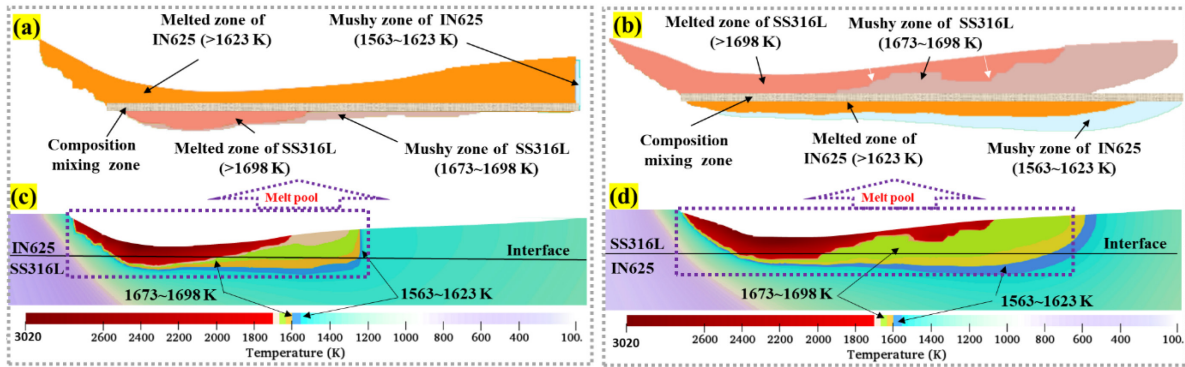


Figure 4-7: The temperature field for Case1 (c) and Case2 (d) based on CFD simulation [154]. The exacted melt pool from the temperature field for Case1 (a) and Case2 (b).

4.5.3 Mechanism of nucleation and grain growth

4.5.3.1 Final grain morphologies

Figure 4-8 shows the simulated and experimental [154] results for both cases. It can be seen that simulated and experimental grain morphologies for each case are consistent, yet two cases present different grain shapes and distributions. The columnar structure prevails in Case1;

in contrast, the deposition layer of Case2 shows two different grain morphologies along the building direction, i.e., (1) columnar grains at the interface and (2) equiaxed grains above the columnar grains.

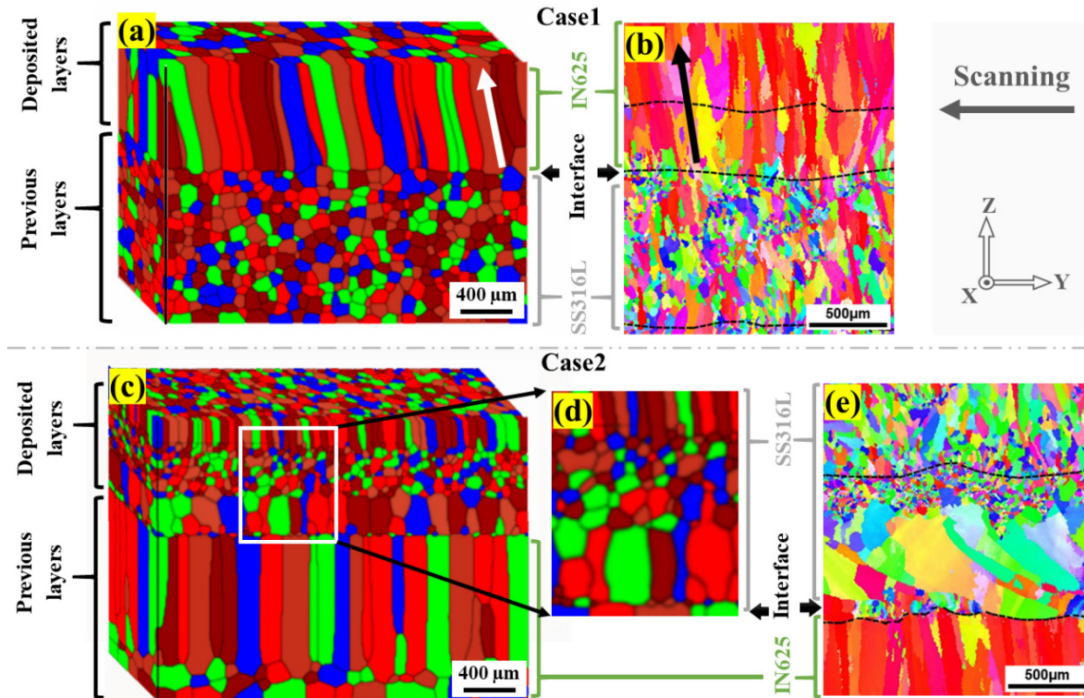


Figure 4-8: (a)(b) Case1: IN625/SS316L, and (c)(d)(e) Case2: SS316L/ IN625, where (a)(c) are PFM predictions, (d) is the enlarged view indicated by the white rectangular box indicated in (c), and (b)(e) are experimental EBSD images, performed by [154].

The comparisons of grain size and shape based on EBSD results and PFM predictions are quantified using ImageJ software and shown in Figure 4-9. For Case1, the main size of the simulated columnar grains is between 670~820 μm in length and 54~145 μm in width. Those columnar grains grow slightly inclined towards scanning direction about 8 degrees. These PFM simulated results exhibit a good consistency with EBSD observed grain size: 560~770 μm in length and 58~86 μm in width as well as 7~15 aspect ratio, see Figure 4-9a.

As shown in Figure 4-9b for Case2, PFM predicted columnar grains have a length of 285~327 μm and a width of 88~147 μm , which are also consistent with EBSD observations: 254~440 μm in length and 133~203 in width. In particular, both of the aspect ratios are between

1.4~3. As shown in Figure 4-9c, the size of equiaxed grains keep well consistent (34~60 μm) between EBSD results and PFM predictions. These show the effectiveness of the PFM model, and the process of nucleation and grain growth corresponding to two cases are further unveiled in the following two sections.

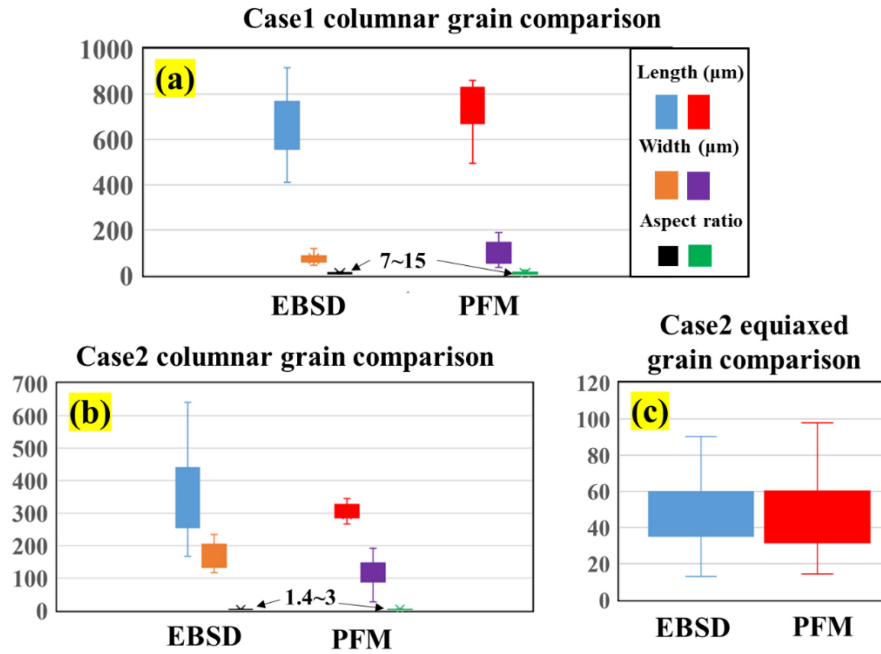


Figure 4-9: Box plots for grain comparisons between EBSD observations and PFM predictions.

4.5.3.2 The nucleation and grain growth at the interface of IN625/SS316L

This section mainly focuses on the nucleation and grain growth at the interface during depositing IN625 on SS316L (Case1). To illustrate the involved mechanisms, the real-time microstructure simulations and corresponding ΔT_{FL} map (the difference between temperature field and liquidus temperature) are performed and depicted, as shown in Figure 4-10. According to the solidification position and sequence, The DED process can be divided into three stages.

The stage1, as indicated in Figure 4-10a, is a melting process when the temperature field (T_F) is partially moving into the simulated domain. According to the ΔT_{FL} map, the red color indicates the liquid, including deposited IN625 and the partially remelted previous layer of SS316L,

forming an arc-shaped melt pool in the SS316L zone, which is consistent with the contour line of SS316L liquidus, as shown in Figure 4-7a. Note that the liquid state is the white color in the PFM domain. Considering the well-mixing zone caused by flow behaviors at the interface, the whole melt pool in stage1 is a liquid sandwich structure composed of liquid deposited IN625, a well-mixing zone in the middle, and partially remelt SS316L.

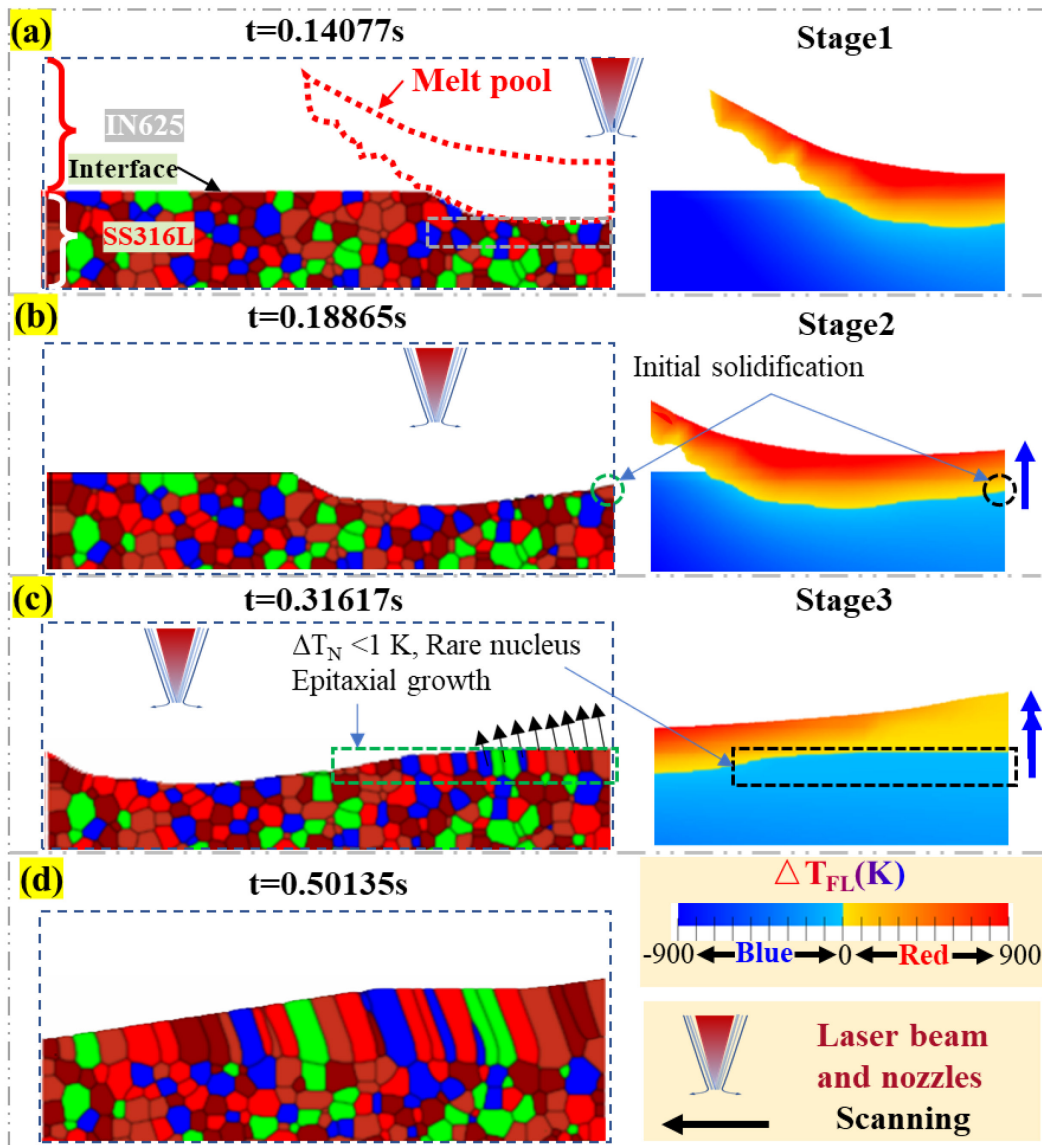


Figure 4-10: (a)~(d) present the simulated grain evolution process with time for Case1, i.e., depositing IN625 on SS316L, where the corresponding ΔT_{FL} map indicates the difference between temperature field (T_F) and liquidus temperature (T_L).

The stage2, shown in Figure 4-10b, is initial solidification. On the one hand, more parts of previous layers of SS316L are remelted with the continuous movement of the temperature field, as indicated by the larger red color zone in the ΔT_{FL} map penetrating the blue color zone compared with the stage1. On the other hand, the blue zone expands along the building direction (blue arrow) into the red zone at the rightmost simulated domain, indicating that the melt pool bottom tail initially evolves to the mushy zone like most AM-ed single materials [24]. This is mainly due to a high liquidus temperature (1698 K) of SS316L located at the bottom of the melt pool, where a relatively low-temperature field is shown in Figure 4-10b. Thus, initial solidification should occur in this mushy zone.

The stage3 is mainly involved in considerably epitaxial grain growth as the temperature field continuously moves forward, as presented in Figure 4-10c. Accompanied by the blue color region further replacing the red color zone along the building direction, epitaxial grain growth dominates in the expended blue color zone ($\sim 150 \mu\text{m}$ in length), indicated by black arrows. The tilt growth of grains is related to thermal gradient (G) [20]. The epitaxial growth is caused by the relatively small undercooling ($\Delta T_N < 1.0 \text{ K}$) of the IN625 zone (similar result for IN718 by Liu et al. [20]), which rarely triggers the heterogeneous nucleation and formation of new nuclei. Consequently, the apparent columnar grain formation prevails, as shown in Figure 4-10d, leading to columnar grain-dominated structure (Figure 4-8a and b), which is observed in other as-fabricated AM-ed IN625 [182][183][184].

To further verify the columnar growth mechanisms, rapid solidification conditions [31][185][186] are examined via the thermal gradient (G), the velocity or growth rate (R), and their ratio ε at the liquid/solid (L/S) interface. As shown in Figure 4-11, there are significant differences in G , R , and ε at the L/S interface since the L/S interface of the bimetallic structure is very complex

compared to that of AM-ed single metal. Compared with a printed single material [24], the change of G and R is not continuous and smooth along arc length due to a sandwich structured L/S liquidus temperature that is decided by SS316L, mixing zone, and IN625. Therefore, the ratio for different regions should be analyzed separately. The calculated ratio of G/R , which governs the solidification mode [185], for Case1 is shown in Figure 4-11b. The value of G/R for the bottom SS316L zone is larger than $10^7 \text{ K}\cdot\text{s}\cdot\text{mm}^{-2}$, leading to a high probability of forming columnar structures [185][187]. The IN625 zone (Z3) mainly shows a columnar growth trend with G/R ranging from 10^7 to $10^8 \text{ K}\cdot\text{s}\cdot\text{m}^{-2}$, indicative of a columnar growth [188]. As for the transition zone (Z1) with a much higher ratio than that of SS316L (Z2) and IN625 (Z3), columnar growth is also preferred. Overall, the melt pool for Case1 shows a preference for columnar growth like most AM-ed single materials.

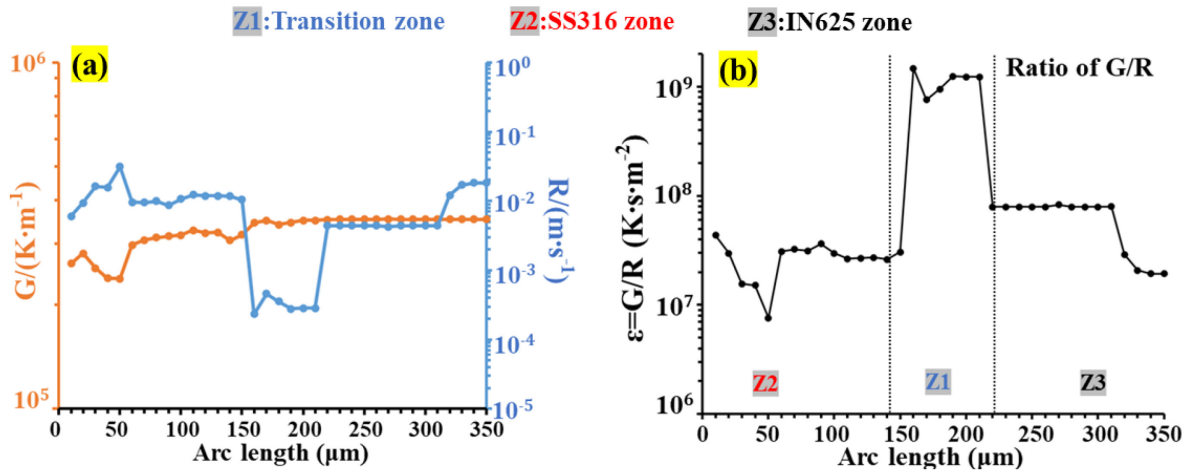


Figure 4-11: (a) shows the thermal gradient (G) and the velocity or growth rate (R) at solid-liquid (S/L) interface, and (b) presents the ratio of G/R for the S/L interface for Case1.

4.5.3.3 The nucleation and grain growth at the interface of SS316L/ IN625

Figure 4-12 presents the simulated grain structure and corresponding ΔT_{FL} map for Case2 as a function of time. It is clear that the evolution process significantly differs from that of Case1, i.e., columnar growth. In general, the as-fabricated AM-ed SS316L preferentially presents

columnar grain morphology [61][189][190][191]. However, in Case2, the common columnar structures are interrupted when depositing SS316L on IN625, as demonstrated by the experimental result in Figure 4-8e. This DED process is divided into four stages according to the solidification position and sequence.

The stage1 is similar to that of Case1, i.e., a melting process in the rightmost simulation domain, consistent with the red color zone in ΔT_{FL} map, as shown in Figure 4-12a. The liquid sandwich structure is different from that of Case1, and it is composed of top deposited SS316L, middle mixing zone, and bottom partially remelt IN625. Note that the remelt area is apparently deeper and larger than that of Case1 due to high energy absorption by top SS316L and the presence of IN625 at the bottom with a low melting point.

The stage2 is also about initial solidification, yet the position is different from that of Case1 and general AM-ed single material. As shown in Figure 4-12b of the ΔT_{FL} map, the red color zone expands along the moving direction, and a small red zone in the rightmost edge changes to blue color (indicated by green dash cycle) compared with stage1. Therefore, this changed zone initially becomes a mushy zone, followed by initial nucleation, as verified by simulated structure (indicated by dotted circles, $\sim 30 \mu\text{m}$). The nucleation begins in the middle place and just above the interface, corresponding to the suddenly changed composition zone (CACZ). This is because the CACZ has a high and comparable liquidus temperature as SS316L. Noteworthy is that complicated flow behaviors in Case2 drive the formation of CACZ.

The stage3 is shown in Figure 4-12c. As the temperature field continues to move forward, new nuclei ($\sim 30 \mu\text{m}$) are formed continuously forward at the CACZ height position. Meanwhile, the color of some sites at the left domain changes to blue in the ΔT_{FL} map, indicated by the rectangular box. This place belongs to the SS316L zone right above the CACZ, in which

significant nucleation undercooling ($\Delta T_N \sim 35$ K) would lead to abundant nuclei (25~45 μm). In this case, the nucleus in the bottom CACZ can only grow downward. Another common growing way is coalescence, and the new nucleus and small grains are likely merged to develop large grains [170].

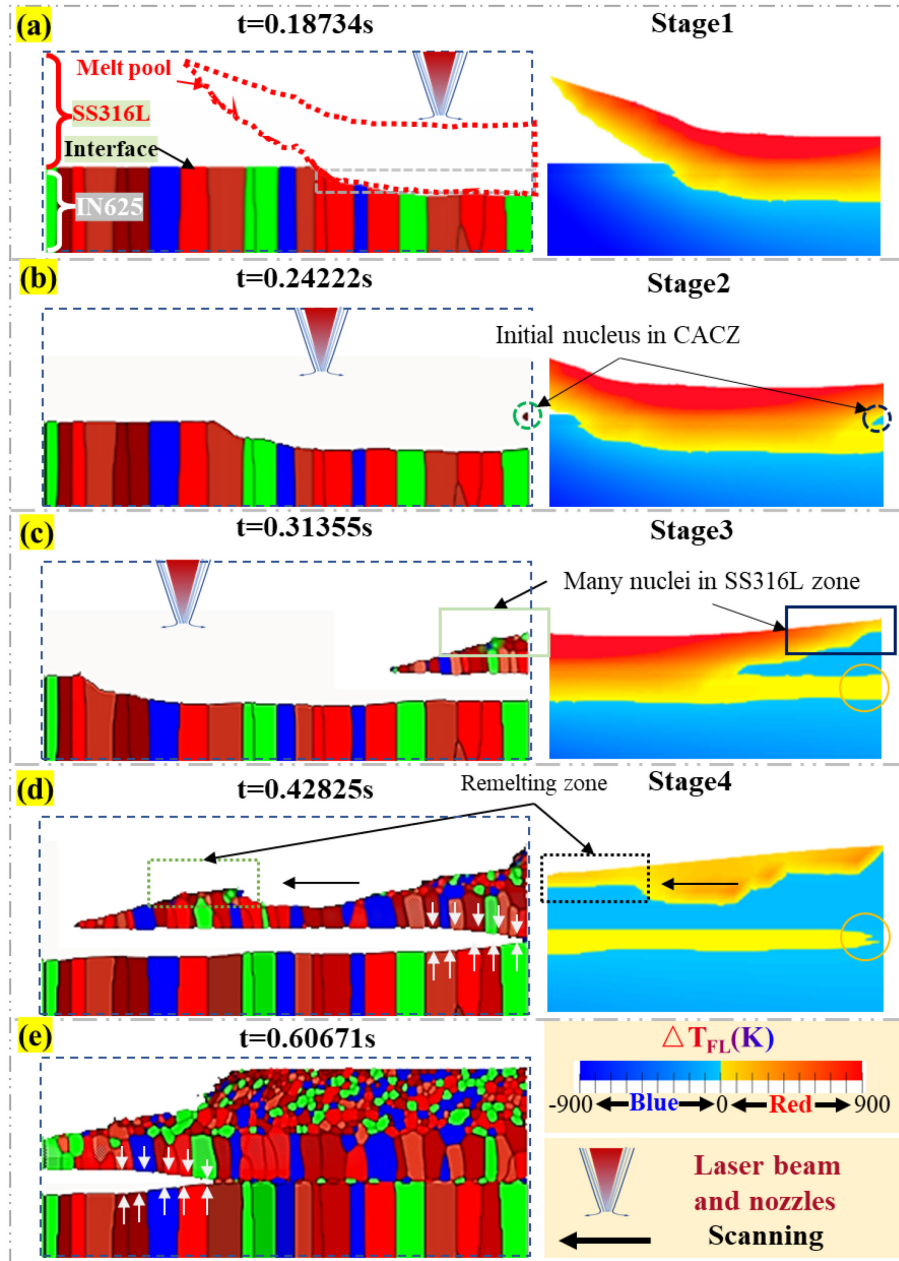


Figure 4-12: (a)~(e) present the simulated grain evolution process with time when SS613L depositing on IN625 (Case2), where the ΔT_{FL} indicates the difference between temperature field (T_F) and liquidus temperature (T_L) at the corresponding time.

The stage4 is mainly involved in the solidification of the bottom IN625 zone. By observing Figure 4-12d, the further expanded mushy zone starts to cover the IN625 zone because the red color of the zone indicated by the golden cycle in ΔT_{FL} map is partially substituted by blue color compared with that in stage3. Due to the calculated low undercooling ($\Delta T_N \sim 1.2$ K) and the low nucleation rate, existing grains beside IN625 would favor epitaxial growth. Meanwhile, many new grains constantly form at the SS316L zone. Note that remelting happens in the SS316L zone due to the zigzag-shaped S/L interface (indicated by the dotted rectangular box), in contrast with a smooth arc curve for most simulated melt pools [24][185]. As shown in Figure 4-12e, the top SS316L zone finally evolves to many small equiaxed grains due to the high undercooling. However, thanks to the limited space under the CACZ, the bottom CACZ grains can only continue to grow downward epitaxially to a length of 285~327 μm with a width of 88~147 μm in the end, as presented in Figure 4-8e. These grains have an aspect ratio of 1.4~3, thus regarded as short columnar grains herein. It should be noted that different ratio values are used to distinguish columnar and equiaxed grains, such as 3 used by Rafieazad et al [192].

Figure 4-13a presents the G , R , and their ratio for Case2. Compared with Case1, the first difference is that the L/S interface for Case2 (670 μm) is longer than that of Case1 (350 μm), which is evident by comparing the melt pool morphology in Figure 4-7a, and b. Second, the calculated values (i.e., G , R , and G/R) also differ from Case1. Here, the G/R is the main focus due to its close relationship with final grain structures. In the IN625 zone (Z3) of Case2, the relative high G/R ($8 \times 10^8 \sim 3 \times 10^9 \text{ K} \cdot \text{s} \cdot \text{m}^{-2}$) also leads to a propensity for epitaxial growth [188]. By contrast, the G/R of SS316L zone (Z2) in Case2 ($2 \times 10^6 \sim 10^7 \text{ K} \cdot \text{s} \cdot \text{m}^{-2}$) is lower than $10^7 \text{ K} \cdot \text{s} \cdot \text{mm}^{-2}$, which is considered to encourage the development of equiaxed grains [185][187][193]. As for the mixing zone, the CACZ zone (Z4) close to the SS316L zone (Z2) has a low ratio value, also leading to a

high nucleation rate, shown in stage1. The transition zone (Z1) shows a high ratio value like the IN625 zone (Z3), hence potentially preferring a low nucleation rate and epitaxial growth. Overall, the melt pool for Case2 shows different grain formation preferences for different zones with an unusual solidification sequence.

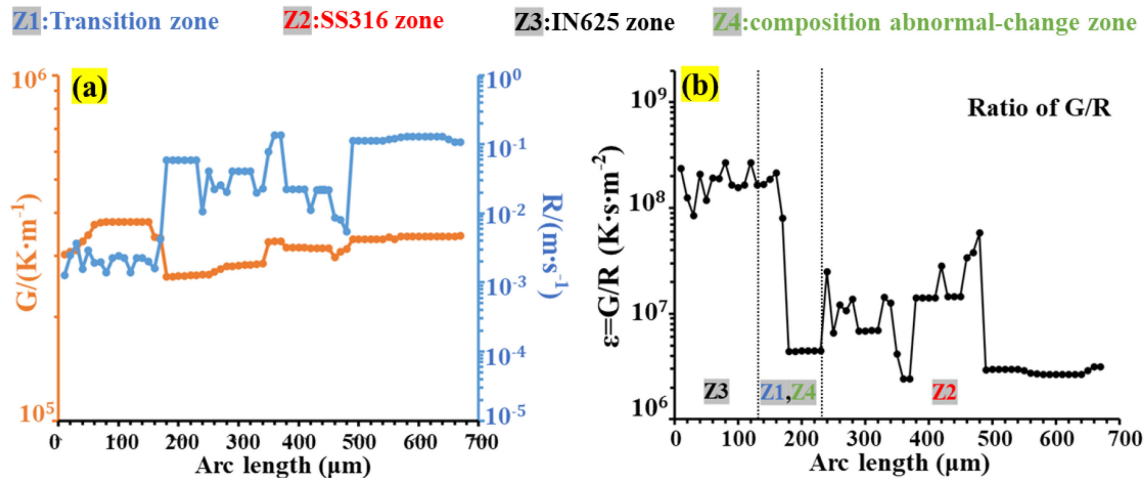


Figure 4-13: (a) shows the thermal gradient (G) and the velocity or growth rate (R) at the solid-liquid (S/L) interface, and (b) presents the ratio of G/R for the S/L interface for Case2.

4.6 Chapter conclusions

In this chapter, the nucleation and grain growth at the interface for DED-ed bimetallic structures (i.e., IN625/SS316L and SS316L/IN625) are simulated, and the main conclusions can be drawn as follows:

- Due to the high energy absorption rate of SS316L and low thermal conductivity of IN625, a deeper melt pool and longer solid-liquid interface are obtained of SS316L/IN625 than that of IN625/SS316L. Meanwhile, two opposite flows are present in the melt pool of SS316L/IN625, while the only clockwise flow is at the rear of the melt pool of IN625/SS316L.
- By incorporating the continuous liquidus temperature of SS316L/IN625 and non-continuous one of IN625/SS316L caused by different flow behaviors and compositional

redistribution into the phase-field model, grain morphologies for both cases are predicted and agreed with the EBSD observations quantitatively, which proves the effectiveness of the developed multi-physics modeling.

- IN625/SS316L mainly presents epitaxial grain growth based on SS316L substrate, leading to a general columnar structure similar to AM-ed single materials. By contrast, the initial solidification in SS316L/IN625 happens at the abrupt composition change zone in the middle melt pool arising from two opposite flows, accompanied by considerable nucleation due to the high undercooling (>30 K). Such a special solidification sequence leads to a mixed grain structure, i.e., columnar grains on the bottom and small equiaxed grains on the top.

This study would remind the potential effects of flow behaviors on nucleation and grain growth and likely give more insights into different microstructure formations for AM-ed bimaterial structures. In particular, the mixed grain structure in SS316L/IN625 has the potential to avoid the anisotropic properties that commonly exist with a columnar structure. However, for the accurate quantitative prediction of microstructural evolutions, the whole 3D temperature field and volume EDS scanning [194] is required and then incorporated into the 3D phase-field model in the future. Furthermore, due to the noise in experimental results and the complexity of physical phenomena like flow behaviors, the machine learning technique will be introduced to speed up the understanding and tailoring processing-structures-properties for AM-ed bimaterial structures in future work.

Chapter 5: Using machine learning to improve melt pool prediction in additive manufacturing: data denoising and predictive modeling

5.1 Introduction

5.1.1 Background

Question 3 raises a vital concern: How to create an inexpensive and rapid data-driven model that can effectively navigate the complex AM process-melt pool relationships, guiding both microstructure optimization and quality control? The primary objective, therefore, is to achieve precise melt pool prediction during the AM process using data-driven modeling.

The applications of data-driven modeling in the AM community have been reviewed in Section 2.4.3. Among these applications, data-driven predictive modeling of melt pool size has become an area of significant interest. The primary challenge associated with this is the careful selection, or even the design, of input features that can precisely capture the dynamic evolution of the melt pool. Existing melt pool modeling often builds upon simple AM process parameters like laser power and scanning speed, or includes material properties to expand the number of input features (up to 23 in total) [195]. Despite the enhancement, these simple input features overlook crucial physics that influence melt pool development, notably the evident thermal accumulation from adjacent scanning tracks or layers. Advanced models like the neighboring-effect modeling (NBEM) [196] and the L-NBEM model [197] have introduced innovative input features (i.e., time and distance neighboring-effect factors) to address this, outperforming general models (e.g., Power-Velocity Model and Energy Density Model). Other model has designed a so-called (pre-scan) initial temperature specifically to take into account the effect of thermal history on the melt

pool size [198]. However, these hand-designed input features rely strictly on domain experts and tend to lose the information of neighboring effects and other potential physics.

Integrating as much scientific knowledge as possible into designed inputs has been considered a promising way to improve data-driven modeling performance, striving to obtain more physics-strengthened correlations. Thus, various physics-related variables have been explored as inputs, such as energy density, surface tension force, Richardson number, and Marangoni number [90][199]. In this paper, various physical principles related to melt pool dynamics are considered, such as (1) laser on/off; (2) turning points; (3) strong heat dissipation at the boundaries, along with many inherent uncertainties in the AM process [2]. The complexity of these factors complicates melt pool dynamics and hinders sufficient physics-related variable design. In response, raw information of preceding laser spots (referred to as scanning history) is employed as input features, bringing two potential advantages. First, enormous raw information inputs would include the neighboring effect and also contain the uncertainty of inputs themselves and even other possible unknown physics. Second, the adoption of raw information would save time without requiring a repeated and complex calculation process of physics-related variables (resorting to physical models [90][199]) or hand-designed input features. Due to the complexity of the high-dimensional scanning history, machine learning (ML) techniques, specifically multi-layer perceptron (MLP), are implemented. The ML modeling with multi-layer perceptron (MLP) enables taking full advantage of unrivaled approximation capability and versatility in handling high-dimensional problems of neural networks (NN) even with many input features. Moreover, ML's self-adaptation [200] allows derivation of complex relationships, including thermal history and other influences, thus enhancing prediction performance. Therefore, this developed method takes full advantage of

the ML's ability to interpret as many factors, including physic effects, as possible from the scanning history that affects the melt pool dynamics.

However, experimental data are frequently subjected to noise interference due to the complexity of the physical environment, particularly due to the interaction between the laser beam and powders. This interaction initiates a series of complex physical phenomena such as convection, fluid flow, and radiation. As shown in Figure 5-1, during *in situ* capturing melt pools by using optical-based monitoring (e.g., high-speed cameras) [201], the plume and spatter are usually observed [85][202][203][204][205][206]. The formation of plumes originates from the ionization of metallic vapor [201], while the generation of spatters is widely attributed to the recoil pressure which propels some liquid droplets to escape the melt pool [201][202]. The contrast similarities between these physics-induced phenomena (plumes and spatters) and the melt pool pose a considerable challenge to the accurate extraction of melt pool morphology through standard thresholding operations [205][207]. Furthermore, manual interventions are impractical and labor-intensive when dealing with high-throughput experimental images. Despite the clear necessity, advanced and efficient denoising processes are yet to be incorporated in current experimental data-driven melt pool modeling strategies [196][197]. As such, the need for a sophisticated and efficient denoising process is crucial to ensure accurate melt pool extraction.

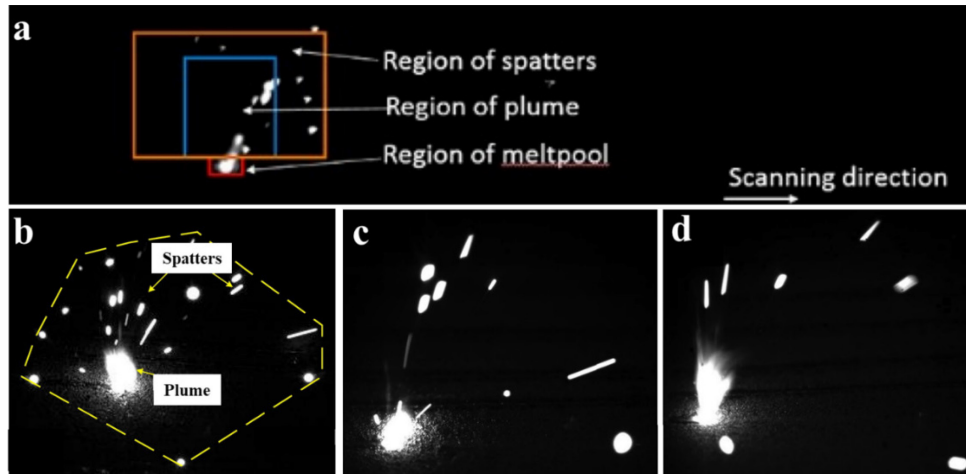


Figure 5-1: Typical examples for plume and spatter exposed under the high-speed camera with references (a) [85] (b) [204], and (c)(d) [202].

This study proposes an experimental data-driven melt pool predictive modeling framework, integrating experimental data denoising, scanning history inputs, and machine learning techniques. It aims to offer highly efficient and accurate melt pool area prediction performance compared to up-to-date experimental-data-driven models. The following sections introduce the extensive raw data, including melt pool images from the experiment conducted by NIST, and present a convolutional neural network (CNN)-based model designed to efficiently denoise melt pool images. Further, the data-driven melt pool predictive model based on artificial neural network (ANN) is trained, incorporating scanning history as input features, to derive more complex relationships between scanning history and melt pool areas. The trained ANN model's extrapolative prediction abilities are then evaluated, followed by a discussion on the necessity of the denoising process.

5.2 Experiment and Raw data

The National Institute of Standards and Technology (NIST), committed to creating standards and benchmarks for the Additive Manufacturing (AM) community, has developed the Additive Manufacturing Metrology Testbed (AMMT). This tool serves as a process image

acquisition device aimed at obtaining high-quality experimental data [111][197]. Utilizing the AMMT, the optical signal of the melt pool is retained and monitored through a coaxially aligned high-speed camera. The signal is then captured according to digital commands, as depicted in Figure 5-2a, which results in the creation of numerous melt pool images. Comprehensive details regarding the AMMT acquisition system can be found in references [111][197][208].

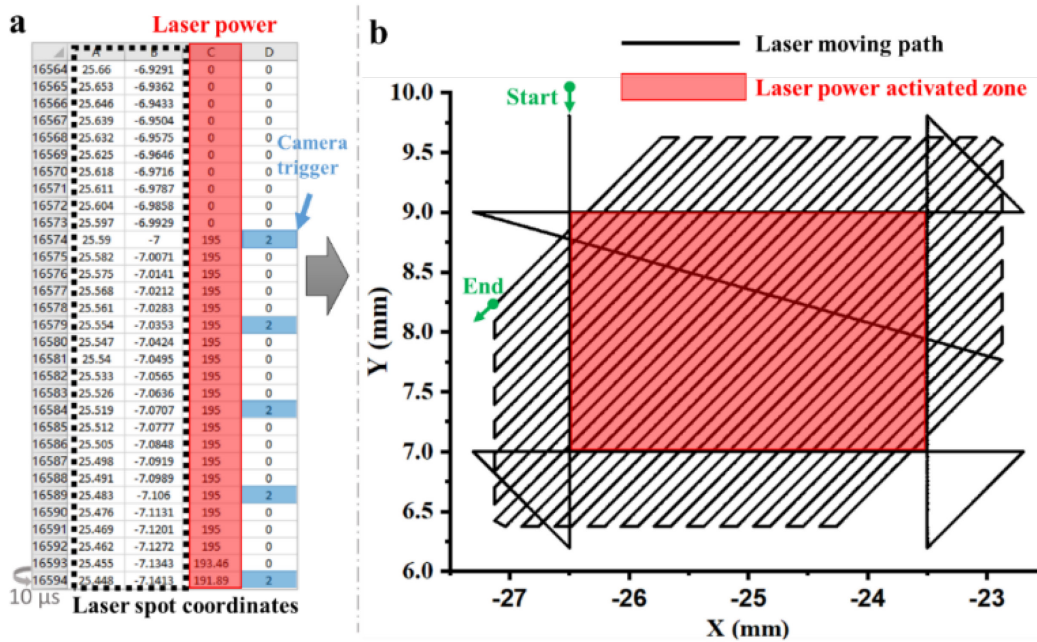


Figure 5-2: (a) Snapshot of AM commands, and (b) visualization of scanning path, including the laser-activated zone.

The raw data encompasses two main components: (1) digital commands and (2) melt pool images. As illustrated in Figure 5-2a, the former category includes information such as laser spot coordinates, corresponding laser power, and the camera's ON/OFF sequence (e.g., represented by 2/0 in the command). The visualization of the printing path and fabrication zone is constructed from these commands, as demonstrated in Figure 5-2b. The printing or scanning path follows a zigzag pattern [209] with the red region indicating the fabrication zone where the laser power is above zero watts, alluding to a rectangular part (see Figure 5-2b). Figure 5-2a only provides a

glimpse of a partial dataset; a complete dataset for printing a part consists of 25,051 lines of commands and 1,498 captured melt pool images when the camera is ON.

Figure 5-3 presents examples of raw melt pool images taken by the AMMT. These images are of two distinct types: (1) melt pool without noise (see Figure 5-3a and b), and (2) melt pool with noise (see Figure 5-3c~f). the former often resembles a burning comet with a tail, highlighted by the white region. Conversely, the latter exhibits the melt pool and spatters simultaneously, where the noise (i.e., the spatter) is either isolated from or attached to the main melt pool, marked by red arrows. Obviously, the splatter can lead to inaccurate measurements of the melt pool area [85] for the model training, which then reduces the accuracy of the trained relationships and prediction performance. Therefore, denoising processing is typically required to improve the quality of data.

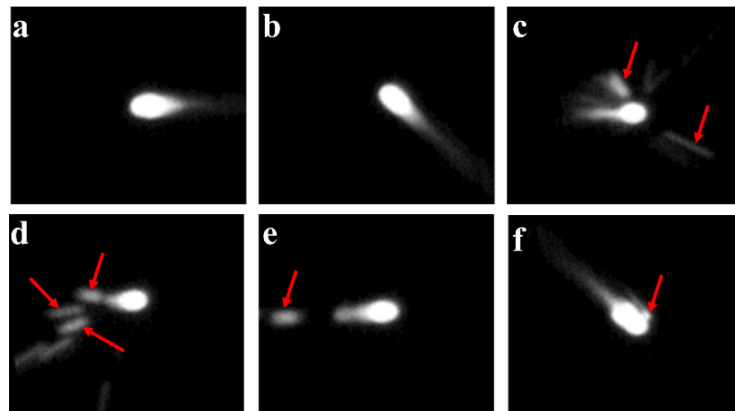


Figure 5-3: A few representative experimental melt pool images captured by Additive Manufacturing Metrology Testbed (AMMT) at the National Institute of Standards and Technology (NIST)

Note that sufficient high-quality are vital to guarantee the success of data-driven modeling [84]. In this context, a large number of experimental melt pool images after the denoising process are essential to satisfy this prerequisite. As mentioned above, one dataset for a single part includes 25,051 rows of commands and 1,498 captured images corresponding to 1,498 laser spots. In total, 32 datasets corresponding to 32 parts built at different locations in the same layer using the

identical printing pattern would result in 801632 rows of commands and 47936 melt pool images. This acquisition method used to obtain melt pool morphology shows a great potential to replace the general *ex-situ* characterization methods (e.g., optical microscope and scanning electron microscope). This potential stems from the direct relationship between the captured images and melt pool morphology. General methods for acquiring morphology are intricate, time-consuming, and costly due to multiple process steps and machinery [81][78]. In contrast, the advantage of intensive acquisition of *in-situ* melt pool morphology by AMMT is unparalleled. Further quality improvement of raw melt pool images is discussed in Section 5.3.1.

5.3 Machine learning methodologies

5.3.1 Convolutional neural network for denoising processing

The deep convolutional neural network (CNN) is selected among various machine learning (ML) algorithms for image denoising processing in this study. CNN features local connections, weight sharing, pooling, and multi-layer stack utilization, conferring substantial benefits in image processing. Within the Additive Manufacturing (AM) community, CNN has been extensively applied for tasks such as AM process monitoring [202], material property prediction [210], anomaly detection [211], quality monitoring [212]. For the extraction of the primary features of melt pools during denoising processing, the CNN structure utilized is illustrated in Figure 5-4. This structure comprises both convolution and deconvolution sections. The convolution part contains normalization layers, convolution layers, activation layers with the ReLU function, and pooling layers. Conversely, the deconvolution part encompasses upsampling layers, deconvolution layers, and output layers. This specific CNN is capable of intricate feature extraction, such as boundaries, textures, and morphologies [213]. A smooth and elliptical-shaped boundary mainly characterizes a real melt pool, whereas a noised melt pool exhibits an abnormal boundary due to

spatter interference. Thus, CNN is apt for denoising processing, removing spatter effects by autonomously adapting and learning regular boundary features.

Before the execution of CNN model training and validation, all raw melt pool images must undergo pre-processing to extract a clear region of interest (RoI). This involves image thresholding and hue inverting, as displayed in Figure 5-4. The primary principle for selecting the threshold level is to render the melt pool post-thresholding operation analogous to manual measurement [205][207]. Note that although the selected threshold level might not precisely represent the real melt pool, it enables the analysis of changing trends when considered a uniform standard. In this work, we use a grayscale level of 80% for all raw images, following NIST requirements. Grayscale varies from 0 (black) to 255 (white), with higher grayscale areas corresponding to higher temperature ranges. Subsequent to the thresholding operation, hue inverting is carried out to accentuate the region of interest (RoI) with black color. The resulting images are referred to as pre-processed raw images, as demonstrated on the right side of Figure 5-4.

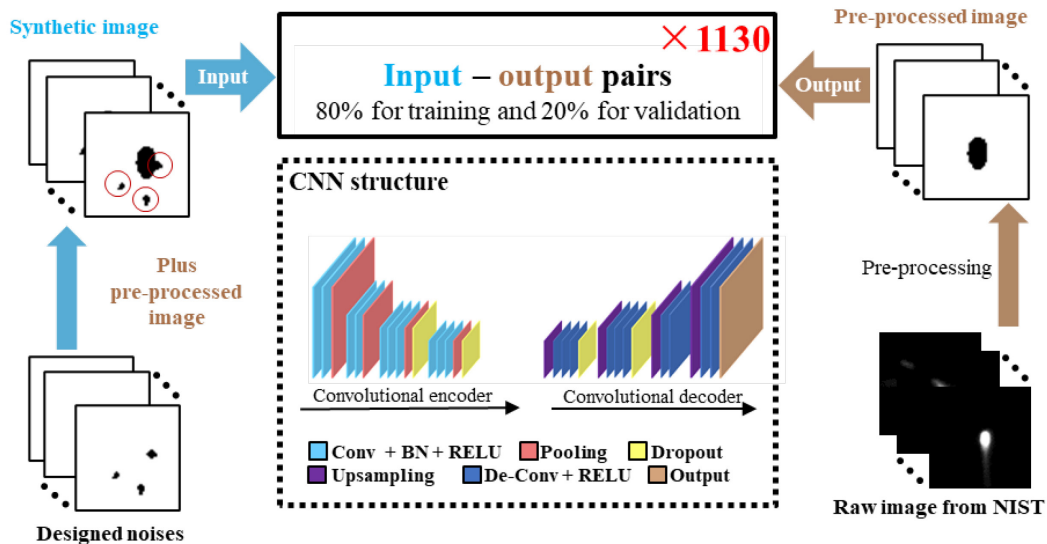


Figure 5-4: The developed convolutional neural network (CNN) model for denoising process of melt pool images

Training the CNN model successfully demands an ample number of input-output pairs to facilitate a full feature extraction of real melt pools and to eliminate spatter noise. These pairs

consist of noised images and their corresponding denoised counterparts, as indicated in Figure 5-4. A total of 1130 input-output pairs are generated, with 80% allocated for training and the remainder for validation. Denoising numerous noisy images manually to create required input-output pairs is impractical. Consequently, we generate such datasets in reverse by synthesizing noisy melt pools from clean ones. The input images are synthesized by introducing noise into pre-processed raw images devoid of noise (as outputs), forming synthetic images as inputs, as revealed on the left side of Figure 5-4. The designed noise in Figure 5-4 is created by imitating real noise throughout the NIST dataset, including its size, shape, and distributions (i.e., isolated or sometimes attached). Section 5.4.1 will present the validation result, and the data denoising capability of the CNN learned from synthetic melt pool images will be transferred directly to process real noisy images (see Section 5.4.2 for results). The derived noise-free images will then facilitate high-quality melt pool area data generation for predictive modeling in subsequent section.

5.3.2 Artificial neural network for melt pool prediction

This section mainly introduces our machine learning model for melt pool prediction and its structure comparison with the recent predictive models (NBEM and L-NBEM). Given the high-dimensional scanning history as input, artificial neural networks (ANNs) are trained for melt pool prediction, with the design portrayed in Figure 5-5. The multi-layer perceptron (MLP) artificial neural network utilized consists of one input layer, two hidden layers, and one output layer, with 60 neurons used per hidden layer. This optimal configuration yields improved results while minimizing computational costs.

The output layer represents the prediction objective, A_i , where the subscript i refers to the i^{th} melt pool image. This aligns with the i^{th} '2' order in the camera trigger column of the commands (Figure 5-2a). The melt pool area, A , is calculated using the center black color (each pixel grid is

64 μm^2) of denoised processed melt pool images by the trained CNN modeling outlined in Section 5.3.1.

The input layer includes (1) raw scanning history and (2) information regarding predictive laser spot i . The information of (2) mainly consists of the power P_i from commands and scan speed V_i , easily obtained as the distance-to-time interval ratio. These inputs symbolize the current energy density effects on the predictive melt pool area, in line with prior models [197][208]. Such considerations are reinforced by numerous studies demonstrating the close relationship between power, speed, energy density, and melt pool size [96].

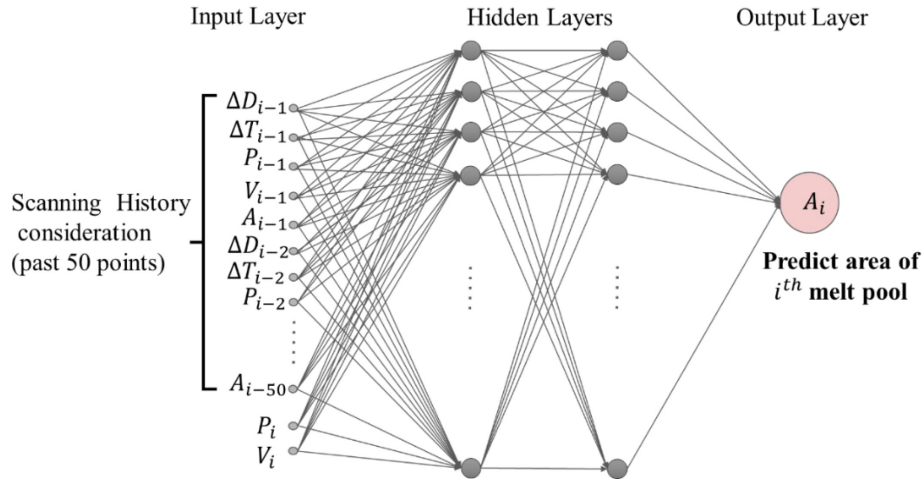


Figure 5-5: Structure of the Artificial Neural Network, where Δd_{i-1} and Δt_{i-1} correspond to distance and the time gap between points $i-1$ and the predictive point i , respectively, and P_{i-1} , V_{i-1} , and A_{i-1} indicate the power, scan speed, and melt pool area of laser spot $i-1$, respectively. Subscript i , for example, corresponds to the i^{th} melt pool images, i.e., the i^{th} '2' order of the camera trigger column in the commands (Figure 5-2a) in sequence.

The raw scanning history input must encompass sufficient past raw information, safeguarding the ANN from inaccuracies instigated by human-designed factors. This approach empowers the neural network to autonomously learn, iterate, and discern underlying laws, accounting for neighboring effects and other potential physics. In detail, the scanning history for predicting A_i mainly comprises the five kinds of information from the past 50 points (from $i-1$ to $i-50$), as presented in Figure 5-5. Using laser point $i-1$ as an example, the Δd_{i-1} and the Δt_{i-1} are the

Euclidean and time distance between point $i-1$ and the predictive point i , readily obtained from the commands. Other inputs for the past point $i-1$ include P_{i-1} , V_{i-1} , and A_{i-1} , providing raw data about power, scan speed, and melt pool area respectively. Due to the inclusion of 50 past points, there are 250 total inputs for scanning history. This evidently conserves more raw information compared to the two featured factors employed in the previous NBEM model. Additionally, the scanning history is more transparent and obtainable than the complex feature derivation process. When predicting the initial 50 points, zero values are set if there are insufficient inputs.

Table 5-1: Comparisons between our model, NBEM model, and L-NBEM model

| Model | Preparation | Inputs | Output | Prediction tool |
|--------|--------------|---|--------|----------------------------|
| NBEM | Characterize | $\theta_i^t, \theta_i^{td}, P_i, V_i$ | A_i | quadratic regression model |
| L-NBEM | Characterize | $\theta_i^t, \theta_i^{td}, P_i, V_i, A_{avg}, A_{max}, A_{var}, t_i, J, \lambda$ | A_i | ANN |
| Ours | Denoising | $(\Delta d_{i-50} \dots \Delta d_{i-1}, \Delta t_{i-1}, P_{i-1}, V_{i-1}, A_{i-1}), P_i, V_i$ | A_i | ANN |

* θ_i^t NBEM time factor, θ_i^{td} NBEM distance factor, P_i laser power, and V_i scan speed belong to track-wise inputs [208]. The layer-wise input variables [197] include J total energy input on the previous layer, λ laser idle time gap between previous layer and current layer, t_i building time from start point to the laser spot and A_{avg} mean, A_{max} maximum, and A_{var} standard deviation of the melt pool area of the L-NBEM region. A_i presents the melt pool area to be predicted.

Table 5-1 summarizes the structure comparisons of the aforementioned two recent melt pool predictive models and our developed counterparts, focusing on preparation, inputs, and training tools. Initially, the preparation phase for our model training entails a denoising process to exclude spatter effects on the real melt pool area (A), thereby enhancing input accuracy. Conversely, the other two models emphasize the acquisition of neighboring effect factors, undergoing a complex design and derivation process that necessitates professional, in-depth, and thoughtful consideration.

Secondly, the inputs for all three models vary except for the laser power P_i and scanning speed V_i , which directly relate to the melt pool area A_i . For the NBEM model, the two more inputs are mainly the neighboring factors responsible for neighboring effects. The L-NBEM model includes factors related to the previous layer, such as the total energy input J of the previous layer, the laser idle time gap λ between the previous layer and the current layer, the build time t_i from the starting point to the laser point, and the average A_{avg} , maximum A_{max} , and standard deviation A_{var} of the melt pool area. Clearly, factors that might influence the impact of past laser points on predicted points should be included as inputs in various forms, such as neighboring factors and inputs reflecting previous-layer effects. It should be noted that our focus is mainly on single-layer printing, similar to the NBEM model, without the need to consider other layer effects. In this study, the influence of previous laser spots is considered through scanning history inputs depicted in Figure 5-5. Gathering 250 values of scanning history inputs from the past 50 laser spots furnishes sufficient raw information. Specifically, the inputs of previous melt pool areas encapsulate the physical effect results directly and contain the fluctuation of melt pool area development. Lastly, the utilization of ANN within our model enables the self-adaptation of all potential physical effects on the predictive spot, afforded by the vast array of raw scanning history inputs. By contrast, though the quadratic regression model coupled with two featured factors can learn the effects of past laser points, it may concurrently lose partial information. In this study, 32 datasets are randomly divided into two parts: one containing 26 datasets for training models and the remaining part (6 groups) for testing. Namely, the 26 constructed parts are employed for model training to predict the melt pools for the other six unbuilt counterparts under different AM processes, hence adhering to an extrapolative predictive method.

5.4 Results

5.4.1 Denoising modeling validation

Figure 5-6a shows synthetic noisy melt pools as inputs, the CNN-predicted melt pool by trained CNN modeling, and the pre-processed melt pools, namely, ground truth. The CNN-predicted melt images exhibit negligible differences from the ground truth, affirming the efficacy of the CNN model in eliminating the introduced noise and accurately replicating the actual melt pool. The model proves particularly effective when the noise is isolated from the melt pools, and in instances where the noise adheres to the melt pool, the model is able to accurately distinguish the boundaries of the melt pool and remove the excess as noise. Figure 5-6b presents the training and validation loss curves [214] to evaluate the designed CNN model. The close parallelism of these curves suggests that the Artificial Neural Network (ANN) model is well-trained, free from both overfitting and underfitting [215]. The gradual decrease of the training and validation loss culminates in a low value of 0.0003 after 175 epochs, further indicating that the CNN model has been well trained and validated using the designated data (Figure 5-4). This trained and validated CNN model is then utilized to process the noisy raw images as detailed in Section 5.4.1. Finally, the denoised images will be employed to calculate the melt pool area based on the pixel area for the actual melt pool, which is one of the inputs and the training objective for our predictive models.

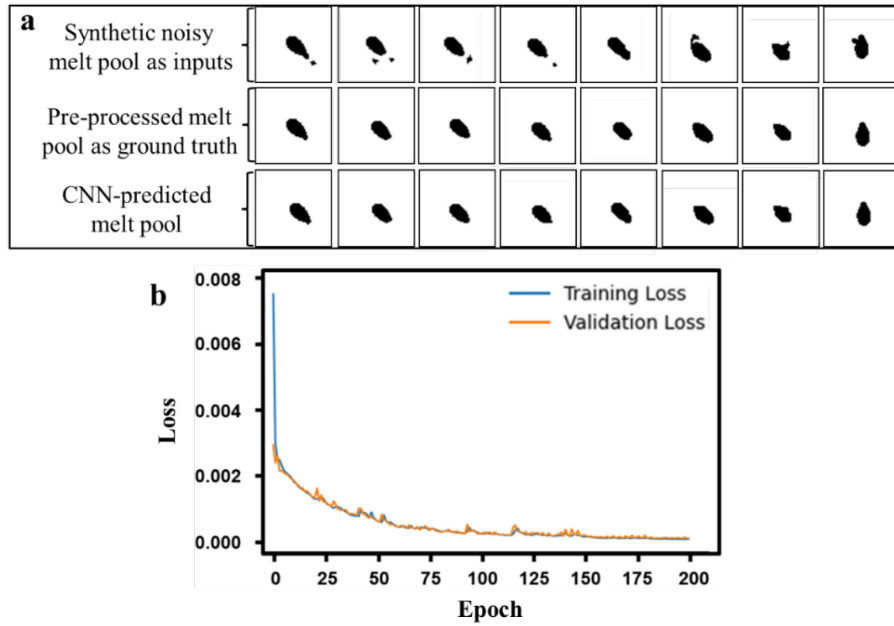


Figure 5-6: (a) Eight validation results, and (b) the training and validation loss plots of the CNN model.

5.4.2 Melt pool denoising

Figure 5-7 shows the raw melt pool image sourced from NIST, corresponding noisy melt pool image by pre-processing (i.e., image thresholding operation and hue inverting), denoised images by the trained-CNN, and ground truth (manually denoised). The area of each melt pool is provided for quantitative comparison. Pre-processing reveals that some small black spots persist in the pre-processed images (i.e., noisy melt pool in Figure 5-4). This confirms that the thresholding operation is incapable of entirely eliminating spatters. Consequently, the calculated melt pool area may exceed the ground truth, leading to an overestimation of the melt pool area. This underscores the importance of the subsequent denoising process by the trained CNN to yield an accurate melt pool area close to the ground truth, thereby improving prediction.

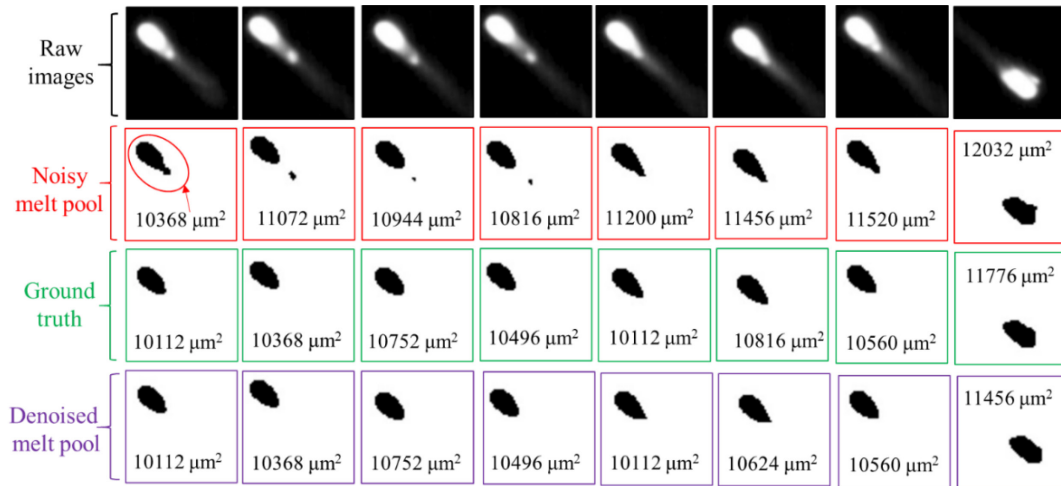


Figure 5-7: Eight testing results of the denoising process performed on real noisy melt pool images by the trained CNN.

Upon performing the denoising process with the CNN model, it is evident that the denoised melt pool closely mirrors the ground truth, with only minor differences in certain cases. This validates the effectiveness and capability of the developed CNN model to eradicate spatter noise from real noisy melt pool images. When compared with the calculated area, the denoised results align well with the corresponding ground truth. The area discrepancy caused by spatters can reduce by up to 15% following the denoising process. It is worth noting that minor differences between noisy and denoised pools may occur when the spatter adheres to the melt pool boundary. Nonetheless, the trained CNN can accurately delineate the actual melt pool boundaries, making the denoised melt pool closely resemble the ground truth.

5.4.3 Melt pool prediction

Figure 5-8 compares the performance of our predictive model with the NBEM model using the Average Relative Error Magnitude (AREM). The AREM is a widely-used metric for evaluating prediction performance [111][197][201][216], signifying the average error for all predictions in a given testing dataset. For a rigorous comparison, the NBEM is revised using the same ANN model for training, while retaining the original input features designed for the previous NBEM model, as

shown in Table 5-1: Comparisons between our model, NBEM model, and L-NBEM model. Using our datasets, the highest AREM of NBEM is approximately 18%, with an average of 14.8%, as illustrated in Figure 5-8. In contrast, our proposed model exhibits excellent performance, with an AREM value as low as about 2.8%. This represents an at least 80% reduction in AREM compared to the NBEM model, thereby significantly improving prediction accuracy. This can largely be attributed to the input design, particularly the immense raw information of scanning history. These inputs enable the ANN to fully incorporate scanning history as a condition to inform melt pool development at the predictive location. Moreover, unlike L-NBEM [197] and revised NBEM, there are no significant AREM fluctuations for all testing datasets, reflecting the stability and generalizability of the proposed model.

However, it should be acknowledged that the denoising process has a negligible impact on AREM, as presented in Figure 5-8. The improvement resulting from data denoising is not apparent in this context due to the exceptionally small number and distribution of noise in all datasets. To verify this, we examine the area difference caused by noise. Figure 5-9a presents the accumulated area difference caused by noise in each dataset. Overall, it is evident that noise causes relatively small accumulation area differences in 32 datasets, with only eight datasets showing an accumulated area difference ranging from 192 to 5056 μm^2 . Even for dataset 1 with the highest accumulated area difference, over 99.1% of raw images are free of noise, as shown in Figure 5-9b. Consequently, noise data comprise only a small portion of the datasets. This can be attributed to the small range of laser power and low energy density used during AM [203][217][218] and the well-designed AMMT system [111][197]. Noise side effects are further discussed in Section 5.5.1.

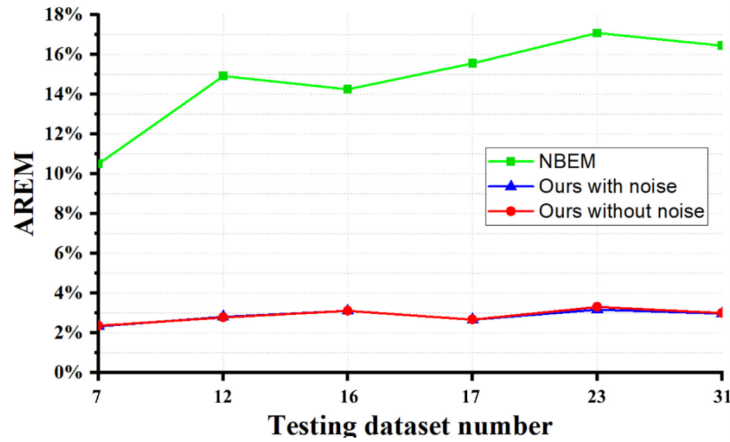


Figure 5-8: Comparison of average relative error magnitude (AREM) in melt pool area prediction between NBEM and our model (with/without noise) for different testing groups.

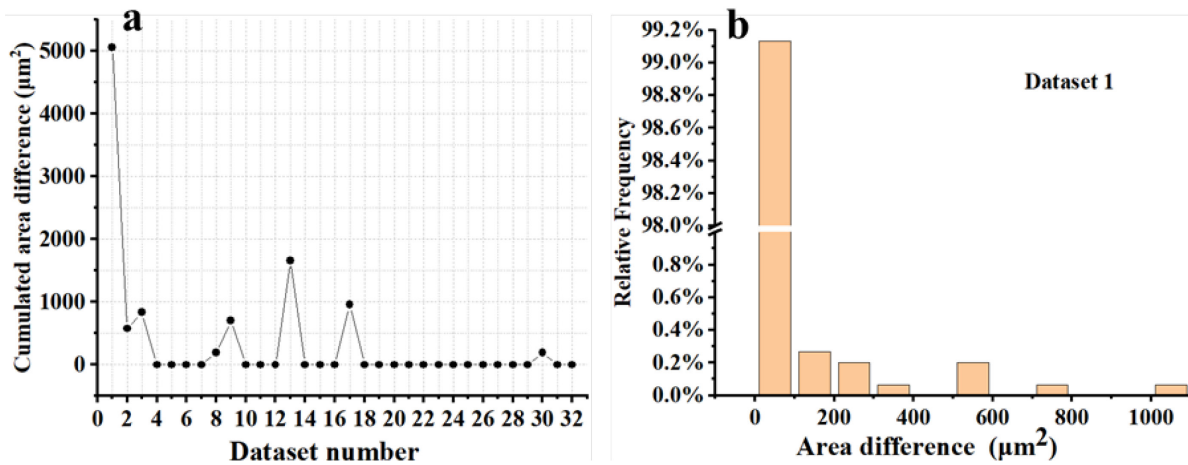


Figure 5-9: (a) cumulated area difference of melt pool between ground truth and noisy melt pool for each dataset, and (b) the relative frequency of melt pool area difference for dataset 1.

To visually compare the prediction results of different models with ground truth, the melt pool area distributions of testing datasets 16 and 23 are mapped into contour plots, as shown in Figure 5-10. It is evident that all models can predict the general trend of area change, especially for the large melt pool at the turning points where significant heat accumulation occurs. However, the similarity of the predictions by different models to the ground truth varies. The area predicted by our model is almost consistent with the ground truth due to the exceptionally low AREM of 2.8%, further demonstrating the high predictive performance and reliability of our proposed model. In contrast, the overall predictions by NBEM are slightly lower than the ground truth, particularly

evident at the turning points with the highest heat accumulation. Moreover, NBEM fails to accurately predict the slight fluctuations of the melt pool (indicated by black circles) at locations where heat accumulation is not significant enough. Even worse, the P-V model can only determine the relative size of the melt pool where heat build-up is most intense, resulting in significantly lower overall prediction results compared to the ground truth. In summary, the combination of the designed scanning history input features and the ANN technique significantly improves the prediction performance of our model. Note that these conclusions do not negate the importance of the denoising process, which will be further discussed in Section 5.5.1.

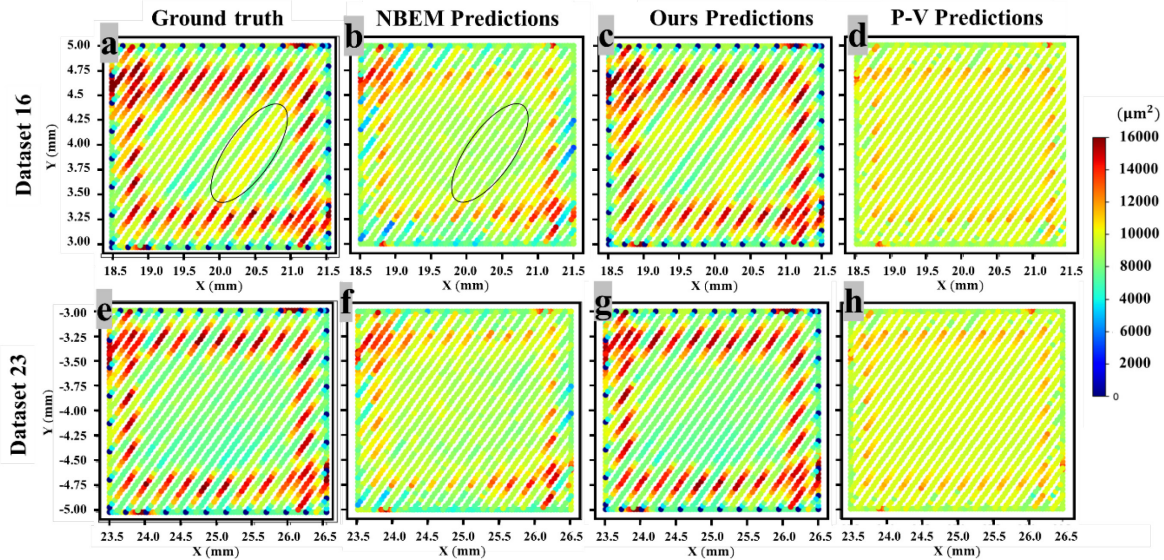


Figure 5-10: Contour plots of the melt pool area predicted by different models as well as ground truth for testing dataset 16 and 23.

5.5 Discussion

5.5.1 Noise effects

Although the current datasets provided by NIST contain rare noise, it is widely observed that the melt pool exposed under a high-speed camera is susceptible to interference from spatters and plumes [203][204][205][206]. Therefore, the denoising process remains essential for studies focused on melt pools. To further demonstrate the significance of data denoising in improving

model performance, we intentionally increase the noise level in the melt pool datasets. This comprehensive examination allows us to understand how noise deteriorates prediction performance and emphasizes the importance of the denoising process proposed in this research.

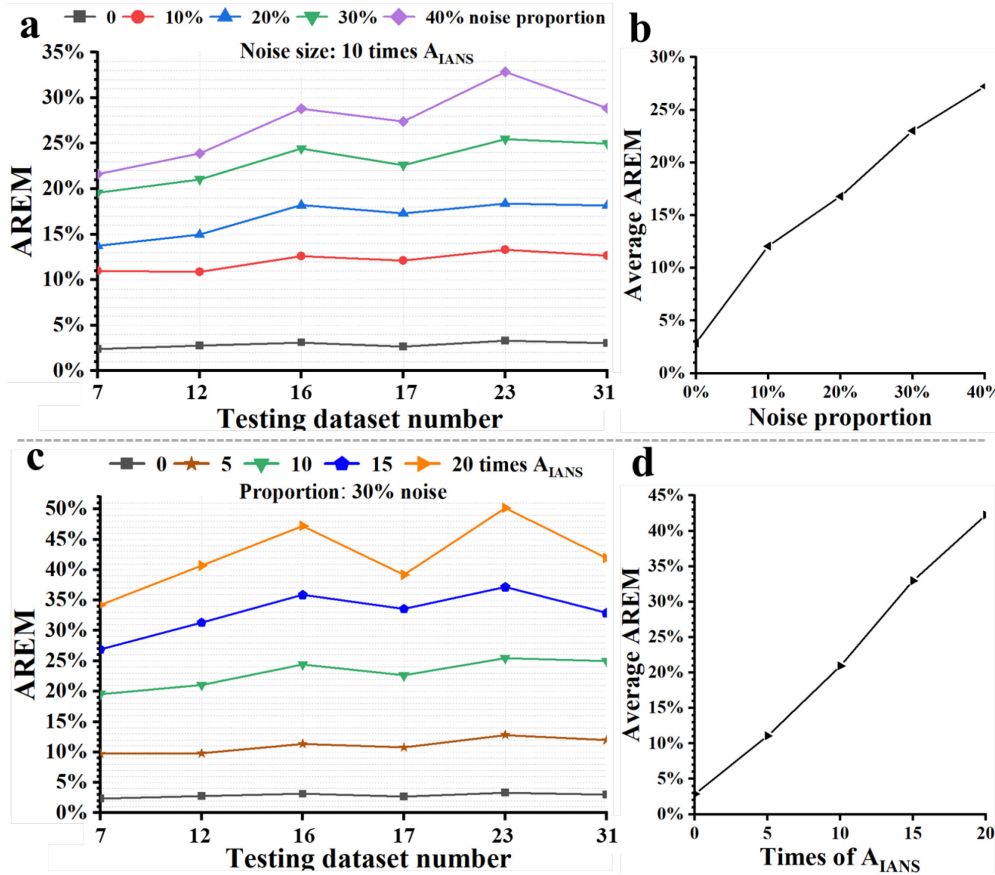


Figure 5-11: With a designed Gaussian normal distribution noise, the AREM changes with (a) noise proportion and (c) noise size (times of initial added noise size A_{IANS}) for each testing dataset. The average AREM changes against (b) noise proportion and (d) noise size.

The artificial designed method is performed by adding a specific noise size (noise area) in a certain proportion of the raw data (the melt pool area) as noised melt pools in each dataset. The added noise follows a Gaussian normal distribution, with a mean value of $350.89 \mu\text{m}^2$ and a standard deviation of $256.88 \mu\text{m}^2$, calculated based on all existing noisy data in the entire datasets. Note that $350.89 \mu\text{m}^2$ is set as the initial added noise size (A_{IANS}). Figure 5-11 shows the variations in AREM as a function of noise proportion and noise size, represented as times of A_{IANS} . These two factors significantly influence prediction performance. As shown in Figure 5-11a, with a

constant noise size (10 times of A_{IANS}), the AREM obviously increases with noise proportion for each dataset, along with increased fluctuations. The average AREM linearly increases from 2.88% to 27.24% as the noise proportion varies from 0 to 40%, as shown in Figure 5-11b. When fixing a 30% noise addition, a similar trend is observed with noise size, as depicted in Figure Figure 5-11c. The average AREM also linearly increases from 2.88% to 42.25%.

To better visualize the noise side effects, the melt pool area distributions of dataset 16 before and after noise addition and prediction are mapped into contour plots, as presented in Figure 5-12. Comparing Figure 5-12c and 12e with 12a, it is evident that the presence of noise leads to chaotic prediction results, severely deviating from the ground truth (Figure 5-12). From Figure 5-12a, the ARME for the predictions of Figure 5-12c and Figure 5-12e is 12.6% and 24.4%, respectively, compared to a very low AREM of 3.0% in Figure 5-12a, which closely resembles the ground truth. This difference is mainly attributed to the fact that the prediction model trained using noisy datasets fails to learn the underlying relationships and physics accurately, as the noise presence likely misleads the relationships established during model training. To further examine whether the model trained using noisy datasets can identify the noise, noise is added into the ground truth shown in Figure 5-12d. In contrast, more deviation from ground truth is presented in Figure 5-12c, indicating that models trained using noisy datasets cannot automatically learn the noise interference and produce results similar to those in Figure 5-12d. This further emphasizes the necessity to remove noise before training the ANN model. As more and larger noise is added, the predictions presented in Figure 5-12e show a much more disordered distribution, indicating that trained model has almost completely lost its predictive ability and even is unable to learn the thermal accumulation physics at the turning points.

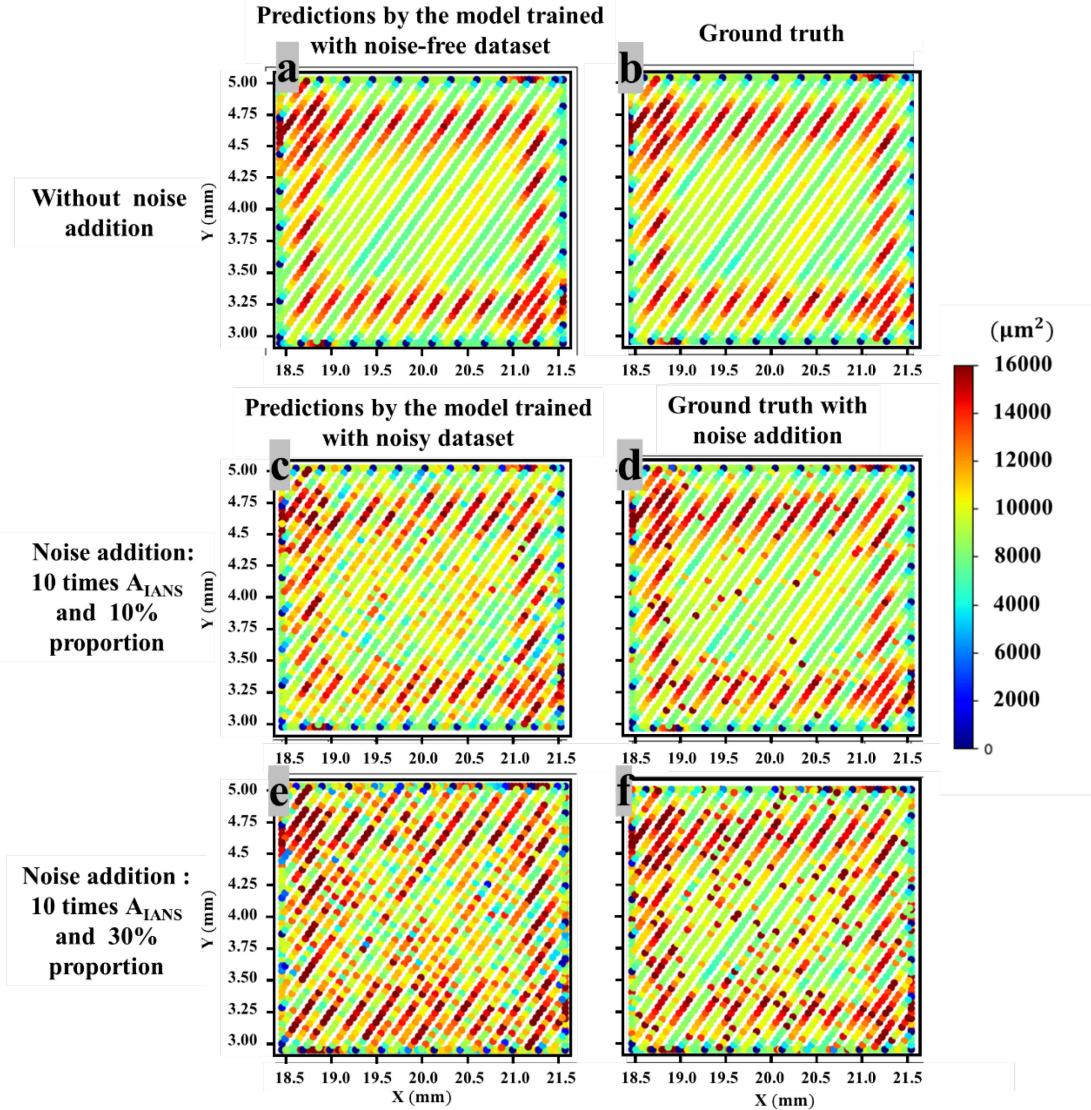


Figure 5-12: Contour plots of (a) melt pool area predictions by the trained ANN model with noise-free datasets, i.e., Figure 5-10c, (b) ground truth, i.e., Figure 5-10a, (c)(e) melt pool area predictions by the trained ANN model with noisy datasets, and (d)(f) ground truth with noise addition in dataset 16.

5.6 Chapter conclusions

In summary, we have proposed an experimental data-driven model by using the machine learning technique, enabling fast extrapolative melt pool prediction for unbuilt parts. Some important conclusions are listed as below:

1. The denoising process is performed using a convolutional neural network (CNN) model trained on synthetic melt pool images as inputs containing designed noise (e.g., spatters)

and corresponding real melt pools as outputs. This ensures sufficient exposure to real melt pool features under various noise interferences. The trained model can accurately identify the real melt pool and effectively exclude spatters, ensuring the accurate calculation of the melt pool area as the input for our predictive model.

2. An artificial neural network (ANN) is trained for melt pool area prediction using the extensive datasets from NIST. The input design of scanning history results in a significant reduction in the average relative error magnitude (AREM) to 2.8% compared to the recent NBEM model's 14.8%, an 81% reduction. This improvement can be attributed to the scanning history inputs containing vast raw information of past laser spots, allowing the multi-layer perceptron of the ANN to self-adapt to melt pool development effects (e.g., physics and fluctuation).
3. We have demonstrated that noise can deteriorate prediction performance through artificially designed noise strategies. Increasing the proportion and size of noise results in the ANN model losing its ability to learn thermal physics accurately, leading to an inability to predict melt pools with noise interference. Therefore, the denoising process is essential to remove noise interference and establish a reliable association between the input and the target (melt pool area in this study).

This designed method can be easily extended to multi-layer printing by incorporating the scanning history, including qualified laser spot information from previous layers. Additionally, other ML models (e.g., random forest model and support vector machine) can be used for parametric studies and further comparisons [219], which are not addressed in this paper due to the exceptionally small AREM achieved (2.8%). However, the AMMT system enables *in-situ* capturing of the 2D surface of the melt pool, but visualizing the 3D melt pool shape quickly remains a challenge with the existing in-situ monitors. Incorporating a physical model or a physics-

informed data-driven model may be a possible approach to correlate the captured 2D melt pool with the 3D counterpart in the future.

Chapter 6: Conclusion and Perspectives

In this dissertation, the focus was placed on the intricate processes of additive manufacturing (AM), with particular attention given to the microstructural development understanding in the context of dynamic thermal conditions, flow-driven compositional redistribution, and data-driven modeling. . The ultimate objective is to deepen understanding of the complex AM process-microstructure relationship for enhanced quality control and performance improvement.

Throughout the conducted studies, a comprehensive understanding was gained on microstructural development under dynamic conditions. Specifically, the gradient structures featured with different phases in AM-fabricated Ti-6Al-4V were thoroughly examined. Thermal simulation and experimental design enabled the systematic exploration and validation of location-dependent phase evolution, which results from periodically attenuated thermal cycles. Moreover, the study has shown that flow behaviors at the interface of the bimetallic structures of SS316L and IN625 during directed energy deposition (DED) could lead to composition redistribution. This, in turn, changes the liquidus temperature in the mixing zone at the interface, influencing the solidification sequence and the final grain structure. These findings significantly enhance our understanding of bimetal additive manufacturing. Finally, in order to efficiently establish the complex AM process-microstructure relationships for microstructure optimization and quality control, a data-driven modeling framework was established. By harnessing experimental data inputs from the National Institute of Standards and Technology (NIST), this framework facilitates swift and cost-effective extrapolative melt pool predictions for unbuilt parts.

However, it is important to recognize that the research conducted in this dissertation is only a part of the broader narrative on AM microstructural evolution and optimization due to the complex physics of AM processes. As such, several perspectives for future work emerge:

Broadening Metal Species Scope: The study focused on Ti-6Al-4V and bimetallic structures of SS316L and IN625. Expanding the metal species scope to include other metals used in AM would further enrich the understanding of AM microstructure development, which can boost material development and customization.

Expanding Data-Driven Modeling: While the data-driven modeling framework established shows promise, there is always room for practical application. Future work could focus on reverse design of processing parameters to get desired microstructures and even properties.

Investigating Other Microstructural Features: Apart from phase evolution and grain structure, other microstructural features, such as defects and texture, can also significantly influence the final product quality and performance in AM. Future studies can integrate these aspects into the AM process-microstructure relationship.

Incorporating Real-time Process Monitoring: Real-time monitoring techniques can be incorporated into the AM process to provide continuous data, enabling in-situ detection. Then in-situ correction of defects or variations can be achieved via adapted AM process, guided by rapid data-driven modeling feedback.

In conclusion, the findings within this dissertation contribute to the ongoing conversation around microstructural evolution in metal additive manufacturing. The approaches adopted and insights gleaned represent one attempt among many to grapple with the complexities of the AM process-microstructure relations. There is much work to be done and many questions still to answer. It is hoped that this work provides a useful platform (i.e., the physics-based framework) for other

researchers and serves to catalyze further exploration of this transformative technology. We are still at the foothills of understanding, and the potential for discovery and improvement in this field remains vast.

References

- [1] N. Ur Rahman *et al.*, “Directed energy deposition and characterization of high-carbon high speed steels,” *Addit. Manuf.*, 2019, doi: 10.1016/j.addma.2019.100838.
- [2] M. J. Bermingham, D. H. StJohn, J. Krynen, S. Tedman-Jones, and M. S. Dargusch, “Promoting the columnar to equiaxed transition and grain refinement of titanium alloys during additive manufacturing,” *Acta Mater.*, 2019, doi: 10.1016/j.actamat.2019.02.020.
- [3] D. Zhang *et al.*, “Additive manufacturing of ultrafine-grained high-strength titanium alloys,” *Nature*, 2019, doi: 10.1038/s41586-019-1783-1.
- [4] A. Thiriet, C. Schneider-Maunoury, P. Laheurte, D. Boisselier, and L. Weiss, “Multiscale study of different types of interface of a buffer material in powder-based directed energy deposition: Example of Ti6Al4V/Ti6Al4V - Mo/Mo - Inconel 718,” *Addit. Manuf.*, 2019, doi: 10.1016/j.addma.2019.02.007.
- [5] J. Wang, Q. Luo, H. Wang, Y. Wu, X. Cheng, and H. Tang, “Microstructure characteristics and failure mechanisms of Ti-48Al-2Nb-2Cr titanium aluminide intermetallic alloy fabricated by directed energy deposition technique,” *Addit. Manuf.*, 2020, doi: 10.1016/j.addma.2019.101007.
- [6] L. Scime and J. Beuth, “Melt pool geometry and morphology variability for the Inconel 718 alloy in a laser powder bed fusion additive manufacturing process,” *Addit. Manuf.*, 2019, doi: 10.1016/j.addma.2019.100830.
- [7] A. A. Martin *et al.*, “Dynamics of pore formation during laser powder bed fusion additive manufacturing,” *Nat. Commun.*, 2019, doi: 10.1038/s41467-019-10009-2.
- [8] G. L. Knapp, N. Raghavan, A. Plotkowski, and T. DebRoy, “Experiments and simulations on solidification microstructure for Inconel 718 in powder bed fusion electron beam additive manufacturing,” *Addit. Manuf.*, 2019, doi: 10.1016/j.addma.2018.12.001.
- [9] A. R. Nassar, M. A. Gundermann, E. W. Reutzel, P. Guerrier, M. H. Krane, and M. J. Weldon, “Formation processes for large ejecta and interactions with melt pool formation in powder bed fusion additive manufacturing,” *Sci. Rep.*, 2019, doi: 10.1038/s41598-019-41415-7.
- [10] C. L. A. Leung, S. Marussi, M. Towrie, R. C. Atwood, P. J. Withers, and P. D. Lee, “The effect of powder oxidation on defect formation in laser additive manufacturing,” *Acta Mater.*, 2019, doi: 10.1016/j.actamat.2018.12.027.
- [11] L. D. Bobbio *et al.*, “Additive manufacturing of a functionally graded material from Ti-6Al-

- 4V to Invar: Experimental characterization and thermodynamic calculations,” *Acta Mater.*, 2017, doi: 10.1016/j.actamat.2016.12.070.
- [12] L. D. Bobbio *et al.*, “Characterization of a functionally graded material of Ti-6Al-4V to 304L stainless steel with an intermediate V section,” *J. Alloys Compd.*, 2018, doi: 10.1016/j.jallcom.2018.01.156.
- [13] D. C. Hofmann *et al.*, “Developing gradient metal alloys through radial deposition additive manufacturing,” *Sci. Rep.*, 2014, doi: 10.1038/srep05357.
- [14] B. E. Carroll *et al.*, “Functionally graded material of 304L stainless steel and inconel 625 fabricated by directed energy deposition: Characterization and thermodynamic modeling,” *Acta Mater.*, 2016, doi: 10.1016/j.actamat.2016.02.019.
- [15] A. Reichardt *et al.*, “Development and characterization of Ti-6Al-4V to 304L stainless steel gradient components fabricated with laser deposition additive manufacturing,” *Mater. Des.*, 2016, doi: 10.1016/j.matdes.2016.05.016.
- [16] A. Saboori, A. Aversa, G. Marchese, S. Biamino, M. Lombardi, and P. Fino, “Application of directed energy deposition-based additive manufacturing in repair,” *Applied Sciences (Switzerland)*. 2019. doi: 10.3390/app9163316.
- [17] S. Zhu, W. Chen, X. Zhan, L. Ding, and J. Zhou, “Parameter optimisation of laser cladding repair for an Invar alloy mould,” *Proc. Inst. Mech. Eng. Part B J. Eng. Manuf.*, 2019, doi: 10.1177/0954405418805653.
- [18] U. Scipioni Bertoli, A. J. Wolfer, M. J. Matthews, J. P. R. Delplanque, and J. M. Schoenung, “On the limitations of Volumetric Energy Density as a design parameter for Selective Laser Melting,” *Mater. Des.*, 2017, doi: 10.1016/j.matdes.2016.10.037.
- [19] C. Panwisawas, Y. T. Tang, and R. C. Reed, “Metal 3D printing as a disruptive technology for superalloys,” *Nature Communications*. 2020. doi: 10.1038/s41467-020-16188-7.
- [20] P. W. Liu *et al.*, “Investigation on evolution mechanisms of site-specific grain structures during metal additive manufacturing,” *J. Mater. Process. Technol.*, 2018, doi: 10.1016/j.jmatprotec.2018.02.042.
- [21] A. Basak and S. Das, “Epitaxy and Microstructure Evolution in Metal Additive Manufacturing,” *Annual Review of Materials Research*. 2016. doi: 10.1146/annurev-matsci-070115-031728.
- [22] S. Das, “Physical Aspects of Process Control in Selective Laser Sintering of Metals,” *Advanced Engineering Materials*. 2003. doi: 10.1002/adem.200310099.
- [23] F. Yan, W. Xiong, and E. J. Faierson, “Grain structure control of additively manufactured metallic materials,” *Materials (Basel)*., 2017, doi: 10.3390/ma10111260.
- [24] P. Liu, Z. Wang, Y. Xiao, M. F. Horstemeyer, X. Cui, and L. Chen, “Insight into the

- mechanisms of columnar to equiaxed grain transition during metallic additive manufacturing,” *Addit. Manuf.*, 2019, doi: 10.1016/j.addma.2018.12.019.
- [25] Y. M. Ren, X. Lin, X. Fu, H. Tan, J. Chen, and W. D. Huang, “Microstructure and deformation behavior of Ti-6Al-4V alloy by high-power laser solid forming,” *Acta Mater.*, 2017, doi: 10.1016/j.actamat.2017.04.026.
- [26] A. A. Antonysamy, J. Meyer, and P. B. Prangnell, “Effect of build geometry on the β -grain structure and texture in additive manufacture of Ti6Al4V by selective electron beam melting,” *Mater. Charact.*, 2013, doi: 10.1016/j.matchar.2013.07.012.
- [27] J. Nguejio, F. Szmytka, S. Hallais, A. Tanguy, S. Nardone, and M. Godino Martinez, “Comparison of microstructure features and mechanical properties for additive manufactured and wrought nickel alloys 625,” *Mater. Sci. Eng. A*, 2019, doi: 10.1016/j.msea.2019.138214.
- [28] M. Javidani, J. Arreguin-Zavala, J. Danovitch, Y. Tian, and M. Brochu, “Additive Manufacturing of AlSi10Mg Alloy Using Direct Energy Deposition: Microstructure and Hardness Characterization,” *J. Therm. Spray Technol.*, 2017, doi: 10.1007/s11666-016-0495-4.
- [29] R. Acharya, J. A. Sharon, and A. Staroselsky, “Prediction of microstructure in laser powder bed fusion process,” *Acta Mater.*, 2017, doi: 10.1016/j.actamat.2016.11.018.
- [30] T. T. Roehling *et al.*, “Modulating laser intensity profile ellipticity for microstructural control during metal additive manufacturing,” *Acta Mater.*, 2017, doi: 10.1016/j.actamat.2017.02.025.
- [31] N. Raghavan *et al.*, “Numerical modeling of heat-transfer and the influence of process parameters on tailoring the grain morphology of IN718 in electron beam additive manufacturing,” *Acta Mater.*, vol. 112, pp. 303–314, 2016, doi: 10.1016/j.actamat.2016.03.063.
- [32] K. Karami *et al.*, “Continuous and pulsed selective laser melting of Ti6Al4V lattice structures: Effect of post-processing on microstructural anisotropy and fatigue behaviour,” *Addit. Manuf.*, 2020, doi: 10.1016/j.addma.2020.101433.
- [33] N. Raghavan *et al.*, “Localized melt-scan strategy for site specific control of grain size and primary dendrite arm spacing in electron beam additive manufacturing,” *Acta Mater.*, 2017, doi: 10.1016/j.actamat.2017.08.038.
- [34] P. A. Kobryn and S. L. Semiatin, “Microstructure and texture evolution during solidification processing of Ti-6Al-4V,” *J. Mater. Process. Technol.*, 2003, doi: 10.1016/S0924-0136(02)00865-8.
- [35] C. J. Todaro *et al.*, “Grain structure control during metal 3D printing by high-intensity ultrasound,” *Nat. Commun.*, 2020, doi: 10.1038/s41467-019-13874-z.

- [36] J. H. Martin, B. D. Yahata, J. M. Hundley, J. A. Mayer, T. A. Schaedler, and T. M. Pollock, "3D printing of high-strength aluminium alloys," *Nature*, 2017, doi: 10.1038/nature23894.
- [37] P. Kiani, A. D. Dupuy, K. Ma, and J. M. Schoenung, "Directed energy deposition of AlSi10Mg: Single track nonscalability and bulk properties," *Mater. Des.*, 2020, doi: 10.1016/j.matdes.2020.108847.
- [38] H. Galarraga, D. A. Lados, R. R. Dehoff, M. M. Kirka, and P. Nandwana, "Effects of the microstructure and porosity on properties of Ti-6Al-4V ELI alloy fabricated by electron beam melting (EBM)," *Addit. Manuf.*, 2016, doi: 10.1016/j.addma.2016.02.003.
- [39] C. Schaak, W. Tillmann, M. Schaper, and M. E. Aydinöz, "Process gas infiltration in Inconel 718 samples during SLM processing," *RTeJournal-Fachforum für Rapid Technol.*, vol. 2016, no. 1, 2016.
- [40] C. Weingarten, D. Buchbinder, N. Pirch, W. Meiners, K. Wissenbach, and R. Poprawe, "Formation and reduction of hydrogen porosity during selective laser melting of AlSi10Mg," *J. Mater. Process. Technol.*, 2015, doi: 10.1016/j.jmatprotec.2015.02.013.
- [41] A. Sola and A. Nouri, "Microstructural porosity in additive manufacturing: The formation and detection of pores in metal parts fabricated by powder bed fusion," *J. Adv. Manuf. Process.*, 2019, doi: 10.1002/amp2.10021.
- [42] X. Wang, Y. Liu, L. Li, C. O. Yenusah, Y. Xiao, and L. Chen, "Multi-scale phase-field modeling of layer-by-layer powder compact densification during solid-state direct metal laser sintering," *Mater. Des.*, 2021, doi: 10.1016/j.matdes.2021.109615.
- [43] K. Moussaoui, W. Rubio, M. Mousseigne, T. Sultan, and F. Rezai, "Effects of Selective Laser Melting additive manufacturing parameters of Inconel 718 on porosity, microstructure and mechanical properties," *Mater. Sci. Eng. A*, 2018, doi: 10.1016/j.msea.2018.08.037.
- [44] S. Liu and Y. C. Shin, "Additive manufacturing of Ti6Al4V alloy: A review," *Mater. Des.*, 2019, doi: 10.1016/j.matdes.2018.107552.
- [45] P. J. Arrazola, A. Garay, L. M. Iriarte, M. Armendia, S. Marya, and F. Le Maître, "Machinability of titanium alloys (Ti6Al4V and Ti555.3)," *Journal of Materials Processing Technology*. 2009. doi: 10.1016/j.jmatprotec.2008.06.020.
- [46] T. Ahmed and H. J. Rack, "Phase transformations during cooling in $\alpha+\beta$ titanium alloys," *Mater. Sci. Eng. A*, 1998, doi: 10.1016/s0921-5093(97)00802-2.
- [47] S. M. Kelly, "Thermal and Microstructure Modeling of Metal Deposition Processes with Application to Ti-6Al-4V," *Mater. Sci. Eng.*, 2004.
- [48] B. Vrancken, L. Thijs, J. P. Kruth, and J. Van Humbeeck, "Heat treatment of Ti6Al4V produced by Selective Laser Melting: Microstructure and mechanical properties," *J. Alloys Compd.*, 2012, doi: 10.1016/j.jallcom.2012.07.022.

- [49] L. Facchini, E. Magalini, P. Robotti, A. Molinari, S. Höges, and K. Wissenbach, “Ductility of a Ti-6Al-4V alloy produced by selective laser melting of prealloyed powders,” *Rapid Prototyp. J.*, 2010, doi: 10.1108/13552541011083371.
- [50] L. E. Murr *et al.*, “Microstructure and mechanical behavior of Ti-6Al-4V produced by rapid-layer manufacturing, for biomedical applications,” *Journal of the Mechanical Behavior of Biomedical Materials*. 2009. doi: 10.1016/j.jmbbm.2008.05.004.
- [51] J. Yang, H. Yu, J. Yin, M. Gao, Z. Wang, and X. Zeng, “Formation and control of martensite in Ti-6Al-4V alloy produced by selective laser melting,” *Mater. Des.*, 2016, doi: 10.1016/j.matdes.2016.06.117.
- [52] P. K. Gokuldoss, S. Kolla, and J. Eckert, “Additive manufacturing processes: Selective laser melting, electron beam melting and binder jetting-selection guidelines,” *Materials*. 2017. doi: 10.3390/ma10060672.
- [53] W. Xu *et al.*, “Additive manufacturing of strong and ductile Ti-6Al-4V by selective laser melting via in situ martensite decomposition,” *Acta Mater.*, 2015, doi: 10.1016/j.actamat.2014.11.028.
- [54] W. Xu, E. W. Lui, A. Pateras, M. Qian, and M. Brandt, “In situ tailoring microstructure in additively manufactured Ti-6Al-4V for superior mechanical performance,” *Acta Mater.*, 2017, doi: 10.1016/j.actamat.2016.12.027.
- [55] C. Qiu, N. J. E. Adkins, and M. M. Attallah, “Microstructure and tensile properties of selectively laser-melted and of HIPed laser-melted Ti-6Al-4V,” *Mater. Sci. Eng. A*, 2013, doi: 10.1016/j.msea.2013.04.099.
- [56] C. de Formanoir *et al.*, “Micromechanical behavior and thermal stability of a dual-phase $\alpha+\alpha'$ titanium alloy produced by additive manufacturing,” *Acta Mater.*, 2019, doi: 10.1016/j.actamat.2018.09.050.
- [57] C. de Formanoir *et al.*, “A strategy to improve the work-hardening behavior of Ti-6Al-4V parts produced by additive manufacturing,” *Mater. Res. Lett.*, 2017, doi: 10.1080/21663831.2016.1245681.
- [58] L. Qian, J. Mei, J. Liang, and X. Wu, “Influence of position and laser power on thermal history and microstructure of direct laser fabricated Ti-6Al-4V samples,” *Mater. Sci. Technol.*, 2005, doi: 10.1179/174328405x21003.
- [59] S. L. Lu, M. Qian, H. P. Tang, M. Yan, J. Wang, and D. H. StJohn, “Massive transformation in Ti-6Al-4V additively manufactured by selective electron beam melting,” *Acta Mater.*, 2016, doi: 10.1016/j.actamat.2015.11.011.
- [60] Z. Ren and F. Ernst, “High-temperature phase transformations in AISI 316 stainless steel infused with concentrated interstitial carbon,” *J. Alloys Compd.*, 2020, doi: 10.1016/j.jallcom.2019.153000.

- [61] Y. Zhong *et al.*, “Additive manufacturing of 316L stainless steel by electron beam melting for nuclear fusion applications,” *J. Nucl. Mater.*, 2017, doi: 10.1016/j.jnucmat.2016.12.042.
- [62] D. Wang, C. Song, Y. Yang, and Y. Bai, “Investigation of crystal growth mechanism during selective laser melting and mechanical property characterization of 316L stainless steel parts,” *Mater. Des.*, 2016, doi: 10.1016/j.matdes.2016.03.111.
- [63] S. Mirzababaei and S. Pasebani, “A review on binder jet additive manufacturing of 316L stainless steel,” *Journal of Manufacturing and Materials Processing*. 2019. doi: 10.3390/jmmp3030082.
- [64] X. Chen, J. Li, X. Cheng, H. Wang, and Z. Huang, “Effect of heat treatment on microstructure, mechanical and corrosion properties of austenitic stainless steel 316L using arc additive manufacturing,” *Mater. Sci. Eng. A*, 2018, doi: 10.1016/j.msea.2017.10.002.
- [65] A. F. Padilha and P. R. Rios, “Decomposition of austenite in austenitic stainless steels,” *ISIJ Int.*, 2002, doi: 10.2355/isijinternational.42.325.
- [66] E. Liverani, S. Toschi, L. Ceschini, and A. Fortunato, “Effect of selective laser melting (SLM) process parameters on microstructure and mechanical properties of 316L austenitic stainless steel,” *J. Mater. Process. Technol.*, 2017, doi: 10.1016/j.jmatprotec.2017.05.042.
- [67] Y. Zhong, L. Liu, S. Wikman, D. Cui, and Z. Shen, “Intragranular cellular segregation network structure strengthening 316L stainless steel prepared by selective laser melting,” *J. Nucl. Mater.*, 2016, doi: 10.1016/j.jnucmat.2015.12.034.
- [68] A. Yadollahi, N. Shamsaei, S. M. Thompson, and D. W. Seely, “Effects of process time interval and heat treatment on the mechanical and microstructural properties of direct laser deposited 316L stainless steel,” *Mater. Sci. Eng. A*, 2015, doi: 10.1016/j.msea.2015.07.056.
- [69] C. Qiu, M. Al Kindi, A. S. Aladawi, and I. Al Hatmi, “A comprehensive study on microstructure and tensile behaviour of a selectively laser melted stainless steel,” *Sci. Rep.*, 2018, doi: 10.1038/s41598-018-26136-7.
- [70] L. Qin *et al.*, “The microstructure and mechanical properties of deposited-IN625 by laser additive manufacturing,” *Rapid Prototyp. J.*, 2017, doi: 10.1108/RPJ-05-2016-0081.
- [71] Z. Tian *et al.*, “A review on laser powder bed fusion of inconel 625 nickel-based alloy,” *Applied Sciences (Switzerland)*. 2020. doi: 10.3390/app10010081.
- [72] Y. Wang *et al.*, “Effect of magnetic Field on the microstructure and mechanical properties of inconel 625 superalloy fabricated by wire arc additive manufacturing,” *J. Manuf. Process.*, 2021, doi: 10.1016/j.jmapro.2021.01.008.
- [73] F. Zhang *et al.*, “Homogenization kinetics of a nickel-based superalloy produced by powder bed fusion laser sintering,” *Scr. Mater.*, 2017, doi: 10.1016/j.scriptamat.2016.12.037.
- [74] C. Li, R. White, X. Y. Fang, M. Weaver, and Y. B. Guo, “Microstructure evolution

- characteristics of Inconel 625 alloy from selective laser melting to heat treatment,” *Mater. Sci. Eng. A*, 2017, doi: 10.1016/j.msea.2017.08.058.
- [75] E. A. Lass *et al.*, “Formation of the Ni₃Nb δ -Phase in Stress-Relieved Inconel 625 Produced via Laser Powder-Bed Fusion Additive Manufacturing,” *Metall. Mater. Trans. A Phys. Metall. Mater. Sci.*, 2017, doi: 10.1007/s11661-017-4304-6.
- [76] Y. L. Hu *et al.*, “Plastic deformation behavior and dynamic recrystallization of Inconel 625 superalloy fabricated by directed energy deposition,” *Mater. Des.*, 2020, doi: 10.1016/j.matdes.2019.108359.
- [77] R. M. Mahamood and E. T. Akinlabi, “Types of Functionally Graded Materials and Their Areas of Application,” in *Topics in Mining, Metallurgy and Materials Engineering*, 2017. doi: 10.1007/978-3-319-53756-6_2.
- [78] Y. H. Xiao, P. W. Liu, Z. Wang, Y. Wang, K. Q. Feng, and L. Chen, “La₂O₃ addition for improving the brazed joints of WC-Co/1Cr13,” *J. Mater. Process. Technol.*, 2019, doi: 10.1016/j.jmatprotec.2018.11.045.
- [79] B. Onuiké, B. Heer, and A. Bandyopadhyay, “Additive manufacturing of Inconel 718—Copper alloy bimetallic structure using laser engineered net shaping (LENSTM),” *Addit. Manuf.*, 2018, doi: 10.1016/j.addma.2018.02.007.
- [80] B. Heer and A. Bandyopadhyay, “Compositionally graded magnetic-nonmagnetic bimetallic structure using laser engineered net shaping,” *Mater. Lett.*, 2018, doi: 10.1016/j.matlet.2017.12.129.
- [81] Y. Xiao, K. Feng, H. Chen, Y. Zhou, Y. Li, and H. Shi, “Fabrication and micro-structure of a multilayer functionally graded (WC-Co)-Ni composite,” *J. Alloys Compd.*, 2015, doi: 10.1016/j.jallcom.2015.01.092.
- [82] B. Onuiké and A. Bandyopadhyay, “Additive manufacturing of Inconel 718 – Ti6Al4V bimetallic structures,” *Addit. Manuf.*, 2018, doi: 10.1016/j.addma.2018.06.025.
- [83] Q. Guo *et al.*, “In-situ characterization and quantification of melt pool variation under constant input energy density in laser powder bed fusion additive manufacturing process,” *Addit. Manuf.*, 2019, doi: 10.1016/j.addma.2019.04.021.
- [84] Z. Wang *et al.*, “Uncertainty quantification and reduction in metal additive manufacturing,” *npj Comput. Mater.*, vol. 6, no. 1, p. 175, 2020, doi: 10.1038/s41524-020-00444-x.
- [85] Y. Zhang, G. S. Hong, D. Ye, K. Zhu, and J. Y. H. Fuh, “Extraction and evaluation of melt pool, plume and spatter information for powder-bed fusion AM process monitoring,” *Mater. Des.*, 2018, doi: 10.1016/j.matdes.2018.07.002.
- [86] M. Khanzadeh, S. Chowdhury, M. A. Tschopp, H. R. Doude, M. Marufuzzaman, and L. Bian, “In-situ monitoring of melt pool images for porosity prediction in directed energy deposition processes,” *IISE Trans.*, vol. 51, no. 5, pp. 437–455, 2019, doi:

10.1080/24725854.2017.1417656.

- [87] R. Seede *et al.*, “An ultra-high strength martensitic steel fabricated using selective laser melting additive manufacturing: Densification, microstructure, and mechanical properties,” *Acta Mater.*, 2020, doi: 10.1016/j.actamat.2019.12.037.
- [88] R. Cunningham *et al.*, “Keyhole threshold and morphology in laser melting revealed by ultrahigh-speed x-ray imaging,” *Science (80-.)*, 2019, doi: 10.1126/science.aav4687.
- [89] J. V. Gordon *et al.*, “Defect structure process maps for laser powder bed fusion additive manufacturing,” *Addit. Manuf.*, 2020, doi: 10.1016/j.addma.2020.101552.
- [90] R. Liu, S. Liu, and X. Zhang, “A physics-informed machine learning model for porosity analysis in laser powder bed fusion additive manufacturing,” *Int. J. Adv. Manuf. Technol.*, 2021, doi: 10.1007/s00170-021-06640-3.
- [91] M. J. Anderson, C. Panwisawas, Y. Sovani, R. P. Turner, J. W. Brooks, and H. C. Basoalto, “Mean-field modelling of the intermetallic precipitate phases during heat treatment and additive manufacture of Inconel 718,” *Acta Mater.*, 2018, doi: 10.1016/j.actamat.2018.07.002.
- [92] Y. T. Tang *et al.*, “Alloys-by-design: Application to new superalloys for additive manufacturing,” *Acta Mater.*, 2021, doi: 10.1016/j.actamat.2020.09.023.
- [93] H. Chen, D. Gu, J. Xiong, and M. Xia, “Improving additive manufacturing processability of hard-to-process overhanging structure by selective laser melting,” *J. Mater. Process. Technol.*, 2017, doi: 10.1016/j.jmatprotec.2017.06.044.
- [94] T. Heeling, M. Cloots, and K. Wegener, “Melt pool simulation for the evaluation of process parameters in selective laser melting,” *Addit. Manuf.*, 2017, doi: 10.1016/j.addma.2017.02.003.
- [95] M. Mozaffar *et al.*, “Data-driven prediction of the high-dimensional thermal history in directed energy deposition processes via recurrent neural networks,” *Manuf. Lett.*, 2018, doi: 10.1016/j.mfglet.2018.10.002.
- [96] Y. Xiao *et al.*, “A gleeble-assisted study of phase evolution of Ti-6Al-4V induced by thermal cycles during additive manufacturing,” *J. Alloys Compd.*, 2021, doi: 10.1016/j.jallcom.2020.158409.
- [97] “The rise of data-driven modelling,” *Nature Reviews Physics*. 2021. doi: 10.1038/s42254-021-00336-z.
- [98] A. A. Antonysamy, P. B. Prangnell, and J. Meyer, “Effect of wall thickness transitions on texture and grain structure in additive layer manufacture (ALM) of Ti-6Al-4V,” 2012. doi: 10.4028/www.scientific.net/MSF.706-709.205.
- [99] C. Qiu *et al.*, “Influence of Laser Processing Strategy and Remelting on Surface Structure

- and Porosity Development during Selective Laser Melting of a Metallic Material,” *Metall. Mater. Trans. A Phys. Metall. Mater. Sci.*, 2019, doi: 10.1007/s11661-019-05348-0.
- [100] L. X. Lu, N. Sridhar, and Y. W. Zhang, “Phase field simulation of powder bed-based additive manufacturing,” *Acta Mater.*, 2018, doi: 10.1016/j.actamat.2017.11.033.
- [101] M. Yang, L. Wang, and W. Yan, “Phase-field modeling of grain evolutions in additive manufacturing from nucleation, growth, to coarsening,” *npj Comput. Mater.*, 2021, doi: 10.1038/s41524-021-00524-6.
- [102] J. Akram, P. Chalavadi, D. Pal, and B. Stucker, “Understanding grain evolution in additive manufacturing through modeling,” *Addit. Manuf.*, 2018, doi: 10.1016/j.addma.2018.03.021.
- [103] A. Zinoviev, O. Zinovieva, V. Ploshikhin, V. Romanova, and R. Balokhonov, “Evolution of grain structure during laser additive manufacturing. Simulation by a cellular automata method,” *Mater. Des.*, 2016, doi: 10.1016/j.matdes.2016.05.125.
- [104] K. Teferra and D. J. Rowenhorst, “Optimizing the cellular automata finite element model for additive manufacturing to simulate large microstructures,” *Acta Mater.*, 2021, doi: 10.1016/j.actamat.2021.116930.
- [105] S. Sunny, H. Yu, R. Mathews, A. Malik, and W. Li, “Improved grain structure prediction in metal additive manufacturing using a Dynamic Kinetic Monte Carlo framework,” *Addit. Manuf.*, 2021, doi: 10.1016/j.addma.2020.101649.
- [106] T. M. Rodgers *et al.*, “Simulation of powder bed metal additive manufacturing microstructures with coupled finite difference-Monte Carlo method,” *Addit. Manuf.*, 2021, doi: 10.1016/j.addma.2021.101953.
- [107] Y. Ji, L. Chen, and L. Q. Chen, “Understanding Microstructure Evolution During Additive Manufacturing of Metallic Alloys Using Phase-Field Modeling,” in *Thermo-Mechanical Modeling of Additive Manufacturing*, 2017. doi: 10.1016/B978-0-12-811820-7.00008-2.
- [108] Z. Wang, P. Liu, Y. Xiao, X. Cui, Z. Hu, and L. Chen, “A Data-Driven Approach for Process Optimization of Metallic Additive Manufacturing under Uncertainty,” *J. Manuf. Sci. Eng. Trans. ASME*, 2019, doi: 10.1115/1.4043798.
- [109] Z. Wang, P. Liu, Y. Xiao, X. Cui, Z. Hu, and L. Chen, “A Data-Driven Approach for Process Optimization of Metallic Additive Manufacturing under Uncertainty,” *J. Manuf. Sci. Eng. Trans. ASME*, vol. 141, no. 8, pp. 1–14, 2019, doi: 10.1115/1.4043798.
- [110] O. Kwon *et al.*, “A deep neural network for classification of melt-pool images in metal additive manufacturing,” *J. Intell. Manuf.*, 2020, doi: 10.1007/s10845-018-1451-6.
- [111] H. Yeung, Z. Yang, and L. Yan, “A melt-pool prediction based scan strategy for powder bed fusion additive manufacturing,” *Addit. Manuf.*, 2020, doi: 10.1016/j.addma.2020.101383.
- [112] Z. L. Wang and Y. Adachi, “Property prediction and properties-to-microstructure inverse

- analysis of steels by a machine-learning approach,” *Mater. Sci. Eng. A*, 2019, doi: 10.1016/j.msea.2018.12.049.
- [113] Z. Wang *et al.*, “Uncertainty Quantification in Metallic Additive Manufacturing Through Physics-Informed Data-Driven Modeling,” *JOM*, 2019, doi: 10.1007/s11837-019-03555-z.
- [114] P. W. Liu *et al.*, “Integration of phase-field model and crystal plasticity for the prediction of process-structure-property relation of additively manufactured metallic materials,” *Int. J. Plast.*, p. 102670, 2020.
- [115] M. Ghayoomi Mohammadi, D. Mahmoud, and M. Elbestawi, “On the application of machine learning for defect detection in L-PBF additive manufacturing,” *Opt. Laser Technol.*, 2021, doi: 10.1016/j.optlastec.2021.107338.
- [116] J. L. Bartlett, A. Jarama, J. Jones, and X. Li, “Prediction of microstructural defects in additive manufacturing from powder bed quality using digital image correlation,” *Mater. Sci. Eng. A*, 2020, doi: 10.1016/j.msea.2020.140002.
- [117] P. Liu, X. Cui, J. Deng, S. Li, Z. Li, and L. Chen, “Investigation of thermal responses during metallic additive manufacturing using a ‘Tri-Prism’ finite element method,” *Int. J. Therm. Sci.*, 2019, doi: 10.1016/j.ijthermalsci.2018.10.022.
- [118] S. M. Kelly and S. L. Kampe, “Microstructural evolution in laser-deposited multilayer Ti-6Al-4V builds: Part II. Thermal Modeling,” *Metall. Mater. Trans. A Phys. Metall. Mater. Sci.*, 2004, doi: 10.1007/s11661-004-0095-7.
- [119] S. M. Kelly and S. L. Kampe, “Microstructural evolution in laser-deposited multilayer Ti-6Al-4V builds: Part 1. Microstructural characterization,” *Metall. Mater. Trans. A Phys. Metall. Mater. Sci.*, 2004, doi: 10.1007/s11661-004-0094-8.
- [120] W. Xu, S. Sun, J. Elambasseril, Q. Liu, M. Brandt, and M. Qian, “Ti-6Al-4V Additively Manufactured by Selective Laser Melting with Superior Mechanical Properties,” *JOM*, 2015, doi: 10.1007/s11837-015-1297-8.
- [121] G. J. Marshall, W. J. Young, S. M. Thompson, N. Shamsaei, S. R. Daniewicz, and S. Shao, “Understanding the Microstructure Formation of Ti-6Al-4V During Direct Laser Deposition via In-Situ Thermal Monitoring,” *JOM*, 2016, doi: 10.1007/s11837-015-1767-z.
- [122] X. Tan *et al.*, “Graded microstructure and mechanical properties of additive manufactured Ti-6Al-4V via electron beam melting,” *Acta Mater.*, 2015, doi: 10.1016/j.actamat.2015.06.036.
- [123] M. F. Zäh and S. Lutzmann, “Modelling and simulation of electron beam melting,” *Prod. Eng.*, 2010, doi: 10.1007/s11740-009-0197-6.
- [124] B. Zheng, Y. Zhou, J. E. Smugeresky, J. M. Schoenung, and E. J. Lavernia, “Thermal behavior and microstructural evolution during laser deposition with laser-engineered net

- shaping: Part I. Numerical calculations,” *Metall. Mater. Trans. A Phys. Metall. Mater. Sci.*, 2008, doi: 10.1007/s11661-008-9557-7.
- [125] B. E. Carroll, T. A. Palmer, and A. M. Beese, “Anisotropic tensile behavior of Ti-6Al-4V components fabricated with directed energy deposition additive manufacturing,” *Acta Mater.*, 2015, doi: 10.1016/j.actamat.2014.12.054.
- [126] M. Fahrman and A. Suzuki, “Effect of Cooling Rate on Gleeble Hot Ductility of UDIMET Alloy 720 Billet,” 2012. doi: 10.7449/2008/superalloys_2008_311_316.
- [127] Z. Sun, S. Guo, and H. Yang, “Nucleation and growth mechanism of α -lamellae of Ti alloy TA15 cooling from an $\alpha + \beta$ phase field,” *Acta Mater.*, 2013, doi: 10.1016/j.actamat.2012.12.025.
- [128] S. Moeinifar, A. H. Kokabi, and H. R. M. Hosseini, “Effect of tandem submerged arc welding process and parameters of Gleeble simulator thermal cycles on properties of the intercritically reheated heat affected zone,” *Mater. Des.*, 2011, doi: 10.1016/j.matdes.2010.07.005.
- [129] M. J. Cieslak, T. J. Headley, and W. A. Baeslack, “Effect of thermal processing on the microstructure of Ti-26Al-11Nb: Applications to fusion welding,” *Metall. Trans. A*, 1990, doi: 10.1007/BF02656544.
- [130] S. M. Kelly, “Thermal and microstructure modeling of metal deposition processes with application to titanium aluminum vanadium.” Virginia Polytechnic Institute and State University, 2004.
- [131] H. Zhou, K. Feng, Y. Xiao, Y. Liu, and S. Ke, “Pressure effects on a novel W-Mo-Cu alloy by large current electric field sintering: Sintering behavior, microstructure and properties,” *J. Alloys Compd.*, 2019, doi: 10.1016/j.jallcom.2019.01.297.
- [132] A. F. Boostani *et al.*, “Heat Treatment Strategies to Improve the Quasi-Static and Dynamic Performance of $\alpha + \beta$ Titanium Alloys,” in *TMS 2019 148th Annual Meeting & Exhibition Supplemental Proceedings*, 2019, pp. 1383–1387.
- [133] B. Schoinochoritis, D. Chantzis, and K. Salonitis, “Simulation of metallic powder bed additive manufacturing processes with the finite element method: A critical review,” *Proceedings of the Institution of Mechanical Engineers, Part B: Journal of Engineering Manufacture*. 2017. doi: 10.1177/0954405414567522.
- [134] S. H. Nikam and N. K. Jain, “Modeling and Prediction of Residual Stresses in Additive Layer Manufacturing by Microplasma Transferred Arc Process Using Finite Element Simulation,” *J. Manuf. Sci. Eng. Trans. ASME*, 2019, doi: 10.1115/1.4043264.
- [135] J. C. Heigel, “Thermo-Mechanical Model Development and Experimental Validation for Directed Energy Deposition Additive Manufacturing Processes,” 2015.
- [136] S. Malinov, W. Sha, Z. Guo, C. C. Tang, and A. E. Long, “Synchrotron X-ray diffraction

- study of the phase transformations in titanium alloys,” *Mater. Charact.*, 2002, doi: 10.1016/S1044-5803(02)00286-3.
- [137] M. Neikter, P. Åkerfeldt, R. Pederson, M. L. Antti, and V. Sandell, “Microstructural characterization and comparison of Ti-6Al-4V manufactured with different additive manufacturing processes,” *Mater. Charact.*, 2018, doi: 10.1016/j.matchar.2018.02.003.
- [138] B. McArthur, “Effects of thermal processing variations on microstructure and high cycle fatigue of beta-STOA Ti-6Al-4V.” Colorado School of Mines. Arthur Lakes Library, 2017.
- [139] J. I. Qazi, J. Rahim, F. H. (SAM) Fores, A. Genc, and F. H. Froes, “Phase transformations in Ti-6Al-4V-xH alloys,” *Metall. Mater. Trans. A Phys. Metall. Mater. Sci.*, 2001, doi: 10.1007/s11661-001-0035-8.
- [140] A. K. Singla, J. Singh, and V. S. Sharma, “Microstructure and Mechanical Properties of Lamellar Ti-6Al-4V ELI Alloy,” in *Manufacturing Engineering*, Springer, 2019, pp. 109–116.
- [141] Y. wei SUI, B. sheng LI, A. hui LIU, H. NAN, J. jie GUO, and H. zhi FU, “Microstructures and hardness of Ti-6Al-4V alloy staging castings under centrifugal field,” *Trans. Nonferrous Met. Soc. China (English Ed.)*, 2008, doi: 10.1016/S1003-6326(08)60051-5.
- [142] J. W. Elmer, T. A. Palmer, S. S. Babu, and E. D. Specht, “In situ observations of lattice expansion and transformation rates of α and β phases in Ti-6Al-4V,” *Mater. Sci. Eng. A*, 2005, doi: 10.1016/j.msea.2004.08.084.
- [143] V. Manvatkar, A. De, and T. DebRoy, “Spatial variation of melt pool geometry, peak temperature and solidification parameters during laser assisted additive manufacturing process,” *Mater. Sci. Technol. (United Kingdom)*, 2015, doi: 10.1179/1743284714Y.0000000701.
- [144] H. Wang and Y. Zou, “Microscale interaction between laser and metal powder in powder-bed additive manufacturing: Conduction mode versus keyhole mode,” *Int. J. Heat Mass Transf.*, 2019, doi: 10.1016/j.ijheatmasstransfer.2019.118473.
- [145] Y. Ji, T. W. Heo, F. Zhang, and L. Q. Chen, “Theoretical Assessment on the Phase Transformation Kinetic Pathways of Multi-component Ti Alloys: Application to Ti-6Al-4V,” *J. Phase Equilibria Diffus.*, 2016, doi: 10.1007/s11669-015-0436-9.
- [146] T. W. Heo, D. S. Shih, and L. Q. Chen, “Kinetic pathways of phase transformations in two-phase Ti alloys,” *Metall. Mater. Trans. A Phys. Metall. Mater. Sci.*, 2014, doi: 10.1007/s11661-014-2269-2.
- [147] Y. H. Xiao, P. W. Liu, Z. Wang, Y. Wang, K. Q. Feng, and L. Chen, “La₂O₃ addition for improving the brazed joints of WC-Co/1Cr13,” *J. Mater. Process. Technol.*, 2019, doi: 10.1016/j.jmatprotec.2018.11.045.
- [148] T. B. Massalski, “Massive transformations revisited,” 2002. doi: 10.1007/s11661-002-

0351-7.

- [149] A. L. Pilchak and T. F. Broderick, “Evidence of a massive transformation in a Ti-6Al-4V solid-state weld?,” *JOM*, 2013, doi: 10.1007/s11837-013-0591-6.
- [150] C. L. A. Leung, S. Marussi, R. C. Atwood, M. Towrie, P. J. Withers, and P. D. Lee, “In situ X-ray imaging of defect and molten pool dynamics in laser additive manufacturing,” *Nat. Commun.*, 2018, doi: 10.1038/s41467-018-03734-7.
- [151] L. Aucott *et al.*, “Revealing internal flow behaviour in arc welding and additive manufacturing of metals,” *Nat. Commun.*, 2018, doi: 10.1038/s41467-018-07900-9.
- [152] Q. Guo *et al.*, “In-situ full-field mapping of melt flow dynamics in laser metal additive manufacturing,” *Addit. Manuf.*, 2020, doi: 10.1016/j.addma.2019.100939.
- [153] Y. Zhao, Y. Koizumi, K. Aoyagi, D. Wei, K. Yamanaka, and A. Chiba, “Molten pool behavior and effect of fluid flow on solidification conditions in selective electron beam melting (SEBM) of a biomedical Co-Cr-Mo alloy,” *Addit. Manuf.*, 2019, doi: 10.1016/j.addma.2018.12.002.
- [154] N. Chen *et al.*, “Microstructural characteristics and crack formation in additively manufactured bimetal material of 316L stainless steel and Inconel 625,” *Addit. Manuf.*, 2020, doi: 10.1016/j.addma.2020.101037.
- [155] S. Sridar, M. A. Klecka, and W. Xiong, “Interfacial characteristics of P91 steel - Inconel 740H bimetallic structure fabricated using wire-arc additive manufacturing,” *J. Mater. Process. Technol.*, 2022, doi: 10.1016/j.jmatprotec.2021.117396.
- [156] C. Wei *et al.*, “Understanding of process and material behaviours in additive manufacturing of Invar36/Cu10Sn multiple material components via laser-based powder bed fusion,” *Addit. Manuf.*, 2021, doi: 10.1016/j.addma.2020.101683.
- [157] K. Karayagiz *et al.*, “Finite interface dissipation phase field modeling of Ni–Nb under additive manufacturing conditions,” *Acta Mater.*, 2020, doi: 10.1016/j.actamat.2019.11.057.
- [158] T. Keller *et al.*, “Application of finite element, phase-field, and CALPHAD-based methods to additive manufacturing of Ni-based superalloys,” *Acta Mater.*, 2017, doi: 10.1016/j.actamat.2017.05.003.
- [159] M. R. N. Esfahani, J. Coupland, and S. Marimuthu, “Numerical simulation of alloy composition in dissimilar laser welding,” *J. Mater. Process. Technol.*, 2015, doi: 10.1016/j.jmatprotec.2015.05.005.
- [160] R. S. Gonzaga, F. W. C. Farias, and J. da C. Payão Filho, “Microstructural characterization of the transition zone between a C–Mn steel pipe and a 70%Ni30%Cu alloy cladding welded by HW-GTAW,” *Int. J. Press. Vessel. Pip.*, 2021, doi: 10.1016/j.ijpvp.2021.104433.
- [161] L. Hardwick, P. Rodgers, E. Pickering, and R. Goodall, “Development of a Novel Ni-Based

- Multi-principal Element Alloy Filler Metal, Using an Alternative Melting Point Depressant,” *Metall. Mater. Trans. A Phys. Metall. Mater. Sci.*, 2021, doi: 10.1007/s11661-021-06246-0.
- [162] B. J. Babalola, O. O. Ayodele, M. A. Awotunde, S. O. Akinwamide, and P. A. Olubambi, “Microstructure and mechanical properties of Ni-17Cr-xCo ternary alloys fabricated via field-assisted sintering,” *Mater. Lett.*, 2021, doi: 10.1016/j.matlet.2021.130404.
- [163] Z. S. Saldi, A. Kidess, S. Kenjereš, C. Zhao, I. M. Richardson, and C. R. Kleijn, “Effect of enhanced heat and mass transport and flow reversal during cool down on weld pool shapes in laser spot welding of steel,” *Int. J. Heat Mass Transf.*, 2013, doi: 10.1016/j.ijheatmasstransfer.2013.07.085.
- [164] P. Farahmand and R. Kovacevic, “An experimental-numerical investigation of heat distribution and stress field in single- and multi-track laser cladding by a high-power direct diode laser,” *Opt. Laser Technol.*, 2014, doi: 10.1016/j.optlastec.2014.04.016.
- [165] F. Chen and W. Yan, “High-fidelity modelling of thermal stress for additive manufacturing by linking thermal-fluid and mechanical models,” *Mater. Des.*, 2020, doi: 10.1016/j.matdes.2020.109185.
- [166] Y. S. Lee and W. Zhang, “Mesoscopic simulation of heat transfer and fluid flow in laser powder bed additive manufacturing,” 2020.
- [167] W. I. Cho and P. Woizeschke, “Analysis of molten pool dynamics in laser welding with beam oscillation and filler wire feeding,” *Int. J. Heat Mass Transf.*, 2021, doi: 10.1016/j.ijheatmasstransfer.2020.120623.
- [168] Z. Gan, G. Yu, X. He, and S. Li, “Numerical simulation of thermal behavior and multicomponent mass transfer in direct laser deposition of Co-base alloy on steel,” *Int. J. Heat Mass Transf.*, 2017, doi: 10.1016/j.ijheatmasstransfer.2016.08.049.
- [169] A. Kar and J. Mazumder, “Model for nonequilibrium partitioning during rapid solidification of binary concentrated solutions,” *Acta Metall. Mater.*, 1992, doi: 10.1016/0956-7151(92)90174-D.
- [170] C. E. Krill and L. Q. Chen, “Computer simulation of 3-D grain growth using a phase-field model,” *Acta Mater.*, 2002, doi: 10.1016/s1359-6454(02)00084-8.
- [171] L. Chen *et al.*, “An integrated fast Fourier transform-based phase-field and crystal plasticity approach to model recrystallization of three dimensional polycrystals,” *Comput. Methods Appl. Mech. Eng.*, 2015, doi: 10.1016/j.cma.2014.12.007.
- [172] T. Pinomaa and N. Provatas, “Quantitative phase field modeling of solute trapping and continuous growth kinetics in quasi-rapid solidification,” *Acta Mater.*, 2019, doi: 10.1016/j.actamat.2019.02.009.
- [173] S. Kavousi and M. Asle Zaeem, “Quantitative phase-field modeling of solute trapping in

- rapid solidification,” *Acta Mater.*, 2021, doi: 10.1016/j.actamat.2020.116562.
- [174] J. Zhang, F. Liou, W. Seufzer, and K. Taminger, “A coupled finite element cellular automaton model to predict thermal history and grain morphology of Ti-6Al-4V during direct metal deposition (DMD),” *Addit. Manuf.*, vol. 11, pp. 32–39, 2016, doi: 10.1016/j.addma.2016.04.004.
- [175] H. Search, C. Journals, A. Contact, M. Iopscience, M. Simul, and I. P. Address, “3D probabilistic modelling of equiaxed eutectic solidification,” *Model. Simul. Mater. Se. Eng. I*, pp. 455–466, 1993.
- [176] M. A. Arafin, M. Medraj, D. P. Turner, and P. Bocher, “Transient liquid phase bonding of Inconel 718 and Inconel 625 with BNi-2: Modeling and experimental investigations,” *Mater. Sci. Eng. A*, 2007, doi: 10.1016/j.msea.2006.10.045.
- [177] S. R. Pulugurtha, “Functionally graded Ti6Si4V and Inconel 625 by laser metal deposition,” 2014.
- [178] E. Kaschnitz, L. Kaschnitz, and S. Heugenhauer, “Electrical Resistivity Measured by Millisecond Pulse Heating in Comparison with Thermal Conductivity of the Superalloy Inconel 625 at Elevated Temperature,” *Int. J. Thermophys.*, 2019, doi: 10.1007/s10765-019-2490-8.
- [179] H. Mizukami, T. Suzuki, T. Umeda, and W. Kurz, “Initial stage of rapid solidification of 18-8 stainless steel,” *Mater. Sci. Eng. A*, 1993, doi: 10.1016/0921-5093(93)90245-A.
- [180] T. Okane and T. Umeda, “Eutectic growth of unidirectionally solidified Fe-Cr-Ni alloy,” *ISIJ Int.*, 1998, doi: 10.2355/isijinternational.38.454.
- [181] Y. Yang, O. Ragnvaldsen, Y. Bai, M. Yi, and B. X. Xu, “3D non-isothermal phase-field simulation of microstructure evolution during selective laser sintering,” *npj Comput. Mater.*, 2019, doi: 10.1038/s41524-019-0219-7.
- [182] P. Ganesh *et al.*, “Fatigue and fracture toughness characteristics of laser rapid manufactured Inconel 625 structures,” *Mater. Sci. Eng. A*, vol. 527, no. 29–30, pp. 7490–7497, Nov. 2010, doi: 10.1016/j.msea.2010.08.034.
- [183] L. E. Murr, “Metallurgy of additive manufacturing: Examples from electron beam melting,” *Addit. Manuf.*, vol. 5, pp. 40–53, Jan. 2015, doi: 10.1016/j.addma.2014.12.002.
- [184] J. A. Gonzalez, J. Mireles, S. W. Stafford, M. A. Perez, C. A. Terrazas, and R. B. Wicker, “Characterization of Inconel 625 fabricated using powder-bed-based additive manufacturing technologies,” *J. Mater. Process. Technol.*, vol. 264, pp. 200–210, Feb. 2019, doi: 10.1016/j.jmatprotec.2018.08.031.
- [185] Y. Huang *et al.*, “Rapid prediction of real-time thermal characteristics, solidification parameters and microstructure in laser directed energy deposition (powder-fed additive manufacturing),” *J. Mater. Process. Technol.*, 2019, doi: 10.1016/j.jmatprotec.2019.116286.

- [186] J. Coleman *et al.*, “Sensitivity of Thermal Predictions to Uncertain Surface Tension Data in Laser Additive Manufacturing,” *J. Heat Transfer*, 2020, doi: 10.1115/1.4047916.
- [187] R. Shi, S. A. Khairallah, T. T. Roehling, T. W. Heo, J. T. McKeown, and M. J. Matthews, “Microstructural control in metal laser powder bed fusion additive manufacturing using laser beam shaping strategy,” *Acta Mater.*, 2020, doi: 10.1016/j.actamat.2019.11.053.
- [188] Y. L. Hu *et al.*, “Evolution of solidification microstructure and dynamic recrystallisation of Inconel 625 during laser solid forming process,” *J. Mater. Sci.*, 2018, doi: 10.1007/s10853-018-2701-x.
- [189] M. Ma, Z. Wang, and X. Zeng, “A comparison on metallurgical behaviors of 316L stainless steel by selective laser melting and laser cladding deposition,” *Mater. Sci. Eng. A*, 2017, doi: 10.1016/j.msea.2016.12.112.
- [190] S. Gao *et al.*, “Recrystallization-based grain boundary engineering of 316L stainless steel produced via selective laser melting,” *Acta Mater.*, 2020, doi: 10.1016/j.actamat.2020.09.015.
- [191] A. E. Wilson-Heid, S. Qin, and A. M. Beese, “Multiaxial plasticity and fracture behavior of stainless steel 316L by laser powder bed fusion: Experiments and computational modeling,” *Acta Mater.*, 2020, doi: 10.1016/j.actamat.2020.08.066.
- [192] M. Rafieezad, M. Ghaffari, A. Vahedi Nemani, and A. Nasiri, “Microstructural evolution and mechanical properties of a low-carbon low-alloy steel produced by wire arc additive manufacturing,” *Int. J. Adv. Manuf. Technol.*, 2019, doi: 10.1007/s00170-019-04393-8.
- [193] K. Zhang, S. Wang, W. Liu, and X. Shang, “Characterization of stainless steel parts by Laser Metal Deposition Shaping,” *Mater. Des.*, 2014, doi: 10.1016/j.matdes.2013.09.006.
- [194] R. Wirth, “Focused Ion Beam (FIB) combined with SEM and TEM: Advanced analytical tools for studies of chemical composition, microstructure and crystal structure in geomaterials on a nanometre scale,” *Chem. Geol.*, 2009, doi: 10.1016/j.chemgeo.2008.05.019.
- [195] S. Lee, J. Peng, D. Shin, and Y. S. Choi, “Data analytics approach for melt-pool geometries in metal additive manufacturing,” *Sci. Technol. Adv. Mater.*, 2019, doi: 10.1080/14686996.2019.1671140.
- [196] Z. Yang, Y. Lu, H. Yeung, and S. Krishnamurty, “From scan strategy to melt pool prediction: A neighboring-effect modeling method,” *J. Comput. Inf. Sci. Eng.*, vol. 20, no. 5, 2020, doi: 10.1115/1.4046335.
- [197] Z. Yang, Y. Lu, H. Yeung, and S. Kirishnamurty, “3D build melt pool predictive modeling for powder bed fusion additive manufacturing,” 2020. doi: 10.1115/DETC2020-22662.
- [198] Y. Ren, Q. Wang, and P. (Pan) Michaleris, “A Physics-Informed Two-Level Machine-Learning Model for Predicting Melt-Pool Size in Laser Powder Bed Fusion,” *J. Dyn. Syst.*

- Meas. Control*, 2021, doi: 10.1115/1.4052245.
- [199] Y. Du, T. Mukherjee, and T. DebRoy, “Physics-informed machine learning and mechanistic modeling of additive manufacturing to reduce defects,” *Appl. Mater. Today*, 2021, doi: 10.1016/j.apmt.2021.101123.
- [200] Z. Ge, Z. Song, S. X. Ding, and B. Huang, “Data Mining and Analytics in the Process Industry: The Role of Machine Learning,” *IEEE Access*, vol. 5, pp. 20590–20616, 2017, doi: 10.1109/ACCESS.2017.2756872.
- [201] C. Wang, X. P. Tan, S. B. Tor, and C. S. Lim, “Machine learning in additive manufacturing: State-of-the-art and perspectives,” *Additive Manufacturing*. 2020. doi: 10.1016/j.addma.2020.101538.
- [202] D. Ye, J. Y. Hsi Fuh, Y. Zhang, G. S. Hong, and K. Zhu, “In situ monitoring of selective laser melting using plume and spatter signatures by deep belief networks,” *ISA Trans.*, vol. 81, no. May, pp. 96–104, 2018, doi: 10.1016/j.isatra.2018.07.021.
- [203] H. Zheng, H. Li, L. Lang, S. Gong, and Y. Ge, “Effects of scan speed on vapor plume behavior and spatter generation in laser powder bed fusion additive manufacturing,” *J. Manuf. Process.*, 2018, doi: 10.1016/j.jmapro.2018.09.011.
- [204] D. Ye, K. Zhu, J. Y. H. Fuh, Y. Zhang, and H. G. Soon, “The investigation of plume and spatter signatures on melted states in selective laser melting,” *Opt. Laser Technol.*, 2019, doi: 10.1016/j.optlastec.2018.10.019.
- [205] M. Grasso and B. M. Colosimo, “A statistical learning method for image-based monitoring of the plume signature in laser powder bed fusion,” *Robot. Comput. Integr. Manuf.*, 2019, doi: 10.1016/j.rcim.2018.11.007.
- [206] Y. Huang, X. Hua, F. Li, C. Shen, G. Mou, and B. Tang, “Spatter feature analysis in laser welding based on motion tracking method,” *J. Manuf. Process.*, 2020, doi: 10.1016/j.jmapro.2020.04.016.
- [207] L. Scime and J. Beuth, “Using machine learning to identify in-situ melt pool signatures indicative of flaw formation in a laser powder bed fusion additive manufacturing process,” *Addit. Manuf.*, vol. 25, no. September 2018, pp. 151–165, 2019, doi: 10.1016/j.addma.2018.11.010.
- [208] Z. Yang, Y. Lu, H. Yeung, and S. Krishnamurty, “From scan strategy to melt pool prediction: A neighboring-effect modeling method,” *J. Comput. Inf. Sci. Eng.*, 2020, doi: 10.1115/1.4046335.
- [209] L. C. Zhang, Y. Liu, S. Li, and Y. Hao, “Additive Manufacturing of Titanium Alloys by Electron Beam Melting: A Review,” *Advanced Engineering Materials*. 2018. doi: 10.1002/adem.201700842.
- [210] G. X. Gu, C. T. Chen, D. J. Richmond, and M. J. Buehler, “Bioinspired hierarchical

- composite design using machine learning: Simulation, additive manufacturing, and experiment,” *Mater. Horizons*, 2018, doi: 10.1039/c8mh00653a.
- [211] L. Scime and J. Beuth, “A multi-scale convolutional neural network for autonomous anomaly detection and classification in a laser powder bed fusion additive manufacturing process,” *Addit. Manuf.*, 2018, doi: 10.1016/j.addma.2018.09.034.
- [212] S. A. Shevchik, C. Kenel, C. Leinenbach, and K. Wasmer, “Acoustic emission for in situ quality monitoring in additive manufacturing using spectral convolutional neural networks,” *Addit. Manuf.*, 2018, doi: 10.1016/j.addma.2017.11.012.
- [213] S. S. Razvi, S. Feng, A. Narayanan, Y. T. T. Lee, and P. Witherell, “A review of machine learning applications in additive manufacturing,” 2019. doi: 10.1115/DETC2019-98415.
- [214] Z. Zhou, H. Shen, B. Liu, W. Du, and J. Jin, “Thermal field prediction for welding paths in multi-layer gas metal arc welding-based additive manufacturing: A machine learning approach,” *J. Manuf. Process.*, 2021, doi: 10.1016/j.jmapro.2021.02.033.
- [215] Y. Oh, M. Sharp, T. Sprock, and S. Kwon, “Neural network-based build time estimation for additive manufacturing: A performance comparison,” *J. Comput. Des. Eng.*, 2021, doi: 10.1093/jcde/qwab044.
- [216] Z. Yang, D. Eddy, S. Krishnamurty, I. Grosse, and Y. Lu, “A super-metamodeling framework to optimize system predictability,” 2018. doi: 10.1115/DETC201886055.
- [217] Z. A. Young *et al.*, “Types of spatter and their features and formation mechanisms in laser powder bed fusion additive manufacturing process,” *Addit. Manuf.*, 2020, doi: 10.1016/j.addma.2020.101438.
- [218] G. Repossini, V. Laguzza, M. Grasso, and B. M. Colosimo, “On the use of spatter signature for in-situ monitoring of Laser Powder Bed Fusion,” *Addit. Manuf.*, 2017, doi: 10.1016/j.addma.2017.05.004.
- [219] Z. Zhan and H. Li, “Machine learning based fatigue life prediction with effects of additive manufacturing process parameters for printed SS 316L,” *Int. J. Fatigue*, 2021, doi: 10.1016/j.ijfatigue.2020.105941.